

NASA-CR-164,942

A THREE-DIMENSIONAL SIMULATION
OF TRANSITION AND EARLY TURBULENCE
IN A TIME-DEVELOPING MIXING LAYER

NASA-CR-164942
19820003520
by
A. B. Cain,
W. C. Reynolds,
and
J. H. Ferziger

Prepared from work done under Grant
NASA NCC 2-15



LIBRARY COPY

Report No. TF-14

JUL 27 1990

LANGLEY RESEARCH CENTER
LIBRARY NASA, HAMPTON, VA

Thermosciences Division
Department of Mechanical Engineering
Stanford University
Stanford, California



NF01124

August 1981

A THREE-DIMENSIONAL SIMULATION
OF TRANSITION AND EARLY TURBULENCE
IN A TIME-DEVELOPING MIXING LAYER

by
A. B. Cain
W. C. Reynolds,
and
J. H. Ferziger

Prepared from work done under Grant
NASA NCC 2-15

Report No. TF-14

Thermosciences Division
Department of Mechanical Engineering
Stanford University
Stanford, California

August 1981

N82-11393#

This Page Intentionally Left Blank

Acknowledgments

The authors express their special appreciation to Drs. A. Leonard, R. Rogallo, A. Wray, and M. Rubesin of the NASA-Ames Research Center for many helpful discussions. Drs. N. Mansour and P. Moin provided a solid starting point in both fundamental tools and easily understood computer codes. Drs. W. J. Feiereisen and E. Shirani provided important discussion, as did J. Bardina. The excellent typing of Ruth Korb is greatly appreciated. Special thanks go to NASA-Ames Research Center for making this work possible through financial support under grant NASA NCC-2-15 and also by use of their facilities.

Abstract

The primary focus of this study is the physics of the transition and early turbulence regimes in the time-developing mixing layer. Three-dimensional, time-dependent numerical simulations were carried out. In particular, we deal with the sensitivity of the mixing layer to the disturbance field of the initial condition. The growth of the momentum thickness, the mean velocity profile, the turbulence kinetic energy, the Reynolds stresses, the anisotropy tensor, and particle track pictures of computations are all examined in an effort to better understand the physics of these regimes. The amplitude, spectrum shape, and random phases of the initial disturbance field were varied.

In carrying out this study, a new scheme of generating discrete orthogonal function expansions on some nonuniform grids was developed. In the present work it allowed us to compute in an infinite domain, eliminating image-flow problems. The new scheme retains the efficiency of the fast Fourier transform, but allows the application of more general boundary conditions by using a restricted set of mapping functions. In evaluations using linear test equations, the new scheme employed in the present work had errors up to six orders of magnitude smaller than in standard finite-difference methods (using equal numbers of grid points).

Due to computational limitations, all cases address the early or near field of the mixing layer. The results showed that large eddies may vary considerably, particularly in the turbulent structure measured by the anisotropy tensor. An interesting oscillatory behavior of the width of turbulent kinetic energy profile was observed. The most significant result shows that the secondary instability of the mixing layer is produced by spanwise variations in the straining field of the primary vortex structures.

Table of Contents

	Page
Acknowledgments	iii
Abstract	iv
List of Figures	vii
List of Tables	xii
Nomenclature	xiii
 Chapter	
1. INTRODUCTION	1
1.1 Background	1
1.2 Related Work	4
1.3 Motivation and Objectives	6
1.4 Summary of Present Work	9
2. PROBLEM FORMULATION	12
2.1 Governing Equations	12
2.2 Boundary Conditions	13
2.3 Initial Conditions	13
2.4 The Computational Domain	14
2.5 Filtering	15
2.6 Subgrid Modeling	17
2.7 Summary	19
3. NUMERICAL METHODS	20
3.1 Preview	20
3.2 Standard Fourier Methods	21
3.3 Fourier Transforms on Non-Uniform Grids	23
3.4 Derivative and Integral Operators	26
3.5 Resolution and Statistical Validity	28
3.6 Interpolation	30
3.7 Generating a Smooth, Divergence-Free Initial Dis- turbance Field	31
4. METHOD VALIDATION	33
4.1 Convection	33
4.2 Diffusion	35
4.3 Taylor-Green Problem (2-D)	36
5. RESULTS	37
5.2 Overview of Effects Studied	37
5.2 Case Descriptions	37
5.3 Mean Velocity Profiles	39
5.4 Momentum Thickness	40
5.5 Turbulent Kinetic Energy at the Center of the Mixing Layer	43

5.6	Profiles of the Turbulent Kinetic Energy	45
5.7	Reynolds Stresses	46
5.8	The Reynolds Stress Anisotropy Tensor	50
5.9	Correlation Coefficient at the Center of the Mixing Layer	53
5.10	Resolution and Statistical Validity	54
5.11	Particle-Tracking Visualizations	54
6.	CONCLUSIONS	61
Appendix		
A	Finite Difference Methods	64
B	Time-Integration Schemes	65
C	Subgrid Modeling	66
D	Image Flows	68
References		70
Figures		73

List of Figures

Figure		Page
1.3.1	The spatially developing mixing layer as created in the laboratory	73
1.3.2	The time-developing mixing layer studied in the present work	74
4.1.1	Comparison of finite difference, new Fourier, and analytical solutions to the first-order convection equation . .	75
4.2.1	Comparison of the maximum dimensionless errors of finite-difference and new Fourier solutions to the heat or diffusion equation	76
5.3.1	Mean velocity profile at various times for Case 6.	77
5.4.1	Normalized momentum thickness vs. dimensionless time for low-amplitude Cases 4 and 6.	78
5.4.2	Normalized momentum thickness vs. dimensionless time for medium-amplitude Cases 5, 7, 10, 11, and 9	78
5.4.3	Normalized momentum thickness vs. dimensionless time for high-amplitude Cases 2 and 8	79
5.4.4	Dimensionless momentum thickness growth rate vs. normalized momentum thickness for low-amplitude Cases 4 and 6 . . .	79
5.4.5	Dimensionless momentum thickness growth rate vs. normalized momentum thickness for medium-amplitude Cases 5, 7, 10, 11, and 9	80
5.4.6	Dimensionless momentum thickness growth rate vs. normalized momentum thickness for high-amplitude Cases 1 and 8 . . .	80
5.4.7	Dimensionless momentum thickness growth rate vs. normalized momentum thickness for cases with seed #1	81
5.4.8	Dimensionless momentum thickness growth rate vs. normalized momentum thickness for cases with seed #2	81
5.5.1	Dimensionless turbulent kinetic energy at the center of the layer vs. dimensionless time for low-amplitude Cases 4 and 6	82
5.5.2	R.M.S. values of the streamwise velocity fluctuation at the center of the mixing layer versus x/r_o . An $x/r_o = 6$ corresponds to T between 600 and 1200, depending on the initial boundary layer	82

5.5.3	R.M.S. values of the gradient velocity fluctuation at the center of the mixing layer versus x/r_0 . See caption of Fig. 5.2.2	83
5.5.4	Dimensionless turbulent kinetic energy at the center of the layer vs. normalized momentum thickness for low-amplitude Cases 4 and 6	83
5.5.5	Dimensionless turbulent kinetic energy at the center of the layer vs. normalized momentum thickness for medium-amplitude Cases 5, 7, 9, 10, and 11	84
5.5.6	Dimensionless turbulent kinetic energy at the center of the layer vs. normalized momentum thickness for high-amplitude Cases 2 and 8	84
5.6.1	Normalized turbulent kinetic energy profiles for Case 4 .	85
5.6.2	Normalized turbulent kinetic energy profiles for Case 11 .	85
5.6.3	Normalized turbulent kinetic energy profiles for Case 2 .	86
5.7.1	Normalized Reynolds stress tensor profiles for Case 6 at $T = 0$	87
5.7.2	Normalized Reynolds stress tensor profiles for Case 6 at $T = 83$	87
5.7.3	Normalized Reynolds stress tensor profiles for Case 6 at $T = 165$	88
5.7.4	Normalized Reynolds stress tensor profiles for Case 6 at $T = 246$	88
5.7.5	Normalized Reynolds stress tensor profiles for Case 6 at $T = 328$	89
5.7.6	Normalized Reynolds stress tensor profiles for Case 6 at $T = 418$	89
5.7.7	Normalized Reynolds stress tensor profiles for Case 6 at $T = 554$	90
5.7.8	Normalized Reynolds stress tensor profiles for Cases 5, 9, and 10 at $T = 0.0$	90
5.7.9	Normalized Reynolds stress tensor profiles for Case 7 at $T = 0.0$	91
5.7.10	Normalized Reynolds stress tensor profiles for Case 11 at $T = 0.0$	91
5.7.11	Normalized Reynolds stress tensor profiles for Case 5 at $T = 67$	92

5.7.12	Normalized Reynolds stress tensor profiles for Case 7 at T = 66	92
5.7.13	Normalized Reynolds stress tensor profiles for Case 9 at T = 66	93
5.7.14	Normalized Reynolds stress tensor profiles for Case 11 at T = 67	93
5.7.15	Normalized Reynolds stress tensor profiles for Case 5 at T = 132	94
5.7.16	Normalized Reynolds stress tensor profiles for Case 7 at T = 132	94
5.7.17	Normalized Reynolds stress tensor profiles for Case 9 at T = 131	95
5.7.18	Normalized Reynolds stress tensor profiles for Case 11 at T = 131	95
5.7.19	Normalized Reynolds stress tensor profiles for Case 5 at T = 197	96
5.7.20	Normalized Reynolds stress tensor profiles for Case 7 at T = 197	96
5.7.21	Normalized Reynolds stress tensor profiles for Case 9 at T = 197	97
5.7.22	Normalized Reynolds stress tensor profiles for Case 11 at T = 197	97
5.7.23	Normalized Reynolds stress tensor profiles for Case 5 at T = 295	98
5.7.24	Normalized Reynolds stress tensor profiles for Case 7 at T = 295	98
5.7.25	Normalized Reynolds stress tensor profiles for Case 7 at T = 379	99
5.7.26	Normalized Reynolds stress tensor profiles for Case 2 at T = 33	99
5.7.27	Normalized Reynolds stress tensor profiles for Case 8 at T = 33	100
5.7.28	Normalized Reynolds stress tensor profiles for Case 2 at T = 66	100
5.7.29	Normalized Reynolds stress tensor profiles for Case 8 at T = 66	101

5.7.30	Normalized Reynolds stress tensor profiles for Case 2 at $T = 99$	101
5.8.1	Time history of the anisotropy tensor B_{ij} for Case 4 . .	102
5.8.2	Time history of the anisotropy tensor B_{ij} for Case 6 . .	102
5.8.3	Time history of the anisotropy tensor B_{ij} for Case 5 . .	103
5.8.4	Time history of the anisotropy tensor B_{ij} for Case 7 . .	103
5.8.5	Time history of the anisotropy tensor B_{ij} for Case 9 . .	104
5.8.6	Time history of the anisotropy tensor B_{ij} for Case 10 .	104
5.8.7	Time history of the anisotropy tensor B_{ij} for Case 11 .	105
5.8.8	Time history of the anisotropy tensor B_{ij} for Case 2 . .	105
5.8.9	Time history of the anisotropy tensor B_{ij} for Case 8 . .	106
5.9.1	Correlation coefficient at the center of the layer vs. normalized momentum thickness for cases with seed #1 . . .	107
5.9.2	Correlation coefficient at the center of the layer vs. normalized momentum thickness for seed #2	107
5.9.3	Correlation coefficient at the center of the layer vs. normalized momentum thickness for low-amplitude Cases 4 and 6	108
5.9.4	Correlation coefficient at the center of the layer vs. normalized momentum thickness for medium-amplitude Cases 5, 7, 9, 10, and 11	108
5.9.5	Correlation coefficient at the center of the layer vs. normalized momentum thickness for high-amplitude Cases 2 and 8	109
5.10.1	Time history of alias-free accuracy and sample size parameters η_{AF} , η_A , and η_S	110
5.10.2	Time history of alias-free accuracy and sample size parameters η_{AF} , η_A , and η_S	110
5.10.3	Time history of alias-free accuracy and sample size parameters η_{AF} , η_A , and η_S	111
5.10.4	Time history of alias-free accuracy and sample size parameters η_{AF} , η_A , and η_S	111
5.10.5	Time history of alias-free accuracy and sample size parameters η_{AF} , η_A , and η_S	112

5.11.1	Plan view of particle tracking grid for all cases at $T = 0$	113
5.11.2	Plan view of particle tracking grid for Case 6 at $T = 161$.	113
5.11.3	Plan view of particle tracking grid for Case 6 at $T = 200$.	114
5.11.4	Plan view of particle tracking grid for Case 6 at $T = 280$.	114
5.11.5	Plan view of particle tracking grid for Case 6 at $T = 342$.	115
5.11.6	Span view of particle tracking grid for Case 6 at $T = 200$.	115
5.11.7	Span view of particle tracking grid for Case 6 at $T = 342$.	116
5.11.8	Plan view of particle tracking grid for Case 7 at $T = 177$.	116
5.11.9	Plan view of particle tracking grid for Case 8 at $T = 76$.	117
5.11.10	Plan view of particle tracking grid for Case 10 at $T = 76$.	117
5.11.11	Plan view of particle tracking grid for Case 10 at $T = 97$.	118
5.11.12	Plan view of particle tracking grid for Case 10 at $T = 151$.	118
5.11.13	Plan view of particle tracking grid for Case 10 at $T = 171$.	119
5.11.14	Plan view of particle tracking grid for Case 10 at $T = 231$.	119
5.11.15	Span view of particle tracking grid for Case 10 at $T = 231$.	120
5.11.16	Plan view of particle tracking grid for Case 9 at $T = 76$.	120
5.11.17	Plan view of particle tracking grid for Case 9 at $T = 220$.	121
5.11.18	Span view of particle tracking grid for Case 9 at $T = 220$.	121
5.11.19	Plan view of particle tracking grid for Case 11 at $T = 97$.	122
5.11.20	Plan view of particle tracking grid for Case 11 at $T = 151$.	122
5.11.21	Plan view of particle tracking grid for Case 11 at $T = 231$.	123
5.11.22	Span view of particle tracking grid for Case 11 at $T = 171$.	123
5.11.23	Span view of particle tracking grid for Case 11 at $T = 231$.	124
D.1	Schematic view of vortex pairing, image flow study	125

List of Tables

Table		Page
5.1	Descriptions of Cases Run	38
5.2	Definitions of Terms Used in Table 5.1	38

Nomenclature

Symbol

b_{ij}	Reynolds stress anisotropy tensor, $\langle \tilde{u}_i \tilde{u}_j \rangle / \langle \tilde{u}_\ell \tilde{u}_\ell \rangle - \frac{1}{3} \delta_{ij}$.
B_{ij}	$\int_{-\infty}^{\infty} b_{ij}(z) q^2(z) dz / \int_{-\infty}^{\infty} q^2(z) dz$
$c(uw)$	One-point correlation coefficient of the Reynolds shear stress.
$G(\underline{x}-\underline{x}')$	Gaussian spatial filter (see (2.5.4)).
h	Mapping function.
k	Wave number (integer in computation).
k_i	Wave number in the i^{th} direction (integer in computation).
L_i	Computational box length in the i^{th} direction.
p	Pressure.
\tilde{p}	The computational or modified pressure.
q^2	$\tilde{u}_i \tilde{u}_i$.
Re_δ	Reynolds number, $\Delta u \delta_\omega / \nu$.
R_{ij}	$\overline{u'_i \bar{u}_j} + \overline{\bar{u}_i u'_j} + \overline{u'_i u'_j}$.
S_{ij}	$\frac{1}{2} \left[\frac{\partial u_j}{\partial x_i} + \frac{\partial u_i}{\partial x_j} \right]$, u_i as noted where used.
t	Time.
T	Dimensionless time.
u	Streamwise velocity component (u_1).
u_i	The i^{th} velocity component.
\bar{u}_i	Large-scale (filtered) part of u_i .
u'_i	Subgrid-scale part of u_i .
\tilde{u}_i	$\bar{u}_i - \langle \bar{u}_i \rangle$.
$\Delta U = 2u_0$	Velocity difference across the mixing layer.

v	Spanwise velocity component (u_2).
w	Gradient velocity component (u_3).
x	Streamwise coordinate.
x_i	The i^{th} component of the Cartesian coordinates ($i = 1, 2, 3$).
y	Spanwise coordinate.
z	Gradient coordinate.

Greek Letters

α	Dimensionless wavenumber.
Δ_i	Filter width in the i^{th} direction.
δ_ω	Slope thickness of the mixing layer.
δ_{ij}	Kronecker delta.
ζ	Computational coordinate which maps to the physical coordinate z .
η_A	Accuracy measure.
η_{AF}	Alias-free measure.
η_S	Sample measure.
θ	Momentum thickness $\equiv \int_{-\infty}^{\infty} \left[\frac{1}{4} - \frac{\langle u \rangle^2}{\Delta U} \right] dz$.
Θ	θ/θ_0 ; θ_0 denotes the initial momentum thickness.
λ	Velocity difference across the mixing layer divided by the sum of the velocities on each side of the mixing layer.
λ_i	Disturbance wave length in the i^{th} direction.
ν	Kinematic viscosity.
ν_T	Subgrid-scale turbulent kinematic viscosity.
ρ	The fluid density.
τ_{ij}	$R_{ij} - \delta_{ij}R_{kk}/3$.
ω_i	The i^{th} component of the vorticity.

Symbol

$\langle \quad \rangle$ Denotes an average over a plane of homogeneity (plane of constant $z = x_3$).

$\overline{(\quad)}$ Denotes filtered quantity.

Chapter 1

INTRODUCTION

1.1 Background

Turbulent flows have been extensively studied, both experimentally and theoretically, for more than 50 years. The results of this effort still leave much that is unknown about the physics of turbulence, and our ability to predict its effects is still very limited. The theoretical difficulties are primarily due to two things: the nonlinearity of the governing equations and the large range of scales involved in high Reynolds number flows. The nonlinearity severely limits purely analytical solutions. The wide range of scales cannot be handled numerically by present or foreseeable computers, and hence full 3-D, time-dependent, computational solutions can be obtained only at very low Reynolds number.

Large eddy simulation (LES) offers one approach to escape these difficulties. The LES approach is to mathematically distinguish "large" and "subgrid" scale components of a turbulent flow field. The equations for the "large" scales can be derived by smoothing or "filtering" the Navier-Stokes equations; but, due to the nonlinearity, "subgrid" scale terms appear, and these must be modeled. The merit of the LES approach (which is applicable to high Reynolds number flow) is due to the concentration of energy in the large scales or, correspondingly, to the fact that the modeled terms have a relatively small fraction of the energy and the large eddies do most of transport.

LES is conceptually quite different from conventional phenomenological turbulence modeling, in which models for all scales of turbulence are required. See Reynolds (1976) for a review of those approaches. The limited success of modeling the entire turbulence field is understandable when one considers the lack of universality in the large scale motions, since experimental evidence shows that large scale structures are very different in different flows. The work of Kline et al. (1959) on boundary layers and of Roshko (1976) on free shear flows illustrates this point. It is generally believed that the small scales tend to be universal in structure and hence should be much easier to model.

It is also generally believed that large-scale structures contain most of the turbulent energy production and produce most of the important effects. The large scales are clearly dominant in transition of free shear layers (this can be proved analytically) and many researchers now believe this is also true far downstream (for example, see Browand and Troutt (1980) and Roshko (1976)).

Large eddy simulation is thus an important tool for obtaining detailed information about the most important turbulent motions. By examining the results of LES calculations, one can develop a deeper understanding of the physics of these flows. This insight should be useful in finding ways of controlling (to some degree) the effects of turbulence. Thus we believe that the most important aspect of LES goes beyond prediction and into the domain of control; Liepmann (1979) has also pointed out the importance of the large structures in controlling turbulence. LES can also help in guiding the development of simpler phenomenological models by providing quantitative "data" for terms that must be modeled in these theories.

The most impressive LES work to date has been the turbulent channel flow simulation of Moin and Kim (1981). This work clearly demonstrates the power of LES in providing both physical understanding and guidance for model development.

A computational approach related to LES is Full Turbulence Simulation (FTS), in which all of the scales of turbulent motion are computed in a 3-D, time-dependent calculation. With present computers, FTS is limited to low Reynolds numbers, when the large and small scales do not differ by more than one or two orders of magnitude. Nevertheless, FTS calculations are very useful, for they provide a testing ground for subgrid-scale models required in LES simulations, as well as physical insight and other "data" that are useful in developing phenomenological turbulence models. Examples of FTS calculation are Clark et al. (1977), Shirani et al. (1981), Feiereisen et al. (1981), and Orszag and Patterson (1972) and Rogallo (1981)

The present work deals principally with LES computation of a time-developing mixing layer. This required development of a new numerical method. The results provide new insight into the physical processes

that occur during the transition of this layer from laminar to turbulent flow.

1.2 Related Work

While the present work deals primarily with the LES approach, we shall now mention other computational approaches to gain perspective. In Reynolds' (1976) review, statistical methods are placed in a hierarchy ranging from algebraic to those in which five differential equations are used to model the turbulence. Following a discussion of these statistical approaches, vortex methods will also be mentioned.

Statistical approaches to treating turbulence generally employ a time average of the Navier-Stokes equations; occasionally other types of averaging are used. Time averaging the Navier-Stokes equations results in equations which govern the mean (time-averaged) velocity field. These equations contain higher-order terms--time-averaged products of the fluctuating field. By averaging moments of the Navier-Stokes equations, governing equations for the time-averaged products of the fluctuating field are obtained. These equations contain averages of triple products of the fluctuating field. This process always results in higher-order terms--more unknowns than equations regardless of how many moments one takes. This is known as the closure problem of turbulence.

To close the system of equations, a model or closure assumption which expresses the highest-order terms as some function of the lower-order terms is required. The lowest-order model, termed a zero equation model because no differential equations for the turbulence are employed, algebraically relates the turbulent stresses (Reynolds stresses) to the mean flow quantities. Modeling at this level often produces satisfactory results for the mean flow, and calculations require only a few seconds of computer time. The success at this level is due to the considerable empirical content.

The next level of modeling--a one-equation model--generally employs a differential equation for the turbulent kinetic energy and a prescribed length scale or dissipation rate. This level is limited by the skill of the prescriber.

Two-equation models--some of which use equations for the turbulent kinetic energy and one which uses a length or dissipation scale--are very popular. They are still postdictive, as considerable empirical input is required to obtain good results; but they can be made to work well for given classes of flows.

Full Reynolds stress models are used on occasion. At this level a differential equation is used for each component of the Reynolds stress tensor. While there is hope that such a model could be generally applicable, it is quite complicated. There are many empirical constants, and it is often hard to evaluate them.

Statistical methods can "predict" the statistical behavior of the mixing layer. The present study, however, is aimed at better understanding of the physics of the flow, and statistical approaches are not applicable. Approaches which are applicable are now presented.

Ashurst (1979) has used a vortex tracking method to study the spatially developing mixing layer. In this approximation, the vorticity is discretized into two-dimensional line vortices which are periodically released at the origin of the mixing layer. The filaments are convected by use of the Biot-Savart law. A random perturbation of the initial release of the vortices causes the vortices to coalesce to form large-scale vortex structures, which pair. An impressive color motion picture of this process was produced. The discretization approximation used is reasonable, though the 2-D approximation is quite limiting. The most ad-hoc assumption is the method of introducing artificial dissipation. This is necessary to prevent an unphysical growth in the kinetic energy. This approach is quite simple, fairly costly, and has an advantage over LES in terms of simplicity of the inflow and outflow boundary conditions and capability of treating a large region of the spatially developing mixing layer.

This approach can be extended to three-dimensions, as shown by Leonard (1980) for a boundary layer. The full three-dimensional calculations are very costly, and we shall now discuss the vortex in cell method, which greatly reduces the cost.

Couet and Leonard (1980) used the vortex in cell method to perform a three-dimensional simulation of the time-developing mixing layer. In

this approach, three-dimensional vortex filaments are tracked. In place of the costly Biot-Savart method of tracking vortex filaments, the vorticity is interpolated onto a fixed grid. The grid values of the vorticity are used as a source for a Poisson equation for the vector potential whose curl gives the velocity field at the grid nodes. This velocity field is then interpolated to the vortex filaments' positions, and the vortex filaments are convected to new locations. The cost is much lower than that for the Biot-Savart method. Couet and Leonard (1980) has developed a method of analytically continuing boundary conditions at infinity onto the edges of a finite grid, which eliminates image-flow problems (see Appendix D).

Couet's work produced good visualizations of the vortex formation, the existence of a secondary instability, and vortex pairing. He also studied the energy history of individual turbulence modes, but there is concern that the numerical methods used did not treat the conserved properties correctly.

In an FTS, Metcalfe and Riley (1980) simulated a turbulent mixing layer. Their full simulation required a 64^3 grid for adequate resolution in a stream and spanwise domain the same size as in the present work. They were restricted to a layer thickening by a factor of five or six, due to uniformly spaced grid in the gradient direction (the direction of the mean velocity gradient). Other than the treatment of the gradient direction, their numerics are very similar to those of the present work. Metcalfe and Riley's work demonstrates the capability of a full simulation to predict reasonably the mean velocity profile, growth rate, and turbulent energy of a time-developing mixing layer.

Now we shall turn our attention to experimental work on mixing layers. This is by no means a complete listing, but rather a few works on different aspects of the mixing layer. Reference to particular results relevant to the present work are given in Chapter 5.

In a study of nonlinear eigenfunction interactions in transition, Miksad (1972, 1973) forced a laminar mixing layer at two forcing frequencies. Bradshaw (1966) studied the effect of initial conditions on the near field of a one-stream mixing layer by altering the geometry. Good sources of turbulence statistics in a mixing layer include: Spencer

and Jones (1971), Wygnanski and Fiedler (1970), Patel (1973), and Champagne et al. (1976). The asymptotic growth rate of the mixing layer is reviewed by Birch (1980). Visualization of the mixing layer includes the work of Brown and Roshko (1974), Winant and Browand (1974), and Chandrsuda et al. (1978).

1.3 Motivation and Objectives

The basic motivation for the present work is the desire to better understand the importance of large scale structures in free shear flows through study of accurate, 3-D, time-dependent simulations of the formation of such structures. Most previous computational work on this problem was 2-D and often only the linearized equations were used. Recently, Metcalfe and Riley (1980) published one of the first three-dimensional simulations. To compute accurately the transition process accurately up to the point at which the energy reaches the experimentally measured levels for "fully developed" turbulence, the full non-linear equations must be used. Due to the fact, established analytically, that transition or "near field" turbulence in the free shear layer is strongly dominated by a relatively small range of scales, this is a problem well suited to numerical simulation.

To perform a simulation, we require knowledge of the flow field at the boundaries of the domain of interest. Often, this is a major stumbling block, as the boundary conditions at one or more boundaries of the computational region may be unknown.

To illustrate this point, consider the plane mixing layer. In the laboratory flow (see Fig. 1.3.1), two fluid streams moving at different velocities are initially separated by a splitter plate. At the end of the splitter plate the two streams form a free shear layer. This shear layer thickens with downstream distance.

Experiments and theoretical analysis show that transition occurs through growth of a primary (Kelvin-Helmholtz) instability. This leads to the formation of spanwise vortex structures. These in turn create a strong straining field between adjacent vortices, and in this region a secondary instability leads to the formation of counter-rotating vortices aligned with the strain. Pairing of the spanwise vortices is an

important mechanism in the formation of structures of larger scale. Far downstream the mean velocity profile becomes self-similar, although quite different rates of growth have been found in different experiments.

To simulate this flow, time-dependent inflow and outflow boundary conditions need to be imposed. Laboratory experiments never provide these in sufficient detail. Artificial conditions could be imposed, but then there would be several grid points near both the inlet and the outlet where the computed solution would be unphysical. Hence a very long computational domain would be required; this approach is possible on the largest computers, but at very great cost.

To avoid these problems with boundary conditions, we have chosen to treat a simpler problem, namely, the time-developing mixing layer (see Fig. 1.3.2). In the time-developing mixing layer, two semi-infinite streams of fluid travel in opposite directions with equal speed. The shear layer at the interface of these two streams thickens in time. This flow is statistically homogeneous in planes parallel to the interface. Hence, periodic boundary conditions can be applied in the two coordinate directions in the plane of homogeneity.

Because the layer is immersed in an infinite region, some means of handling boundary conditions infinitely far above and below the layer is required. This could be done by applying free-stream conditions at a large but finite distance from the layer. However, this introduces "imaging errors" (Appendix D). Instead, we shall use a method involving a non-uniform grid that extends to infinity above and below the layer. This requires the development of a new numerical method, which represents one of the important contributions of this work.

Let us consider the relationship between this idealized flow and the laboratory flow. The laboratory flow is characterized by a parameter λ , defined by

$$\lambda = (U_1 - U_2)/(U_1 + U_2)$$

where U_1 and U_2 are the speeds of the two streams. As λ goes to zero, all streamwise mean gradients become smaller, and the space-

developing layer becomes more like the time-developing one. Unfortunately, when λ is small, the early part of the flow is dominated by the wake of the splitter plate and is not really a mixing layer flow. Hence, we cannot make a direct comparison of the simulation with experiments. Nevertheless, we believe that the basic physical processes are the same in both flows, and hence can be examined by study of the time-developing flow. The most significant exception is that, in the laboratory flow, the downstream flow can affect the upstream flow by creating pressure fluctuations. This allows "phase locking," a situation in which the flow remains in a particular configuration for a long time.

Simulation of the time-developing flow requires initial conditions. The effect of different initial conditions in the time-developing flow is probably similar to the effect of different upstream conditions in the laboratory flow. The sensitivity of the near field of the mixing layer to initial conditions was examined in the laboratory by Bradshaw (1966). He found the near field to be quite sensitive to changes in the initial disturbance field. In this laboratory study, the initial disturbance field was altered by geometry changes affecting the boundary layer of the one-stream mixing layer.

In the computer simulation we can specify any initial field that is consistent with a few simple constraints, and hence we can examine the effects of changing specific features of the initial disturbance. All computational cases will begin with the same mean field; for each case, a specific disturbance field will be added to complete the initial condition. Changes in the initial disturbance field to be considered include: amplitude, spectrum shape, and the set of random phases of the modes.

After a sufficient period of development, we expect that the mean (phase-averaged) velocity profile will become self-similar. The rate at which this occurs, and the degree of self-similarity in other turbulence parameters of the time-developing flow should provide insight into the self-similarity (or lack thereof) in the laboratory flow.

Summarizing, the objectives of this work are thus:

- To develop an accurate method of differentiation and integration on a non-uniform grid, suitable for simulating a time-developing mixing layer.
- To employ the above method in a study of simulations of the transition and early turbulence domains of a time-developing mixing layer.

1.4 Summary of Present Work

A new and very accurate numerical differencing and integrating scheme for infinite domains is presented. It is based on the use of Fourier expansions and takes advantage of the computational efficiency of the fast Fourier transform. The new method is applicable to more general boundary conditions than the standard Fourier method, due to the use of mapping functions. (The simplest boundary conditions to implement are periodicity, or zero, or zero-derivative conditions, or combinations thereof.) However, the allowed mapping functions are restricted for reasons of efficiency and accuracy. For more detail, see Chapter 3.

Two particular mapping schemes, both for doubly infinite domains, are implemented. One is chosen to handle jet-type flows, while the other is designed for the mixing layer. Both schemes are applied to linear test equations having known analytical solutions. The new scheme is shown to have errors as much as six orders of magnitude smaller than common finite-difference schemes for equal numbers of mesh points.

The new scheme designed for jet-type flows is used to demonstrate the influence of finite-domain boundary conditions. The evaluation was made by use of an array of two-dimensional vortex structures, all with the same sign of vorticity. If this array of vortices is computed in a finite domain with no-stress boundary conditions applied to a surface parallel to the array, but at a finite distance, image flows are implied. The nearest image flow above is the mirror image (imaged about the no-stress surface) of the initial vortex array. This image vortex array and the true vortex array form a near-field jet-type flow, and their behavior in time was computed using the new infinite-domain

scheme. Comparing a base computation with one in which the image array was shifted in the streamwise direction (relative to the true array) showed potentially strong coupling to image flows, depending on vertical spacing. For details, see Appendix D.

Using the new infinite-domain scheme, a 3-D, time-dependent, large eddy simulation study of transition and early turbulence in a time-developing mixing layer was undertaken. The primary focus of this study concerns the effect of the initial disturbance field on turbulence development. Effects due to filtering and modeling are also examined.

To sort out the effects of the initial disturbance field, the same laminar, mean-velocity profile is used as the initial mean field in all cases. To this mean velocity field, an initial divergence-free disturbance field is added. We use nine cases involving seven different initial disturbance fields. These seven cases examine the influence of the disturbance amplitude, spectrum shape, and random phase sets on the resulting early turbulence.

The computations provide the mean velocity profile, the momentum thickness, the turbulent kinetic energy, the Reynolds stress tensor, the Reynolds stress anisotropy tensor, and particle tracking pictures. Examination of these results provides better understanding of the mixing layer. The central observations from these computations are as follows:

- All cases display immediate self-similarity in the mean velocity profile.
- The momentum-thickness growth rate is strongly influenced by the initial disturbance-spectrum shape.
- Interesting oscillatory behavior is observed in the kinetic energy profile width for the small-amplitude initial disturbance cases. This oscillatory behavior is not present in high-amplitude initial disturbance cases.
- The anisotropy tensor proved to be the most sensitive measure of self-similarity. Even changing the random phase distribution in the initial disturbance field produced enormous differences in the evolution of the anisotropy tensor.

Probably the most significant aspect of the study was revealed in the particle-track pictures. While large coherent structures readily

appeared (some similar to those of Winant and Browand (1974) and others like Chandrsuda et al. (1978), the mechanism for producing the secondary instability has been identified. It seems to be the result of spanwise variations in the strength or position of the primary vortex structures, which give rise to spanwise variations in the straining field stagnation line. This causes spanwise vorticity to be tilted towards the streamwise direction as the vorticity is rolled up by the primary vortices, and this process leads to the formation of pairs of counter-rotating vortices aligned with the straining field.

Changing the set of random phases of the initial disturbance field produced significantly different results, both in the statistical and structural characteristics of the mixing layer. This is a consequence of the small sample of large eddies in any given calculation. The implications of this are still very significant, however, as any given experimental apparatus is likely to produce a given type of large eddy structure, which locks on. This is due to the likelihood of a fixed type of initial disturbance being present and also due to pressure feedback effects. However, different experimental apparatus is likely to lock onto different large eddy types. There are two and perhaps more different large eddy patterns which are possible. Thus, large eddy variation may be small in a given experiment, but significant variations may occur from experiment to experiment.

Two cases were run to examine the effects of filtering and subgrid turbulence modeling. We found that filtering delays the onset of non-linear effects and gives us less than the total picture. However, it considerably extends the length of time over which the computation is meaningful. The subgrid-scale model was shown to have very little influence on the calculations.

Chapter 2

PROBLEM FORMULATION

2.1 Governing Equations

We shall restrict ourselves to considering the motion of an incompressible Newtonian fluid. The motion of such a fluid is governed by the Navier-Stokes equations. A common form of these equations is:

$$\frac{\partial u_i}{\partial t} + \frac{\partial(u_i u_j)}{\partial x_j} = -\frac{1}{\rho} \frac{\partial p}{\partial x_i} + \nu \nabla^2 u_i \quad (2.1.1a)$$

For computational conservation* of important properties the equations are written in the form:

$$\frac{\partial u_i}{\partial t} + u_j \frac{\partial u_i}{\partial x_j} - u_j \frac{\partial u_j}{\partial x_i} = -\frac{\partial p}{\partial x_i} + \nu \nabla^2 u_i \quad (2.1.1b)$$

The modified pressure is $P = (p/\rho) + (u_i u_i/2)$. The equation for conservation of mass of an incompressible fluid is:

$$\frac{\partial u_i}{\partial x_i} = 0 \quad (2.1.2a)$$

For computational convenience we take divergence of (2.1.1b) and enforce (2.1.2a) to get a Poisson equation for the modified pressure:

$$\nabla^2 P = -\frac{\partial u_j}{\partial x_i} \frac{\partial u_i}{\partial x_j} + \frac{\partial u_j}{\partial x_i} \frac{\partial u_j}{\partial x_i} + u_j \frac{\partial^2 u_j}{\partial x_i^2} \quad (2.1.1b)$$

Thus, given the velocity of a fluid field at some time t_0 , we may solve (2.1.2b) for the modified pressure and then find the time rate of change of the velocity field from (2.1.1a). From this, we can find the velocity at the next time step.

*This form allows many differencing schemes to conserve mass, momentum, and energy (as shown by Mansour et al., 1977).

2.2 Boundary Conditions

The boundary condition imposed on the time-developing flow in directions of statistical homogeneity is that all variables be periodic:

$$u_1(x,y,z) = u_1(x+L_1,y,z) \quad (2.2.1a)$$

$$u_1(x,y,z) = u_1(x,y+L_2,z) \quad (2.2.1b)$$

In the direction of inhomogeneity, we can require that the flow become the unperturbed free stream far from the shear layer, or, alternatively, we can impose the no-stress conditions:

$$\left. \frac{\partial u}{\partial z} (x,y,z) \right|_{z=\pm\infty} = 0 = \left. \frac{\partial v}{\partial z} (x,y,z) \right|_{z=\pm\infty} ; w(x,y,\pm\infty) = 0 \quad (2.2.1c)$$

The no-stress condition is advantageous numerically and is employed in the present work.

2.3 Initial Conditions

The initial velocity field used consists of a laminar field plus small perturbations. The time-developing laminar mixing layer has gradients only in the z direction, and only the u component of the velocity field is nonzero. This layer is thus governed by the diffusion equation:

$$\frac{\partial u}{\partial t} = \nu \frac{\partial^2 u}{\partial z^2} \quad (2.3.1)$$

With the no-stress boundary condition and initial condition $u(z,0) = u_0$ for $z > 0$ and $u(z,0) = -u_0$ for $z < 0$, Eq. (2.3.1) has the solution

$$u(x,y,z,t) = u_0 \operatorname{erf}(z/\sqrt{4\nu t}) \quad (2.3.2)$$

The slope thickness, δ_w , of a free shear layer is defined as the velocity difference across the layer divided by the maximum gradient of the layer. For the laminar layer:

$$\delta_{\omega} = \sqrt{4\pi\nu t} \quad (2.3.3)$$

For our study of transition, we shall start our calculation at a time at which $Re_{\delta} = 2u_0\delta_{\omega}/\nu = 60$.

The disturbance field is constructed in the following way. First, a periodic, divergence-free, homogeneous, isotropic field on a $16 \times 16 \times 16$ grid is constructed using the routine written by Kwak et al. (1975). The velocities on five planes of this field are assigned to the central five planes of the grid used in the present calculation (which is non-uniform and anisotropic). This field is then smoothed in the gradient direction by a Gaussian filter; the result is smooth, but not divergence-free. We obtain a divergence-free field by taking the curl of this field. The divergence-free velocity field is added to the error-function profile to give the complete initial field. Further details of this process are given in Chapters 3 and 5.

2.4 The Computational Domain

The choice of a streamwise and spanwise box length (L_1 and L_2 , respectively) is critical. Michalke (1965) and Betchov and Criminale (1967) studied the stability characteristics of a mixing layer with a hyperbolic tangent profile. While our error function profile is not identical to theirs, it is sufficiently close that we can use their results as a guide. Betchov and Criminale considered the linearized Navier-Stokes equations (valid for small amplitude disturbances) and searched for eigensolutions growing in time. They found, even in the limit of infinite Reynolds number, that there is a minimum wavelength λ_{1c} in the streamwise direction for which the disturbance is amplified by the mean shear; any disturbance with a shorter wavelength will decay. In non-dimensional terms at infinite Reynolds number, the shortest amplified wave has a wavenumber

$$\alpha_c \equiv \frac{\pi\delta_{\omega}}{\lambda_{1c}} = 1.0 \quad (2.4.1)$$

According to Betchov and Criminale, the most amplified disturbance wave length at infinite Reynolds number corresponds to wavenumber $\alpha_m = 0.43$.

The effect of finite Reynolds number is to decrease the values of α_c and α_m ; at the Reynolds number we shall use, $\alpha_m = 0.34$. Using these considerations as a guide, we set the computational domain such that the smallest α supported in the calculation was 0.17. This corresponds to the longest wave allowed--the one whose wavelength is the computational box length. Since we are using Fourier methods, we have adequate resolution and a large enough domain to study the most amplified waves. At our initial Reynolds number ($Re_\delta = 60$) and with a grid spacing in the span direction equal to the streamwise grid, there are 14 amplified modes in our discrete approximation (this includes 3-D modes).

2.5 Filtering

In treating a turbulent flow numerically, we may have more scales of motion than any computer can handle; this depends somewhat on the flow and Reynolds number. If this is the case, we are forced to filter the flow field in a way which leaves a range of scales that can be computed. We follow Leonard (1974), who first formalized this approach. Since we know from experiments that the largest scales of motion are the most energetic ones and are responsible for most of the transport, we shall truncate the small scales. We shall symbolize the large-scale field by \bar{u} . For a homogeneous flow, we define it as:

$$\bar{u}(x) = \int G(\underline{x}-\underline{x}') u(\underline{x}') d\underline{x}' \quad (2.5.1)$$

(integration over all space). The small-scale or subgrid (SGS) field is simply the difference between the full field and the large-scale field.

$$u' = u - \bar{u} \quad (2.5.2)$$

Note that, since $\bar{\bar{u}} \neq \bar{u}$, $\bar{u}' \neq 0$.

The choice of a difference kernel for the filter function has two assets. Most importantly, such a filter commutes with differentiation operators. This means that both the large-scale field \bar{u} and the subgrid scale (SGS) field u' will separately satisfy the continuity

equation. The second asset of a difference kernel for the filter results from the convolution theorem. Discrete Fourier methods can be used in our problem, and the convolution theorem allows a very fast way of computing \overline{u} by means of the Fourier transform. The transform of \overline{u} is:

$$\hat{\overline{u}}(k) = \hat{G}(k) \hat{u}(k) \quad (2.5.3)$$

and \overline{u} is obtained by inverting (2.5.3).

Our choice for $G(\underline{x}-\underline{x}')$ is a Gaussian (see Mansour et al., 1977):

$$G(\underline{x}-\underline{x}') = \prod_{i=1}^n \left(\frac{6}{\pi \Delta_i} \right)^{1/2} \exp \left[-6(\underline{x}_i - \underline{x}'_i)^2 / \Delta_i^2 \right] \quad (2.5.4)$$

with $\Delta_i = 2h_i$, where h_i is the grid spacing in the i^{th} direction, and n is the number of directions in which we elect to filter. It should be noted that the discrete transform of (2.5.4) is used in (2.5.3). This is slightly different from the continuous transform.

We are using a non-uniform grid scheme in the z or x_3 direction. Moin et al. (1978) showed that it is difficult to define a filter for this direction. One can introduce an approximation, but the large and SGS flow fields would no longer be divergence-free. Thus we do not filter at all in the x_3 direction. If we apply the filter to (2.1.2a) in only the x_1 and x_2 directions ($n = 2$), we get

$$\frac{\partial \overline{u}_1}{\partial x_1} = 0 \quad (2.5.5)$$

Recalling $u_1 = \overline{u}_1 + u'_1$, Eqs. (2.1.2a) and (2.5.5) imply that the subgrid-scale field is divergence-free as well. This demonstrates the desirability of a linear filtering operator which commutes with differentiation.

Application of the filter to (2.1.1b) gives

$$\frac{\partial}{\partial t} \overline{u}_1 + \overline{u}_j \frac{\partial \overline{u}_1}{\partial x_j} - \overline{u}_j \frac{\partial \overline{u}_j}{\partial x_1} = - \frac{\partial \overline{P}}{\partial x_1} + \nu \nabla^2 \overline{u}_1 - \frac{\partial}{\partial x_j} \tau_{1j} \quad (2.5.6)$$

where

$$\begin{aligned}\tau_{ij} &= R_{ij} - R_{kk} \frac{\delta_{ij}}{3} \\ \bar{P} &= \frac{\bar{p}}{\rho} + \frac{R_{kk}}{3} + \frac{1}{2} \overline{(\bar{u}_i \bar{u}_i)} \\ R_{ij} &= \overline{u'_i u'_j} + \overline{\bar{u}_i u'_j} + \overline{u'_i \bar{u}_j}\end{aligned}$$

Note that τ_{ij} contains subgrid-scale terms and therefore must be modeled.

Taking the divergence of Eq. (2.5.6) and enforcing Eq. (2.5.5) gives a Poisson equation for the filtered modified pressure:

$$\nabla^2 \bar{P} = \frac{\partial \bar{u}_j}{\partial x_i} \frac{\partial \bar{u}_i}{\partial x_j} + \bar{u}_j \frac{\partial^2}{\partial x_i^2} \bar{u}_j - \frac{\partial}{\partial x_i} \frac{\partial}{\partial x_j} \tau_{ij} \quad (2.5.7)$$

Since filtering is a linear operator and all boundary conditions are linear, we arrive at the following boundary conditions on the large-scale field:

$$\bar{u}_i(x, y, z) = \bar{u}_i(x + L_1, y, z) \quad (2.5.8)$$

$$\bar{u}_i(x, y, z) = \bar{u}_i(x, y + L_2, z) \quad (2.5.9)$$

$$\left. \frac{\partial \bar{u}}{\partial z} (x, y, z) \right|_{z=\pm\infty} = 0 = \left. \frac{\partial \bar{v}}{\partial z} (x, y, z) \right|_{z=\pm\infty} ; \quad \bar{w}(x, y, \pm\infty) = 0 \quad (2.5.10)$$

2.6 Subgrid Modeling

Since τ_{ij} contains subgrid-scale terms, it must be modeled. The history of how we came to the model eventually used is of some interest.

In a preliminary phase of this work, we explored the fully turbulent mixing layer. We solved the vorticity equations using the vorticity model developed by Mansour et al. (1978). We also used the primitive equations with the following model, due to Smagorinsky (1963):

$$\tau_{ij} = -2\nu_T \bar{S}_{ij}$$

$$\begin{aligned}\bar{s}_{ij} &= \frac{1}{2} \left[\frac{\partial}{\partial x_i} \bar{u}_j + \frac{\partial}{\partial x_j} \bar{u}_i \right] \\ v_T &= (C_s \Delta)^2 \left(2\bar{s}_{ij}\bar{s}_{ij} \right)^{1/2}\end{aligned}\tag{2.6.1}$$

In (2.6.1), Δ is the filter width and C_s is a constant, approximately 0.2. Runs with the same initial conditions--one using the primitive equations and Smagorinsky's model and another using the vorticity equations and Mansour's model--had turbulent statistics which were essentially identical. In both runs, however, the mixing layer thickened much faster than the experimental layer. In an attempt to understand why, we then used Smagorinsky's model in a calculation of an initially laminar mixing layer with no disturbance added, and found that the layer grew between two and three times as fast as the experimental turbulent layer. This erroneous behavior provided the clues needed to modify the model, and led to an improved model that we used in the transition studies.

One reason for the improper behavior in laminar flow arises because the model "turns on" too quickly. The models are supposed to account for the effects of unresolved turbulence, but the eddy viscosity contains a significant contribution from the mean field. Hence, in a laminar flow with no turbulence, these models incorrectly provide eddy viscosity and hence subgrid stresses. A model that allows the subgrid stresses to build up slowly with the turbulence field can be made by redefining v_T as

$$v_T = (C_s \Delta)^2 \left[2(\bar{s}_{ij} - \langle \bar{s}_{ij} \rangle)(\bar{s}_{ij} - \langle \bar{s}_{ij} \rangle) \right]^{1/2}\tag{2.6.2}$$

where the $\langle \rangle$ denotes an average over a plane of constant z .

All model calculations reported here use v_T given by (2.6.2). Another modeling concept is presented in Appendix C; work by Bardina et al. (1980) suggests that this new model is very promising.

The problem with too-rapid growth of the turbulent layer was also related to the grid layout. The stability considerations discussed in Section 2.4 require a grid spacing that is very large in the streamwise

and spanwise directions (the only directions in which we filter); in fact, the spacing is large compared to the thickness of the layer, and hence the filter width was much larger than the layer thickness. Phenomenological models typically use length scales for the large eddies that are about one-tenth the shear layer thickness; this is far shorter than our filter width. Hence, we limited our length scale Δ to a maximum of one-tenth of the shear layer thickness $\Delta_1 = \min(2h_1, \delta_w/10)$.

2.7 Summary

In summary, in the mixing layer transition study we solve the equation for the filtered field \overline{u} (2.5.5 and 2.5.6) using the subgrid model (2.6.1) with v_T from (2.6.2). The filter (2.5.4) was used, and its width Δ_1 was $2h_1$. The boundary conditions (2.5.8-10) were applied. The initial velocity field consisted of a laminar mean field (2.3.2) with $Re_\delta = 60$, plus a divergence-free random perturbation (see Chs. 3 and 5). The computational domain was chosen to allow a number of the amplified modes of the laminar instability to appear in the solution, including the most rapidly growing mode.

At this point, the global problem formulation is complete. We now proceed to the details of the numerical method used.

Chapter 3

NUMERICAL METHODS

3.1 Preview

Some familiar and some new numerical methods are used in this work. To orient the reader, we shall briefly preview the methods to be discussed in this chapter.

Our choices of numerical methods were guided by the objectives of this study. Desirable methods preserve as much of the physics as possible, and this requires accurate numerical representation of the spatial derivatives. Fourier methods provide the most accurate differentiation for a given number of grid points; hence we used them wherever possible.

Since periodic boundary conditions are applied in two directions, (x_1 and x_2), we can use the standard Fourier scheme (described in the next section) to treat spatial derivatives in those directions. The gradient (x_3) direction requires special consideration; we were concerned about the influence of image flows, which are discussed in Appendix D. To avoid imaging problems, we chose to compute the solution over infinite x_3 . For reasons of accuracy we wanted a discrete orthogonal function expansion method which could treat an infinite region. Since no existing method was known, we developed a mapping scheme which retains the efficiency of the fast Fourier transform (FFT) and is ideally suited to our problem as well as several others. This method is described in Sections 3.3 and 3.4.

New measures of spatial resolution and statistical validity in Fourier methods were developed (Section 3.5) and used to quantify the accuracy and statistical validity of the calculations. These are described in Section 3.5.

To aid the understanding of the physics, computational flow visualization is used. The visualization is achieved by tracking the intersections of a freely deforming grid. While this is similar to particle tracking, it differs in that the identity of the individual particles is

retained. Interpolation of the velocity field is required for tracking the intersections, and this is presented in Section 3.6.

Recall that the initial field consists of a laminar mean field plus a random disturbance. The method of constructing the initial divergence-free disturbance velocity field is described in Section 3.7.

Three time-advance schemes were used in parts of this study. The transition problem has a disturbance velocity field which grows by orders of magnitude during the simulation. For this reason, a time-advance scheme which allows the time step size to change continually will be advantageous. To maintain accuracy, we want an explicit scheme of fairly high order. The fourth-order Runge-Kutta method (Appendix B.2) is ideal. It satisfies the above conditions and has excellent stability characteristics as well. All of our numerical studies of transition used this method for time-advance of the velocity field.

To advance the particle positions in time, we require less accuracy, since this is used for visualization purposes only. We still require a scheme which allows continual adjustment of the time step and has moderate accuracy. The second-order Runge-Kutta scheme (Appendix B.3) was chosen for this problem.

In addition, some computational experiments discussed in Appendix D were carried out using the second-order Adams-Bashforth method for time advance (Appendix B.1).

3.2 Standard Fourier Methods

The discrete Fourier transform is defined for any number of grid points; however, efficient algorithms usually limit the number of points to particular integers. In the most popular routines due to Cooley and Tukey (1965), this number must be a power of two; the Winograd (1976) method allows other numbers to be used, but has not yet seen extensive application. Thus, we consider only variations of the Cooley-Tukey algorithm.

If we have a function defined on a set of uniformly spaced grid points, say $x_n = (n-1)/N$, the discrete Fourier transform can be defined by:

$$\hat{f}_k = \sum_{n=1}^N f(x_n) e^{ik2\pi x_n} \quad (3.2.1)$$

We shall assume $N = 2^m$. There is a great deal of freedom in the choice of wavenumbers k used in Eq. (3.2.1). (This formulation gives integer wavenumbers). So long as we are interested only in representing the function on the grid points, the choice (within the allowed bounds) is irrelevant. However, when we use the fast Fourier transform (FFT) as a means of obtaining derivatives we are regarding Eq. (3.2.1) as an interpolation, and it is important to choose the wavenumbers which give the smoothest interpolation possible. For an even number of grid points, there are two equally good choices:

$$k = -\frac{N}{2}, -\frac{N}{2} + 1, \dots, \frac{N}{2} - 1$$

or

$$k = -\frac{N}{2} + 1, -\frac{N}{2} + 2, \dots, \frac{N}{2}$$

Either of these choices means that the wavenumber $|k| = N/2$ is represented only by a single waveform, whereas all other wavenumbers have two waveforms, i.e., $\pm k$. As a result, we have incomplete information about the highest wavenumber component, in fact, we know neither its phase nor its amplitude. Consequently, we cannot differentiate it. Most workers set its derivative equal to zero to avoid the problem. (This problem does not occur with odd-point transforms.) The derivative is thus:

$$\left. \frac{df}{dx} \right|_{x_n} = \frac{1}{N} \sum_{k=-N/2}^{N/2-1} 2\pi i k' \hat{f}_k e^{ik2\pi x_n} \quad (3.2.2)$$

where

$$k' = k ; \quad |k| \neq N/2$$

$$k' = 0 ; \quad |k| = N/2$$

3.3 Fourier Transforms on Non-Uniform Grids

The usual method of dealing with an infinite region involves mapping it onto a finite region. Mappings are also commonly used to modify the geometry such that the function is smoother in the transformed coordinate system. Mappings invariably complicate the equations to be solved, but they offer the important advantage that numerical methods are both more easily applied and more accurate in the transformed coordinate system. These advantages almost always outweigh the disadvantages, and coordinate transformations are a standard part of numerical methods today. Indeed, the development of better mappings is a major field of research.

In describing the new method, we shall restrict our attention to one-dimensional problems. Suppose that z is the physical coordinate and we introduce the computational coordinate ζ by means of the mapping

$$z = h(\zeta) \quad (3.3.1)$$

The derivatives in the two coordinate systems are related via the chain rule:

$$\frac{df}{dz} = \frac{df}{d\zeta} \frac{d\zeta}{dz} = \frac{1}{h'} \frac{df}{d\zeta} \quad (3.3.2)$$

Now, suppose that we choose to represent the function in the transformed coordinate system in terms of its values on a uniformly spaced grid $\zeta_j = j\Delta\zeta$. This function can be represented in terms of its Fourier transform in the manner described in the previous section. Thus, we can write:

$$f(\zeta_j) = \frac{1}{N} \sum_{k=-N/2}^{N/2-1} \hat{f}_k e^{ik2\pi\zeta_j} \quad (3.3.3)$$

We could use this Fourier transform to compute the derivative $df/d\zeta$ that appears in Eq. (3.2.2). One could then substitute the result into Eq. (3.3.3) and compute df/dz . The difficulties with this approach are (1) that, in general, the result contains a considerable aliasing or truncation error, and (2) that the resulting operator cannot

be inverted when the number of points used is even. Thus we must seek further improvements.

To look into this more deeply, we begin by noting that $1/h'(\zeta)$, which appears in Eq. (3.3.2), can itself be represented as a discrete Fourier series similar to the one in Eq. (3.3.3). In general, N terms will be needed and, when this series is multiplied by the one representing $df/d\zeta$, the result will contain $2N$ wavenumbers, $-N, \dots, N-1$. Truncating the result to N terms produces the truncation error alluded to above.

The problem can be avoided by restricting the allowed mapping functions to those which contain only a few Fourier modes with small wavenumbers. Thus, we can write:

$$\frac{1}{h'(\zeta)} = \sum_{k=-m}^m \hat{a}_k e^{ik2\pi\zeta} ; \quad m \ll \frac{N}{2} \quad (3.3.4)$$

When this is substituted into Eq. (3.3.2), the result contains $N + 2m$ wavenumbers. By making m small and truncating the modes whose wavenumbers are less than $-N/2 + 1$ or greater than $N/2 - 1$, we produce a small, acceptable amount of truncation error; doing this accurately requires that the multiplication of $1/h'$ and $df/d\zeta$ be carried out in Fourier space. It is possible to take the product in configuration space; however, the result will be aliased and will populate the $\pm N/2$ modes and thereby make the inverse of the differentiation operator singular. Defining the derivative via the truncated transform-space product allows us to construct an integral operator which is the "exact inverse" of the differentiation operator. By "exact inverse" we mean that the derivative of the integral of f is exactly f . Note that these are alias-free operators.

We now apply these ideas to two mappings suitable for free shear layer problems in fluid mechanics. The problems of interest are best treated in infinite domains.* For example, in the computation of plane jet flow the region of interest is doubly infinite in the gradient

*See Appendix D for a demonstration of the danger of using a finite domain to study vortex pairing.

direction, the boundary conditions are identical at $\pm \infty$, and we would like the grid points to cluster near the origin. The cotangent is a suitable mapping function for this purpose, i.e.,

$$z = h(\zeta) = -a \cotan(\pi\zeta) ; \quad 0 \leq \zeta < 1 , \quad -\infty \leq z < \infty \quad (3.3.5)$$

This gives the metric

$$\frac{1}{h'} = \frac{1}{\pi a} \sin^2(\pi\zeta) = \frac{1}{2\pi a} \left[1 - \frac{(e^{i2\pi\zeta} + e^{-i2\pi\zeta})}{2} \right] \quad (3.3.6)$$

Recalling Eq. (3.3.4), we see that $m = 1$ and the Fourier coefficients of the metric are:

$$\hat{a}_1 = \hat{a}_{-1} = -\frac{1}{4\pi a} , \quad \hat{a}_0 = \frac{1}{2\pi a} \quad (3.3.7)$$

We thus have grid clustering near the origin and a minimum of truncation error, since $m = 1$. An estimate of the error in the derivative of $f(z)$ is given by

$$\epsilon \approx \frac{2}{N} \left| 2\pi \left(\frac{N}{2} - 1 \right) \hat{a}_1 \hat{f}_{N/2-1} \right| \quad (3.3.8)$$

This error will be small if the Fourier series for $f(z)$ converges rapidly. The mapping above is applied to a vortex-pairing problem in Appendix D. It is also useful in treating time-developing plane jet flow.

The problem of interest in this work is the time-developing mixing layer. The main difference between this case and the previous one is that the boundary conditions are no-stress rather than periodic. A variation of the mapping given in Eq. (3.3.5) is suitable for this case, namely,

$$z = h(\zeta) = -a \cotan(2\pi\zeta) , \quad 0 \leq \zeta \leq \frac{1}{2} , \quad -\infty \leq z \leq \infty \quad (3.3.9)$$

As indicated, the domain $0 \leq \zeta \leq 1/2$ is the image of the physical region $-\infty \leq z \leq \infty$ under this mapping. However, the boundary conditions are such that the problem is not periodic in this domain. We shall therefore let ζ range from zero to unity in the computation. The data are made periodic in this domain by defining the solution for

$1/2 \leq \zeta \leq 1$ by reflection about $\zeta = 1/2$. This means that in z -space we are considering two Riemann sheets, i.e., we are essentially doing the problem twice. The difference between this method and the previous one is equivalent to using a Fourier sine or cosine expansion in place of an exponential Fourier transform in a finite domain; in either case, twice the work is required. The choice of sine or cosine transform depends on the nature of the function being expanded. The metric resulting from this mapping is:

$$\frac{1}{h^r} = \frac{1}{2\pi a} \sin^2(2\pi\zeta) = \frac{1}{4\pi a} \left[1 - \frac{(e^{i2(2\pi\zeta)} + e^{-i2(2\pi\zeta)})}{2} \right] \quad (3.3.10)$$

From Eq. (3.3.4), we now have $m = 2$, and the Fourier coefficients of the metric are:

$$\hat{a}_2 = \hat{a}_{-2} = \frac{-1}{8\pi a} ; \quad \hat{a}_{-1} = \hat{a}_1 = 0 ; \quad \hat{a}_0 = \frac{1}{4\pi a} \quad (3.3.11)$$

The truncation error is again small; an estimate for the maximum error in the derivative of f in this case is:

$$\epsilon = 2\pi |\hat{a}_2| \left[|\hat{f}_{N-1}| + |\hat{f}_{N-2}| \right] \quad (3.3.12)$$

Equations (3.3.5) and (3.3.9) are mappings of an infinite physical domain onto a finite domain with grid points clustered near the origin. Equation (3.3.5) is suitable for periodic boundary conditions; Eq. (3.3.9) is suitable for no-stress conditions, and was used in our free shear layer simulations.

3.4 Derivative and Integral Operators

It is important in numerical analysis to use integral and derivative operators that are exact inverses of one another, i.e., that are "consistent." With the results of the last section, we can define a consistent set of derivative and integral operators. Using the mapping (3.3.9) and recalling Eqs. (3.3.2) and (3.3.4), we have

$$\left. \frac{df}{dz} \right|_{z_j} = \left[\frac{1}{4\pi a} \frac{2 - (e^{i2(2\pi\zeta_j)} + e^{-i2(2\pi\zeta_j)})}{2} \right] \left[\frac{1}{N} \sum_{k=-N/2+1}^{N/2-1} \hat{a}_k e^{ik2\pi\zeta_j} \right]$$

Truncating the above expression to include only the wavenumbers k between $-N/2 + 1$ and $N/2 - 1$ gives the definition of the first derivative operator:

$$\left. \frac{\delta f}{\delta z} \right|_{z_j} = \frac{1}{2a} \sum_{k=-N/2+1}^{N/2-1} \left[ik \hat{f}_k - \frac{i(k-2)}{2} \hat{f}_{k-2} - \frac{i(k+2)}{2} \hat{f}_{k+2} \right] e^{i2\pi k \zeta_j} \quad (3.4.1)$$

The prime on the summation indicates that any term whose subscript has magnitude greater than $(N/2 - 1)$ is zero.

The second derivative operator is obtained by a second application of the first derivative operator, giving:

$$\begin{aligned} \left. \frac{\delta^2 f}{\delta z^2} \right|_{z_j} = & \frac{1}{2a} \sum_{k=-N/2+1}^{N/2-1} \left\{ \frac{ik}{2a} \left[ik \hat{f}_k - \frac{i(k-2)}{2} \hat{f}_{k-2} - \frac{i(k+2)}{2} \hat{f}_{k+2} \right] \right. \\ & - \frac{i(k-2)}{4a} \left[i(k-2) \hat{f}_{k-2} - \frac{i(k-4)}{2} \hat{f}_{k-4} - \frac{ik}{2} \hat{f}_k \right] \\ & \left. - \frac{i(k+2)}{4a} \left[i(k+2) \hat{f}_{k+2} - \frac{ik}{2} \hat{f}_k - \frac{i(k+4)}{2} \hat{f}_{k+4} \right] \right\} e^{i2\pi k \zeta_j} \quad (3.4.2) \end{aligned}$$

We also need a fast and accurate Poisson solver for infinite domains. The Poisson equation

$$\nabla^2 P = Q \quad (3.4.3)$$

may be solved by use of the three-dimensional Fourier transform. For the standard case of a function periodic in all three directions and a grid uniformly spaced in each direction, we may find the Fourier coefficient $\hat{P}(\underline{k})$ by dividing the corresponding Fourier coefficient $\hat{Q}(\underline{k})$ by the negative square of the magnitude of the wave vector \underline{k} . One then inverts the Fourier transform to get P itself. This is a very efficient and accurate method of solution. If we use a non-uniform grid in one direction (but uniformly spaced in the other two directions), the solution procedure is only slightly more complicated. For illustrative purposes, we use the mapping (3.3.9) which leads to the second derivative operator given by (3.4.2). Equation (3.4.3) may be solved by considering the linear algebraic system:

$$\hat{A}[\hat{P}] = \hat{Q} \quad (3.4.4)$$

The non-zero elements of A are:

$$\begin{aligned} a_{k,k-4} &= -\frac{(k-2)(k-4)}{16a^2} \\ a_{k,k-2} &= \frac{k(k-2)}{8a^2} + \frac{(k-2)^2}{8a^2} \\ a_{k,k} &= -k_1^2 - k_2^2 - \frac{k^2}{4a^2} - \frac{k(k-2)}{16a^2} - \frac{k(k+2)}{16a^2} \\ a_{k,k+2} &= \frac{k(k+2)}{8a^2} + \frac{(k+2)^2}{8a^2} \\ a_{k,k+4} &= -\frac{(k+2)(k+4)}{16a^2} \end{aligned} \quad (3.4.5)$$

In this case, k_1 and k_2 are the wavenumbers in the uniform grid directions, while k is the ζ -wavenumber in the non-uniform direction. Also, in (3.4.5) any factor whose magnitude is greater than $(N/2 - 1)$ is set to zero. (The problem for uniform grids in all three directions can be viewed as solving (3.4.4) when A is a diagonal matrix.) The solution to pentadiagonal system (3.4.4) can be quickly and easily solved on the computer. Note that, because of the differentiation/integration consistency, this formulation results in a Laplacian identical to the divergence of the gradient operator. This condition is necessary to maintain a divergence-free velocity field, as Kwak et al. (1975) have pointed out.

3.5 Resolution and Statistical Validity

This section will present measures that will help assess the validity of the calculations. We shall use discrete orthogonal function expansions in each spatial direction. This is the most accurate approach available. However, the nonlinear terms in the governing equations make the issue of accuracy difficult to deal with. The product of two variables that can be represented using N modes requires $2N$ modes for complete accuracy. Since we take the product in configuration space, the result is aliased. Aliasing is the pollution of the low wavenumbers

due to high wavenumber information masquerading as low wavenumber information when the grid is too coarse.

To obtain a measure of the accuracy of a configuration space product, we first define the energy spectrum:

$$E(k_1, k_2, z) = \sum_i \frac{1}{N_1 N_2} \hat{u}_i(k_1, k_2, z) \hat{u}_i^*(k_1, k_2, z) \quad (3.5.1)$$

The asterisk denotes the complex conjugate. In (3.5.1) we have Fourier transformed only in the plane of homogeneity, since the grid is non-uniform in z . Consider the central plane ($z = 0$) and note that the highest fully resolved mode in the i^{th} direction is the $N_i/2 - 1$ mode. In the product of u_i with itself, if all non-zero modes have a wavenumber magnitude $|k_i|$ satisfying

$$|k_i| < N_i/4 \quad (3.5.2)$$

then the product is also fully resolved with no aliasing on a grid with N_i points. The fraction of the flow computed with full resolution is therefore

$$\eta_A = \sum_{k_1}'' \sum_{k_2}'' E(k_1, k_2, 0) / \sum_{k_1} \sum_{k_2} E(k_1, k_2, 0) \quad (3.5.3)$$

The double prime on a summation indicates that $|k_i| < N_i/4$. We note further the alias-free fraction of the energy is given by

$$\eta_{AF} = \sum_{k_1}''' \sum_{k_2}''' E(k_1, k_2, 0) / \sum_{k_1} \sum_{k_2} E(k_1, k_2, 0) \quad (3.5.4)$$

The triple prime on the summation indicates the sum over all $|k_i| \leq N_i/4$. One further comment is appropriate, namely, the above are sums over squares in k space.

We now take up the issue of sampling. In a computation of transition in a mixing layer, large, coherent structures are formed. Not all are identical, and thus we desire a measure of how many large structures we capture. We define an energy-weighted measure of the sample size:

$$\eta_s = \frac{\sum_{k_1} \sum_{k_2} \max(|k_1|, 1) \max(|k_2|, 1) E(k_1, k_2, 0)}{\sum_{k_1} \sum_{k_2} E(k_1, k_2, 0)} \quad (3.5.5)$$

The sample size η_s tells us how many effective full Fourier waves the total energy has in the computational domain. It is essentially the ratio of the area of the computational domain to the product of length scales in two coordinate directions; the definition of the length scales is implicit in Eq. (3.5.5).

For a given number of grid points, one may choose a fine mesh so that η_A and η_{AF} are very near one, but the sample η_s , will be small. Conversely, with a coarse grid η_s is large, but we sacrifice accuracy. In other words, we may compute the behavior of one large eddy accurately, or compute several large eddies crudely. The choice depends on one's objectives. Values for η_A , η_{AF} , and η_s are presented with the computational results in Chapter 5.

3.6 Interpolation

To gain further insight into the physical nature of transition in the mixing layer, we shall track particles using computer graphics. After computing the flow field, we know the velocity field at the grid points, and we must interpolate to find the velocity at the location of each particle. For maximum accuracy and consistency, we should use Fourier interpolation. However, the cost of Fourier interpolation is excessive for this purpose. We chose to use a three-point interpolation scheme (three points in each direction, or a 27-point box). In the uniform grid directions, the function is represented as

$$f(x) = c_0 + c_1 x + c_2 x^2, \quad -\frac{1}{2} \leq x \leq \frac{1}{2} \quad (3.6.1)$$

The origin is always taken to be the nearest grid point (which we call x_i) and the distance between grid points is taken to be unity. At the nearest grid point the value of the function is f_i and we have

$$\begin{aligned} c_0 &= f_i \\ c_1 &= (f_{i+1} - f_{i-1})/2 \\ c_2 &= (f_{i-1} - 2f_i + f_{i+1})/2 \end{aligned} \quad (3.6.2)$$

The interpolation in the z direction (non-uniform grid) is similar, but more complicated. It is based on a Taylor expansion, and the first and second derivatives are evaluated using the formulas given in Appendices A.1 and A.3. Also, rather than using the nearest grid point as the origin in the z direction, we use the grid point for which $h'(z_i)|z - z_i|$ is smallest. If z_p is the nearest grid point above z and z_m the nearest grid point below z , then $z_i = z_p$ if $(z_p - z) \times h'(z_p) < (z - z_m) \times h'(z_m)$, or $z_i = z_m$ if $(z - z_m) \times h'(z_m) < (z_p - z) \times h'(z_p)$. Note that h' is the inverse of the mapping metric given by Eq. (3.3.10).

3.7 Generating a Smooth, Divergence-Free Initial Disturbance Field

Kwak et al. (1975) developed a scheme for producing a divergence-free flow field with any desired three-dimensional energy spectrum. This scheme uses random numbers to select the phases of the Fourier coefficients of the velocity field on a $(16)^3$ uniform cubic grid. The Fourier coefficient vector is in the plane whose normal is the wavevector, but with random phase. The orthogonality of the Fourier coefficient and the wavevector ensures that the field is divergence-free.

We used Kwak's routine with three different sets of random numbers (designated 1,2,3), and two different spectrum shapes were used. In all but Case 11,* we used the homogeneous isotropic turbulence spectrum of Comte-Bellot and Corrsin (1971) and applied the Gaussian filter (2.5.4) to give a spectrum we could adequately resolve. For Case 11 we used a "white noise" energy spectrum (all modes excited at equal energy) as input to Kwak's routine. We then zeroed the Fourier coefficients of all modes with $|k_1| > 4$ or $|k_2| > 4$. Thus we retained only 24 of the longest wavelength modes (in horizontal planes) in our initial disturbance field in Case 11.

Kwak's scheme generates $(16)^3$ disturbance fields on a uniform cubic grid. From these fields we extract five planes of data and deposit them on the five central planes of the non-uniform anisotropic grid used in

*See Chapter 5.

the mixing layer computations. On the new grid, the disturbance field is discontinuous and no longer divergence-free. We first eliminated the discontinuity by applying a Gaussian convolution filter, as given by Eqs. (2.5.3) and (2.5.4) in the x_3 direction (across the mixing layer). Note that this smoothing is applied to the initial conditions and therefore there are no difficulties of the kind discussed in Section 2.5. The filter width used was $\Delta_3 = \sqrt{48} h_3$, where h_3 is the computational grid spacing ($\Delta\zeta$). Thus the filter is non-uniform in physical space. We then multiplied each velocity component u_i by a weight factor a_i such that the final field has approximately equal rms amplitudes for all three components.

Finally, we obtained the divergence-free initial disturbance field \tilde{u}_i by two different procedures. The first, used for all but Case 11, was to take the curl of smoothed and weighted field. In Case 11 we again took the curl, but called this the disturbance vorticity and solved the Poisson equation for the vector potential whose curl is then the divergence-free velocity field which is then used in the calculation.

Chapter 4

METHOD VALIDATION

4.1 Convection

In this section we shall assess the new Fourier method described in the last chapter by applying it to a one-dimensional convection problem. We shall compare it to the finite-difference methods given in Appendices A.1 and A.2. The solutions are all computed on grids of 33 points and compared with the analytical solution.

The grid used is defined by Eq. (3.3.9) with

$$a = 32/\pi \quad \text{and} \quad \zeta_j = (j-1)/64$$

The one-dimensional convection equation to be used as a test is:

$$\frac{\partial u}{\partial t} + c \frac{\partial u}{\partial z} = 0 \quad (4.1.1)$$

and has the exact solution

$$u(z,t) = f(z-ct) \quad (4.1.2)$$

which just says that any initial waveform propagates toward increasing z with a uniform speed c . We used a Gaussian waveform initial condition, for which the exact solution to Eq. (4.1.1) is:

$$u(z,t) = \exp\{-[1.6651(z-ct)/\delta_{1/2}]^2\} \quad (4.1.3)$$

In the problem we solved, we took $\delta_{1/2} = 4$ and $c = -1$. The half-width $\delta_{1/2}$ is the width of the waveform at half its peak value.

We used the mapping (3.3.9) which is appropriate for functions which vanish at \pm infinity. Although the appropriate Fourier method for this problem is the complex exponential transform, we used an equal combination of sine and cosine transforms.

Another way of looking at this is to use the Riemann sheet perspective of Section 3.3. A cosine expansion implies a waveform imaged symmetrically about infinity onto a second Riemann sheet. Similarly, using a sine expansion implies an antisymmetric reflection of the physical waveform onto the second Riemann sheet. The physical and image waveforms will propagate towards one another with equal speed and meet at infinity at infinite time. If we use the combination

$$\frac{\delta u}{\delta z} = \frac{1}{2} \left[\frac{\delta u}{\delta z} \Big|_{\sin} + \frac{\delta u}{\delta z} \Big|_{\cos} \right]$$

no image waveform appears on adjacent Riemann sheets, and we obtain periodicity of the waveform over two Riemann sheets. All waveforms are identical and propagate with equal speed in the same direction.

The time advance method was the well-known fourth-order Runge-Kutta scheme with very small time step. The Courant number was taken to be:

$$\frac{\Delta t |c|}{\Delta z_{\min}} = .01$$

The time step was chosen small so that the error is dominated by that of the spatial-differencing scheme.

The scheme given by Eq. (A.1)* is second-order in physical space and slightly more accurate than Eq. (A.2), which is second-order in computational space but first-order in physical space. (In the limit $\Delta_j \rightarrow \Delta_{j-1}$, Eq. (A.2) is also second-order in physical space.)

Figure 4.1.1 shows the grid points relative to the initial waveform and also shows the computed solutions at $T = ct/\delta_{1/2} = 2.0$ obtained using Eq. (A.1) (denoted F.D.) and the new Fourier scheme (denoted N.F.). The maximum error in the solution of the one-dimensional wave equation is .34 using Eq. (A.1), .40 using Eq. (A.2), and .0032 for the new Fourier scheme. Therefore, we conclude that the new Fourier method is vastly superior to finite-difference calculation in its handling of convection.

* See Appendix A, Eq. (A.1).

4.2 Diffusion

We shall now assess the new method on a diffusing problem. Using the same grid as for the convection problem, we solved the heat equation

$$\frac{\partial u}{\partial t} = v \frac{\partial^2 u}{\partial z^2} \quad (4.2.1)$$

The fourth-order Runge-Kutta scheme was used for the time advance (the time was small enough that spatial differencing errors dominated). The dimensionless time step was

$$\frac{v\Delta t}{\Delta z_{\min}^2} = .05625$$

We used two finite-difference schemes for the second spatial derivative. The first scheme is two consecutive applications of (A.1); the second finite-difference scheme is given by (A.3). The (A.3) scheme is a three-point scheme and is first-order; it becomes second-order as

$$\Delta_{j-1} \rightarrow \Delta_j.$$

The initial condition used was an error function, giving the analytical solution:

$$u(z,t) = \text{erf} \left[z/\sqrt{4vt} \right]$$

We set $t_0 = 25$ and $v = .06$, and we advanced the computation until $t_f = 16t_0$.

Figure 4.2.1 shows the time history of the maximum normalized error defined by

$$E_m = \frac{(u_c - u_A)_{\max}}{(u_o - u_A)_{\max}}$$

as a function of dimensionless time. E_m is the maximum error in the computed solution normalized by the maximum change from the initial condition. We see that the new Fourier scheme has errors six orders of magnitude smaller than the finite-difference method at early times and three orders of magnitude smaller at later times. Thus the new Fourier method is far superior in its treatment of diffusion.

4.3 Taylor-Green Problem (2-D)

The previous two tests were both on one-dimensional problems and pertained to the infinite domain Fourier method. In order to test the Navier-Stokes aspects of the final program, we checked the accuracy of the code by computing the solution of the 2-D Taylor-Green problem and comparing it with the analytical solution. The 2-D Taylor-Green problem is a stable configuration of counter-rotating vortices whose amplitude decays by viscous effects. The initial condition for this problem is

$$\begin{aligned}u(x,y,z,0) &= \cos(k_1 x) \sin(k_2 y) \\v(x,y,z,0) &= -(k_1/k_2) \sin(k_1 x) \cos(k_2 y) \\w(x,y,z,0) &= 0\end{aligned}\tag{4.3.1}$$

The analytical solution to this problem is

$$\begin{aligned}u(x,y,z,t) &= u(x,y,z,0) e^{-(k_1^2+k_2^2)\nu t} \\v(x,y,z,t) &= v(x,y,z,0) e^{-(k_1^2+k_2^2)\nu t} \\w(x,y,z,t) &= 0\end{aligned}$$

In our calculation we used $\nu = 1.36$, $k_1 = k_2 = \pi/39.6$, and $\Delta t = 6.26$, which gives

$$e^{-(k_1^2+k_2^2)\nu\Delta t} = .8983775$$

The fourth-order Runge-Kutta method gives the first five terms of a Taylor expansion of the exponential, giving an error of .0000011 by analysis. Exactly the same error was found in the computation.

Since the error in the computation matches the analytical error estimate, we conclude the code is functioning properly in two dimensions. This test showed that the pressure, convection, and diffusion are properly advanced in time, at least for two-dimensional flows.

Chapter 5

RESULTS

5.1 Overview of Effects Studied

The primary focus of this study concerns the sensitivity of the mixing layer to initial conditions. We shall examine the growth of the momentum thickness, mean velocity profile, kinetic energy, Reynolds stresses, anisotropy of the Reynolds stresses, shear stress correlation in the center of the layer, and particle track pictures. These data will allow us to assess the mixing layer's sensitivity to the amplitude, spectrum shape, and relative phases of the initial disturbance field. We shall also examine the influence of the subgrid scale model on the computed large-scale field, as well as the influence of filtering. It must be remembered that, due to computational limitations, all computations cover only the developing near field of the mixing layer.

5.2 Case Descriptions

Nine cases of mixing layer transition were studied in detail. In Sections 2.3 and 3.7 we discussed the way in which the initial conditions were constructed. In this section we shall give a detailed case-by-case description. Thus the various cases will be freshly in mind later in the chapter, allowing a better understanding of the results.

The initial conditions of the various cases are defined by their disturbance fields, as the initial mean field is the error function in all cases. Each initial disturbance field is characterized by the energy spectrum and random number set used by Kwak's routine, the method by which it is adapted to the nonuniform grid, and the amplitude. The description for each case is given in Table 5.1. The terms are defined in Table 5.2.

In addition to the effect of initial conditions, we also checked the sensitivity of our results to the subgrid scale model described in Section 2.6 and the influence of the filtering the governing equations. The subgrid scale model is given by Eq. (2.6.1) with the eddy viscosity given by (2.6.2). Whether the model and/or filtering were used is indicated in the last two columns of Table 5.1. Case 9 was an attempt

to resolve the full field without filtering, but the resolution measures described in Section 3.5 suggest that, by dimensionless time $T = 130$ or $\theta/\theta_0 = 2.4$, the resolution is marginal. The initial condition of Cases 5, 9, and 10 are identical. Comparing Case 5 with Case 10 shows the model influence, while Cases 9 and 10 assess the influence of filtering.

Table 5.1
Descriptions of Cases Run

Case No.	Input E(k)	Amplitude	Random No. Set	Initial Field Type	Model	Filtering
2	C-B-C.	High	1	1	Yes	Yes
4	"	Low	1	1	"	"
5	"	Medium	1	1	"	"
6	"	Low	2	1	"	"
7	"	Medium	2	1	"	"
8	"	High	2	1	"	"
9	"	Medium	1	1	No	No
10	"	Medium	1	1	"	Yes
11	Box	Medium	3	2	"	"

Table 5.2
Definitions of Terms Used in Table 5.1

Quantity	Descriptor	Significance
E(k)	C-B-C	Comte-Bellot & Corrsin spectrum.
	Box	White Noise spectrum.
Amplitude	Low	$(q^2/2)_{\max} = 3.2 \times 10^{-6}$.
	Medium	$(q^2/2)_{\max} = 3.2 \times 10^{-4}$.
	High	$(q^2/2)_{\max} = 3.2 \times 10^{-2}$.
Random No. Set	1,2,3	Seed for random number generator.
Initial Field Type	1	Curl used as initial velocity.
	2	Curl used as initial vorticity.
Model	Yes, No	Subgrid scale model used?
Filtering	Yes, No	Filtering used during simulation?

Before discussing the results, we shall comment on the length of the various runs. Initially, all runs were given enough computational time to ensure at least a fourfold thickening of the layer. Since the time step was varied continuously in all cases, the final times of the runs differed significantly. Following this initial set of runs, three cases (5,6,7) were run until the layer was at least eight times its initial thickness. We thereby explored several effects, using a few runs to the limit of our grid without excessive computer cost. (Each of the various cases required from 1.5 to 5 hours of CDC 7600 computer time.)

5.3 Mean Velocity Profiles

The mean velocity normalized by the velocity difference across the layer was plotted at various dimensionless times $T = \Delta U t / \theta_0$ against the scaling variable $Z = z / \theta$, where θ is the momentum thickness

$$\theta = \int_{-\infty}^{\infty} \left[1/4 - \left(\frac{\langle u \rangle}{\Delta U} \right)^2 \right] dz \quad (5.3.1)$$

where $\langle \rangle$ denotes a planar average. As nearly all of the profiles were found to be self-similar throughout the simulations, we show only one case here, Case 6, the case that departs most significantly from self-similarity.

Figure 5.3.1 presents the mean velocity profile in terms of the non-dimensional variables defined above for Case 6, a low-amplitude initial field case which was run for a long time. It is clear that the mean velocity profile remains self-similar for a long time--a non-dimensional time of the order of 400. At the last time shown ($T = 554$), self-similarity breaks down, and this is a clear indication that the numerical simulation is no longer faithful to the physics of the flow. The calculation clearly has to be stopped at this point. Note that the layer was more than ten times its initial thickness at this time.

5.4 Momentum Thickness

In this section we shall discuss the growth of the momentum thickness. Before looking at the numerical simulations, we shall discuss some experimental results. To compare the experimental spatial growth rate, $d\theta/dx$, with the growth rate of the time-developing layer, $(d\theta/dt)/\Delta U$, we introduce the parameter

$$\lambda = \frac{U_1 - U_2}{U_1 + U_2} \quad (5.4.1)$$

where U_1 is the high speed and U_2 is the low speed in the experiment. By Taylor's hypothesis, the time rate of growth of the momentum thickness in the time-developing mixing layer is related to the spatial growth rate by:

$$\frac{d\theta/dt}{\Delta U} = \frac{1}{2\lambda} \frac{d\theta}{dx} \quad (5.4.2)$$

The experimental $d\theta/dx$ are converted using (5.4.2) to allow comparison with the computational results. For a mixing layer to be self-similar, θ must grow linearly in time or space, but the shear layer need not be self-similar except in the developed, far-downstream state. Whether there is a unique state for all shear layers is not known.

Mansour et al. (1978) in Table 1.1 gave a list of the growth rates for several different experiments. The experimental data for the momentum thickness were fit with straight lines to give values of the growth rate; the resulting values of $(d\theta/dt)/\Delta U$ vary between 0.015 and 0.022. We cannot expect a precise comparison with the experimental data, due to differences between a time and spatially developing layers, as discussed in Section 2.2. The differences are likely to be greater in the early or near field. In the spatially developing case, there is a feedback due to the pressure that is absent in the time-developing case. The measurements of Winant and Browand (1974) gave $(d\theta/dt)/\Delta U \approx 0.035$ in the near field, while farther downstream $(d\theta/dt)/\Delta U \approx 0.019$ for the experiment with laminar boundary layers at the edge of the splitter plate.

Figures 5.4.1 through 5.4.3 show θ/θ_0 versus $T = t\Delta U/\theta_0$ for the various cases. We shall now discuss the effects of initial conditions, the subgrid scale model, and filtering on the development of the momentum thickness.

A. Initial Conditions

First we shall examine the effect of the different random phases of the initial disturbance fields. The different phases were obtained by starting the random number generator with a different "seed." The small initial disturbance cases (4,6) differ only in their initial random phases. Figure 5.4.1 shows that the time required to attain a significant growth rate can vary, but Fig. 5.4.4 shows that, once a significant growth rate is attained, the initial random phases have little effect. A similar behavior is observed in Cases 5 and 7, whose initial disturbance fields are 10^2 times as energetic as Cases 4 and 6, respectively, but are otherwise identical. We again see in Fig. 5.4.2 that the case (7) with seed #2 grows sooner than the case (5) with seed #1. This suggests that the random phases produced by seed #2 are more closely aligned with the phase distributions of the most amplified eigenfunctions. Moving to Figs. 5.4.3 and 5.4.6, we again increase the initial disturbance energy by 10^2 . In these two high-amplitude initial disturbance cases (2 and 8), the initial phases have a very minor role with seed #2, once again showing a higher early growth.

In conclusion, we note that the initial random phases affect early growth of the momentum thickness, with diminishing influence on later growth. We also note that the influence is greatly diminished for high initial disturbance amplitudes.

We now examine the effect of the spectrum shape of the initial condition on the growth of the momentum thickness. Cases 10 and 11 differ in the spectrum of the initial field with the energy content of Case 11 concentrated in the amplified and most slowly decaying modes relative to Case 10. (Note that both Cases 10 and 11 are run without a subgrid model.)

As Figs. 5.4.2 and 5.4.5 show, the initial concentration of energy in the most amplified modes results in a significantly higher momentum

thickness growth rate. Though the present computations do not establish the duration of this higher growth rate, it is fair to say that a significantly higher growth rate due to concentrating the initial disturbance energy in the most amplified modes will persist for at least a sixfold thickening of the layer for the case of a medium amplitude initial disturbance.

Turning our attention to the effect of the initial disturbance amplitude, we now examine Figs. 5.4.7 and 5.4.8. Cases 4, 5, and 2 (Fig. 5.4.7) all have the same initial spectrum shape and random phases, but differing initial disturbance amplitudes. We note that the small and medium amplitude Cases 4 and 5 display nearly the same behavior as each other; the low-amplitude case is slightly delayed in its growth. The high initial disturbance amplitude (Case 2) shows a differing trend. It first reaches a growth rate two to three times as large as the asymptotic value of the spatially developing mixing layer, and then plummets to the observed range of the asymptotic spatially developing layer. The behavior of Cases 6, 7, and 8 is similar to the behavior observed in Cases 4, 5, and 2, respectively.

We conclude that, at low initial amplitude, different initial amplitudes lead to the same momentum thickness growth rate; at high initial amplitudes, the growth rate may dramatically overshoot its final value.

B. Subgrid Scale Modeling

The effect of a subgrid model is seen by comparing Cases 5 and 10. In Fig. 5.4.2, one sees that the model slows the growth of the momentum thickness only very slightly. Figure 5.4.5 emphasizes that the effect is indeed slight, even at later times. Thus the effect of the subgrid scale model is not very important in simulation of these flows; more evidence will be given later. We shall also see later that the differences that do exist are in the small scales, as expected.

It appears that the model has little influence on the growth of the momentum thickness. However, the observation may be due to cancellation of two effects; the model destroys the small scales, making the flow less energetic, but it also increases the diffusion of momentum.

C. Filtering

Next, we look at the effect of filtering by comparing Cases 10 and 9. For Case 9, which has no filtering, the growth rate of its momentum thickness is quite erratic after $T = 130$ or $\theta/\theta_0 = 2.5$. As we shall see later, this case is behaving unphysically after this point.

Thus filtering the field is very effective in keeping energy from piling up at the high wavenumbers. Indeed, filtering is more important than the subgrid scale model in this respect.

5.5 Turbulent Kinetic Energy at the Center of the Mixing Layer

To examine the energy of the disturbance field, we have plotted the turbulent kinetic energy, $\frac{1}{2} \langle \tilde{u}_i \tilde{u}_i \rangle$, ($\tilde{u}_i = \bar{u}_i - \langle \bar{u}_i \rangle$) at the center of the mixing layer, normalized by the square of the velocity difference across the layer $(\Delta U)^2$, against both dimensionless time T and dimensionless momentum thickness. These curves display some important features that we shall now discuss.

An interesting effect is a tendency for the (normalized) energy to overshoot the value expected based on the experiments. Fig. 5.5.1 shows the time history of the normalized kinetic energy at the center of the mixing layer, for Cases 4 and 6, the small-amplitude initial disturbance cases. While the overall behavior of the two cases is similar, they begin to diverge somewhat around $T = 50$, but later rejoin. By $T = 300$, both are very near 0.037, the far-downstream value of the normalized kinetic energy reported by Wygnanski and Fiedler (1970). However, both cases exhibit overshoot; Case 6 reaches a peak about 60% higher than the final experimental value.

Although the calculations cannot be carried sufficiently far to reach the asymptotic state of the mixing layer, we believe this overshoot is real, because it has also been seen in experiments. Bradshaw (1966) reported an experiment with a shear layer generated from a laminar boundary layer. In his results, the gradient component of the disturbance field $\langle \tilde{w}^2 \rangle$ overshoots its far-downstream value by 100% (rms) and the streamwise component overshoots by 15%. His results are shown in Figs. 5.5.2 and 5.5.3. Thus the overshoot we find is consistent with the experimental data.

The computed results appear to have a longer overshoot time scale than the experiment; this may be due to the difference between the time- and space-developing layers, or it may be a Reynolds number effect. Although not shown, the kinetic energy of Case 6 begins to decline at $T = 450$ and continues to descend toward the far-downstream value until the computation is stopped at $T = 554$. However, the resolution is marginal from $T = 450$ on. In Fig. 5.5.4, the normalized kinetic energy of Cases 4 and 6 is plotted versus the dimensionless momentum thickness $\Theta = \theta/\theta_0$. In these coordinates the two cases are remarkably similar, and this indicates that the increase in kinetic energy is more related to the thickness of the mixing layer than to the time. Hence, we shall plot $(q^2/2)/(\Delta U)^2$ vs. θ/θ_0 in the remainder of this section.

Let us now look at the overshoot in the medium amplitude cases. Figure 5.5.5 shows the normalized turbulent kinetic energy as a function of dimensionless momentum thickness for the medium-amplitude disturbance cases. The initial disturbance kinetic energy is slightly more than two orders of magnitude smaller than the far-downstream turbulent kinetic energy. In the two cases (5 and 7) run furthest in time, we see an overshoot followed by a gradual decline. The overshoots are approximately the same size as in the low initial disturbance cases. Case 9 differs most from the rest of this group. This is the case with no filtering or subgrid model. After reaching a peak amplitude roughly 45% higher than the far-downstream experimental value, the kinetic energy begins to decline. Unfortunately the numerical resolution of this case is questionable after $T = 130$ ($\Theta = 2.4$).

A striking observation is that the overshoot behavior at high initial amplitudes differs from that expected from experiments. The two high-amplitude cases (2 and 8) are shown in Fig. 5.5.6; these cases might represent the mixing layer produced from turbulent boundary layers. In these cases the initial energy is roughly 10% lower than the far-downstream experimental value. Both of these cases show a quick rise of the kinetic energy to roughly 60% more than the far-downstream value of the laboratory layer; at the time of the peak in the energy, the mixing layer has thickened by a factor of 2.5. Following this, the turbulent kinetic energy for Case 2 decreases, but it is still about 35% above the fully developed turbulent mixing layer laboratory value at the

end of the run. Case 8 shows no sign of a decline in the turbulent kinetic energy at the time the run was stopped.

The most significant aspect of these two high-amplitude runs is that the energy and growth rates significantly overshoot the expected fully developed values. However, the experimental mixing layer does not exhibit this behavior when the splitter-plate boundary layers are turbulent. The most probable reason for this discrepancy is that the boundary layer turbulence has a longer characteristic streamwise wavelength and much higher obliqueness (Kim, 1981) than the mixing layer can amplify or sustain, while the initial disturbance used in the simulation contains more of the highly amplified wavelength components. We must also consider the possibility that the time-developing mixing layer is more energetic than the spatially developing layer.

The effect of the subgrid model on the centerline kinetic energy is seen by comparing Cases 5 and 10, which are identical in all aspects, except that no model is used in Case 10 in Fig. 5.5.5. The model results in roughly a 10% reduction in the energy, which is smaller than the effect produced by varying the initial conditions (compare Cases 5 and 10 with Cases 7 and 11).

5.6 Profiles of the Turbulent Kinetic Energy

In the previous section the turbulent energy at the center of the layer was presented. That information is sufficient to gain an overall perspective of the turbulence intensity. In this section, we shall check for similarity in the turbulent energy profile.

In Fig. 5.6.1, the turbulent kinetic energy, normalized by the value at the center of the layer, is plotted versus distance across the layer normalized by the momentum thicknesses for Case 4, a low initial amplitude case. Case 6 is quite similar and is not shown. In the time interval covered in the figure, initial momentum thicknesses grew by between 3.5 to 4.0.

In the small disturbance cases, the initial profile was much too broad. At $T = 83$ we find a narrow profile characteristic of the eigenfunctions of the linearized equations. The profile then begins to

broaden until, at $T = 246$, the energy profile is somewhat broader than the "fully developed turbulence" case of Spencer and Jones (1971). At the latest time, the profile is close to that of Spencer and Jones. To see whether this profile persists, we ran Case 6 out much further in time. The profiles remain close to the experimental one; at the final time the layer is more than ten times as thick as it was initially and the numerical accuracy is deteriorating, due to the coarseness of the grid at the outer edges of the shear layer.

In Fig. 5.6.2, the normalized turbulent energy profile is given for a typical medium-amplitude case, Case 11; the others are similar. We again note that the initial condition profile was much too broad. At approximately $T = 66$, these cases exhibit the "narrow" profile characteristic of the eigenfunctions of the linearized equations. At later times all cases show profiles characteristic of fully developed turbulence without the oscillatory behavior of the profile width found in the small-amplitude cases.

In Fig. 5.6.3, we give the kinetic energy profiles of a high initial-amplitude case (Case 2); Case 8 is quite similar. In these cases the profile exhibits a self-similar shape by $T = 32.8$. While the shape reaches self-similarity very quickly, we must remember that the maximum intensity overshoots the final value due to the long wave character of the initial condition.

In summary, we note that the profile of the turbulent kinetic energy profile always progresses from the broad initial profile to the self-similar experimental profile. The approach is oscillatory when the initial energy is low and monotonic if the initial energy is high.

5.7 Reynolds Stresses

In the previous sections, we have learned something of the behavior of the mean velocity profile, the momentum thickness, and the turbulent kinetic energy. With this in mind, we shall now look at profiles of the Reynolds stress tensor. The discussion will proceed from the small-amplitude to large-amplitude initial disturbances with the effects of modeling and filtering included in the medium-amplitude initial disturbance cases.

In Figs. 5.7.1 through 5.7.7, the profiles of the Reynolds stresses for a small-amplitude case (6) are presented. Because the absolute values of the quantities increase rapidly, the results are presented as $\langle \tilde{u}_i \tilde{u}_j \rangle / q^2 (z=0)$ vs. z/θ . The first figure shows the initial conditions. The maximum value of each normal stress is nearly the same. The double peaks in the normal stresses $\langle \tilde{u}^2 \rangle$ and $\langle \tilde{v}^2 \rangle$ are due to the way the initial condition are constructed.*

At $T = 83$ (Fig. 5.7.2), the stresses are those characteristic of the eigenfunctions of the linearized equations. By $T = 165$, nonlinear effects are becoming important and the dominance of $\langle \tilde{u}^2 \rangle$ is diminishing; see Fig. 5.7.3. At $T = 246$ (cf. Figs. 5.7.4), we see that the gradient component of the normal stress, $\langle \tilde{w}^2 \rangle$, has become strongly dominant.

A physical explanation of this can be offered with the aid of the visualizations that are presented in Section 5.11. At $T = 246$, the shear layer has rolled up into vortical structures. If these were straight two-dimensional vortices, as Brown and Roshko (1972) suggested they might be, $\langle \tilde{u}^2 \rangle$ would be double peaked, $\langle \tilde{w}^2 \rangle$ would be single peaked and larger than $\langle \tilde{u}^2 \rangle$ in the center, and $\langle \tilde{v}^2 \rangle$ would be zero. This picture explains much of what is seen in Fig. 5.7.4. The differences are due to the vortices not being straight, which introduces streamwise vorticity, causing $\langle \tilde{v}^2 \rangle$ to be non-zero, and reduces $\langle \tilde{u}^2 \rangle$. Bradshaw (1966) found the same effect in the laboratory. In fact, his data show a stronger effect; in some cases the gradient stress was three times the streamwise stress.

At $T = 328$, Fig. 5.7.5 shows the onset of significant asymmetry. This is not surprising as there are only two or three large eddies in the computational domain. The strong dominance of the gradient component of the normal stress is greatly diminished at $T = 328$. Figures 5.7.6-7 show later profiles for Case 6. Although the streamwise component becomes the dominant normal stress at $T = 554$, the results are marginal at this time due to insufficient resolution at the edges of the

*The initial field is defined by $\vec{v}_0 = \vec{\nabla} \times \vec{v}'_0$, \vec{v}'_0 varies rapidly with z near the edges of the layer.

shear layer. The double peak of the streamwise component is probably due to the existence of a strong vortex with some curvature in the plane of homogeneity (see Section 5.11).

Finally, we note that $\langle \tilde{w}^2 \rangle$ is dominant at the outer edges of the layer at late times but not in the initial condition. This is consistent with experimental observations and, as Phillips (1954) has shown analytically, $\langle \tilde{w}^2 \rangle = \langle \tilde{u}^2 \rangle + \langle \tilde{v}^2 \rangle$ in the irrotational portions of the flow. This remark applies to other cases as well. The other small-amplitude case (4) is similar to Case 6, but most of the effects observed above are weaker.

Let us now turn our attention to the medium-amplitude cases (5, 7, 9, 10, 11). The initial conditions are shown in Fig. 5.7.8-10. It is apparent that the method used to generate Case 11 results in much smoother stress profiles and probably should be preferred.

Figures 5.7.11-14 show four of the profiles at $T \approx 66$. At this time the profiles have the characteristic shape corresponding to the eigenfunctions of the linearized equations. All cases are now very similar, in contrast to the initial conditions. The symmetry is apparent, as is the dominance of the streamwise normal stress. Cases 5 and 10 (not shown) are nearly indistinguishable, showing that the subgrid model has little influence on the stresses; this accords with what we found earlier about the need for the model. The "full simulation" (Case 9) yields rounder profiles for $\langle \tilde{v}^2 \rangle$ and $\langle \tilde{w}^2 \rangle$ than the filtered calculations.

In Figs. 5.7.15-18, we see immense differences between cases developing as we move into the strongly nonlinear domain at $T \approx 131$. Cases 5 and 10 (not shown), which differ only by the absence of a subgrid model in Case 10, again display very little difference. However, comparing Cases 5 and 10 with Case 9, we note a large influence of filtering. At $T = 130$, Cases 5 and 10 are only roughly half as energetic as Case 9 at $T \approx 130$. At $T \approx 180-190$, Cases 5 and 10 are as energetic as Case 9 at $T \approx 130$. If Fig. 5.7.17 is compared with 5.7.19, it is found that they are quite similar. This suggests that the influence of filtering is to delay the time required to reach the

strongly nonlinear domain. Case 9 is generally closer to the physics of the laboratory flow, as might be expected.

The difference between Cases 5 and 7 at $T \approx 131$ is amazing, since the two cases differ only by the set of random numbers used to generate the initial conditions. Figs. 5.7.19-22, give the stress profiles at $T \approx 197$. Cases 5 and 10 are again nearly identical. Cases 5 and 7 are much more similar than at the previous time but, as we shall see below, this is probably coincidental. Case 9 is significantly different from Cases 5 and 10, but Case 9 has marginal resolution at $T = 197$, so caution is needed. The breakdown of the resolution is hinted at by the jaggedness of the curve; better evidence of breakdown will be given later, cf. Sections 10 and 11. Case 11 is now quite different from the others. Once again, this demonstrates the ability of nonlinear processes to cause a large divergence of solutions which were close to one another (compare Cases 10 and 11 at $T \approx 131$ with the same cases at $T \approx 197$). Figure 5.7.23 shows that Case 5 has nearly reached the asymptotic state at $T = 295$; no further significant changes were observed at later times. On the other hand, Figs. 5.7.24-25 show that Case 7 takes a long time to reach the far-downstream state. In Section 5.8 we shall present stronger evidence of this.

Next, we shall compare the medium initial amplitude cases with the corresponding low initial amplitude cases; Cases 4 and 5 and Cases 6 and 7 have the same initial fields except for the magnitude of the disturbance field. Comparing the latter pair of cases, we find very similar behavior, but the medium initial case (7) develops on a faster time scale than the low initial amplitude case (6). The same is true of Cases 4 and 5.

Let us now turn to the high initial amplitude cases (2 and 8). The initial profiles are the same as those for Cases 4 and 6, respectively. At $T \approx 33$, Figs. 5.7.26-27 show that in Case 2 the streamwise normal stress is more dominant than in Case 8. Both of these cases show stronger dominance of the streamwise component than that observed experimentally with turbulent boundary layer(s) on the splitter plate; they also differ from the experiment in other respects, as we have seen earlier and shall see again. Figures 5.7.28-30 show stress profiles of

roughly the experimentally observed relative magnitudes, indicating that these cases develop more quickly than the low amplitude ones. Figure 5.7.29 shows that the gradient normal stress becomes dominant for Case 8 at $T = 66$; this is not observed in experiments having turbulent boundary layers. Fig. 5.7.30 shows that Case 2 has considerable asymmetry in the spanwise normal stress; this reflects the small sample size. All of the differences between our computations and experimental results for the high initial amplitude cases (except the asymmetry) show the computed results to be in the direction of the experimental results for laminar boundary layers.

We thus conclude once again that the experimentally observed near-field differences between mixing layers generated from laminar and turbulent splitter plate boundary layers are due more to the characteristic wavelengths of boundary layer turbulence than they are to the disturbance amplitude. Additional conclusions about the Reynolds stress evolution will be drawn at the end of the next section.

5.8 The Reynolds Stress Anisotropy Tensor

In this section we shall discuss the Reynolds stress anisotropy tensor. We define $\langle \tilde{u}_i \tilde{u}_j \rangle$ as the average of $\tilde{u}_i \tilde{u}_j$ over a horizontal plane. If there were enough points in each horizontal plane, $\langle \tilde{u}_i \tilde{u}_j \rangle$ would be equivalent to the ensemble average of $\tilde{u}_i \tilde{u}_j$, i.e., the Reynolds stress tensor. However, as there are only 256 points in each horizontal plane and the velocities are not statistically independent, this identification needs to be made cautiously. The anisotropic component of this "Reynolds stress" is:

$$b_{ij} = \frac{\langle \tilde{u}_i \tilde{u}_j \rangle}{\langle \tilde{u}_k \tilde{u}_k \rangle} - \frac{1}{3} \delta_{ij} \quad (5.8.1)$$

In the time developing mixing layer, b_{ij} is a function of z and t . As the Reynolds stresses are functions of z and there are asymmetries, we shall consider an energy-weighted average of the anisotropy tensor (5.8.1) to characterize the turbulence

$$B_{ij} = \int_{-\infty}^{\infty} \langle \tilde{u}_\ell \tilde{u}_\ell \rangle_{ij} dz \int_{-\infty}^{\infty} \langle \tilde{u}_\ell \tilde{u}_\ell \rangle dz \quad (5.8.2)$$

This will limit the number of figures required to present the results and carries most of the important information.

We shall begin examining the energy-weighted anisotropy tensor by looking at the small-amplitude cases. Next, the medium-amplitude cases will be considered, and here the effects of modeling and filtering are examined, as well as initial condition influence. Finally, the high initial disturbance amplitude cases are considered. In Figs. 5.8.1 through 5.8.9 the B_{ij} for the nine cases studied are plotted versus time.

The B_{ij} for the small-amplitude cases (4 and 6) shown in Figs. 5.8.1-2 are similar, but not identical. The streamwise normal stress dominates at early times, while the gradient component dominates at intermediate times. The shear (B_{13}) and span (B_{22}) ts have similar character, and both are primarily negative. For the shear component, this is as expected. The span component is the smallest of the normal stresses, which is different from most observations of the asymptotic state. Even at $T = 550$, at which time the layer is 10 times its initial thickness, the anisotropy tensor of Case 6 is far from the asymptotic one.

Next, let's look at the medium-amplitude cases. The B_{ij} for the medium-amplitude cases (5,7,9,10,11), are shown in Figs. 5.8.3 through 5.8.7. Comparison of Figs. 5.8.1 and 5.8.3, which represent cases with the same initial field except for the amplitude, are quite similar, except that in the case with higher initial amplitude (5), the gradient component of the normal stress never becomes dominant. The case shown in Fig. 5.8.4, which is a higher amplitude version of the case shown in Fig. 5.8.2, does display dominance of the gradient component at later times, but the dominance is not as strong as in the low initial disturbance level case. Thus it appears that increasing the amplitude of the initial disturbance decreases the dominance of the gradient component of the normal stress; this will be further verified when we consider the high amplitude cases below.

Figures 5.8.3 and 5.8.6 represent two cases which are identical except that the latter one does not have a subgrid scale model. As can be seen, the effect of the model on B_{ij} is quite small; this is consistent with what we have observed about the effect of the model earlier. The case (9) shown in Fig. 5.8.5, which is identical to Case 5 just considered except for lack of filter and model, is similar to the other two; the most significant difference is that the spanwise normal stress plays a more important role at earlier times in the unfiltered case. This behavior is closer to what has been observed in the laboratory than the other two cases. The shear stress is also smaller and closer to the experimental data in this case. It seems that a significant portion of the spanwise stress resides in the small scales; further evidence of this will be given later. However, the small scales seem to destroy the shear stress. Unfortunately, in this case the numerical method became unreliable at a much earlier time, and we could not follow the development as long as in the other two cases with the present code. The solution to this difficulty lies in constructing a code with a greater number of grid points in the horizontal directions, and we recommend that this be done. The case (11) shown in Fig. 5.8.7, with initial conditions which are relatively deficient in small scales, produces greater dominance of the streamwise normal stress at early times and of the gradient stress at later times. Also, the high shear stress is maintained longer; this is a reflection of the more rapid growth of the layer in this case.

Finally, we examine the high-amplitude cases. Figures 5.8.8 and 5.8.9 show the B_{ij} for the high amplitude cases (2 and 8). The changes noted in going from the lowest amplitude to the medium amplitude are even more obvious in these cases. Relative to the case shown in Fig. 5.8.3, which has the same initial condition except for amplitude, Fig. 5.8.8 shows less dominance of the streamwise normal stress at early times and of the gradient stress at later times; all of the stresses show less variation with time, and the asymptotic state seems to be reached more quickly. The same effects are seen in comparing Figs. 5.8.4 and 5.8.9, but the change is perhaps less dramatic.

In summary, in some cases the components of Reynolds stress anisotropy tensor appear to reach asymptotic values after the layer has thickened only by a factor of four. In other cases no asymptotic value is in evidence after a thickening by as much as a factor of 10. This illustrates the enormous sensitivity of the Reynolds stress anisotropy tensor to the initial disturbance field. This sensitivity is more strongly coupled to the phase relationships of the initial conditions than to their amplitude or spectrum shape. The fact that we have only a couple large eddies in our computation increases this sensitivity; it also shows that large eddies can vary considerably, though variations may be small in a given laboratory experiment, due to phase locking.

5.9 Correlation Coefficient at the Center of the Mixing Layer

In this section we shall examine the correlation coefficient of the Reynolds' shear stress. It can be defined at the center of the layer as

$$c(uw) = \frac{\langle \tilde{u}(x,y,o)\tilde{w}(x,y,o) \rangle}{\left\{ \langle [\tilde{u}(x,y,o)^2]^{1/2} \rangle \langle [\tilde{w}(x,y,o)^2]^{1/2} \rangle \right\}}$$

The correlation coefficient can range between -1.0 and 1.0. In most shear flows studied in the laboratory it has a value of -0.45 ± 0.05 . However, Shirani et al. (1981) found values as large as -0.75 in a simulation of a homogeneous shear flow.

The correlation coefficients for the seed #1 cases are shown in Fig. 5.9.1, and those for seed #2 are shown in Fig. 5.9.2. The collapse of the data is remarkable. The values also seem realistic for the mixing layer, particularly in the near field.

Next, we shall look at the effect of changing the seed while maintaining constant initial amplitude. The correlation coefficients for the three amplitudes used are shown in Figs. 5.9.3-5. For the low and medium amplitude cases, the collapse of the results is considerably poorer than is the case when the seed is held constant and the amplitude varied. The exception is the high amplitude set of cases, for which an excellent collapse of the data is found.

Thus we find that the phases in the initial conditions have a stronger effect on the correlation coefficient than do the amplitudes in

the low to medium initial-amplitude cases. For high initial amplitude cases, the initial phases are not very important.

5.10. Resolution and Statistical Validity

In Figs. 5.10.1 through 5.10.5, the accuracy parameter η_A , the alias-free fraction η_{AF} , and sample number η_S defined in Section 3.5 are plotted.

Comparison of the sample number of case 5 (Fig. 5.10.2) with that of case 10 (Fig. 5.10.3) shows that the subgrid scale model extracts most of its energy at the higher wavenumbers, as it should.

Recalling that cases 5, 9, and 10 all have the same initial condition, we note that case 9 (no filtering or subgrid model), shown in Fig. 5.10.4, shows a strong increase in the sample number, and resolution is questionable after, say, $T = 140$. On the other hand, the Case 10 (no model) results are nearly the same as those of Case 5. Filtering thus has a much larger influence than does the model.

In contrast to general decline of η_S in the small and medium-amplitude cases, Figs. 5.10.4-5 show that in the high-amplitude initial disturbance cases, η_S hardly changes at all. In general, the effects of initial amplitude on these parameters are not large.

The figures show that, with the exception of Case 9, there is good spatial resolution in the central horizontal plane. Again, except for Case 9, two to four "characteristic" large eddies are captured in the computations. This is a very small sample, so extreme care is needed in comparing the results of these computations with those of experiments which are averages over many large eddies.

5.11. Particle-Tracking Visualizations

To complement the quantitative information given in the previous sections flow visualization pictures are presented in this section. The flow visualization pictures were obtained by tracking the intersections of the grid shown in Fig. 5.12.1. Plan views are views along the z axis, with the mean flow in the horizontal direction. One can consider the grid lines as dye or smoke lines put into the flow. For Cases 5

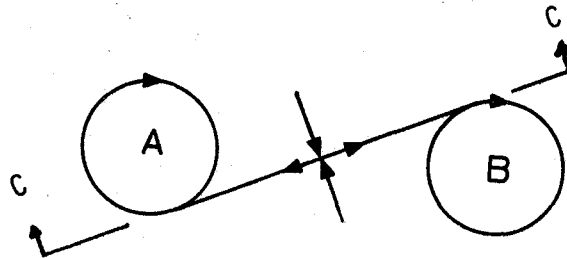
through 11, this grid (5.12.1) was placed in the horizontal midplane of the mixing layer at the initial time. The intersections move with local fluid velocity; the numerical method for doing this is described in Section 3.6. For the small (4 and 6) and medium (5,7,9,10, and 11) amplitude initial disturbance cases, the vertical lines in Fig. 5.11.1 are essentially vortex lines because the vorticity of the disturbance field is weak compared to the mean flow vorticity in these cases. For the high-amplitude disturbance cases, the vertical lines are only a crude approximation to vortex lines, as the initial disturbance vorticity is no longer negligible compared to the vorticity of the mean field.

In order to help the reader understand the visualizations, we shall now present some basic background on shear-layer instability. The primary instability of a time-developing mixing layer is the Kelvin-Helmholtz instability. The most amplified eigenfunction according to linear stability theory is spanwise uniform and, if acting alone, would ultimately result in a vortex array which is uniformly spaced in the streamwise direction (see Betchov and Criminale, 1967).

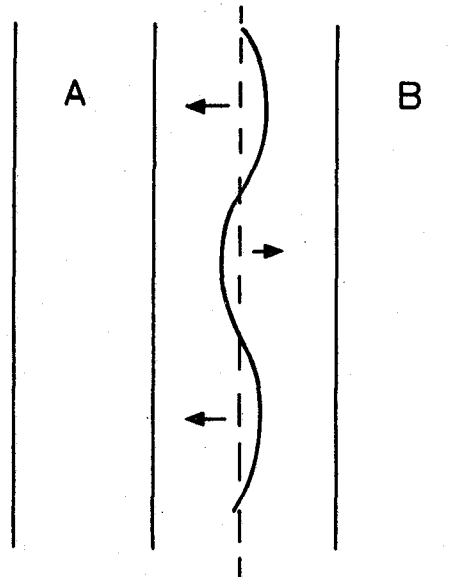
In the computations presented here, broad spectrum, random phase, finite-amplitude, 3-D initial disturbance fields are introduced. This random disturbance can be expressed as a linear combination of the eigenfunctions of the linearized equations and the eigenfunctions which grow most rapidly in time will become dominant if the initial disturbance amplitude is sufficiently small. In the low amplitude initial disturbance cases, a number of the eigenfunctions of the linearized equations grow rapidly so that the flow is not dominated by the single most amplified 2-D eigenfunction, i.e., the 3-D eigenfunctions are important.

The time development of the marker lines for Case 6 is shown in plan view in Figs. 5.11.2 through 5.11.7. In Fig. 5.11.2, we see the roll-up of the vorticity layer into two more or less coherent spanwise vortex structures (similar to what the primary Kelvin-Helmholtz instability would produce). A mechanism of secondary instability is also suggested by this figure. The secondary instability is caused by the straining field created by the primary vortex structures. To see how

this occurs, let us consider the spanwise view of the mixing layer, shown below.



The nearly two 2-D vortex structures (A + B) produce straining field or stagnation line flow midway between them as indicated by the arrows. Vortex A will entrain irrotational fluid from quadrant A', while B entrains from quadrant B'. Also note that, if the vortex structures have spanwise variation in strength or position, the stagnation line will not be straight. A plan view of plane C-C is shown below.



The wavy solid line represents the stagnation line, and the dashed line might represent a vortex line in the "braid" between vortices A and B. Due to the waviness of the stagnation line, the vortex line will be pulled in the directions shown by the arrows. This will turn the vortex line, aligning it with the flow. Eventually, most of the vorticity in

the secondary vortices will be aligned with the stretching direction of the straining field. We refer to this turning and alignment process as "secondary instability."

The secondary instability produces streamwise and gradient components of the vorticity. This completed state has been observed at Caltech by Konrad (1976) and Roshko (1980). The secondary instability is a very efficient mechanism for entrainment of irrotational fluid from the outer part of the flow into the primary vortex structure. Roshko (1980) shows that the secondary instability increases the mixing in the shear layer and that $d\theta/dt$ increases by 10%. A similar mechanism of entrainment was proposed by Corcos (1981).

With this mechanism for formation of the secondary vortices in mind, let's now discuss the other cases. The discussion proceeds from the small to the large amplitude cases.

In Case 6, the primary and secondary vortex structures are clearly delineated and are well formed by $T = 200$ (Fig. 5.11.3). The primary vortices each have slightly less than half the total circulation. The part of the secondary vortex marked a-b in Fig. 5.11.3 contains three vortex lines suggesting that it has a circulation of approximately 30% of the circulation of the primary vortices; this is larger than the value suggested by Roshko (1980). There is also a weaker secondary vortex forming in the center of Figs. 5.11.2-3, but it is harder to see. In Figs. 5.11.4-5, the two primary vortex structures are moving closer together and beginning to pair, and Figs. 5.11.6-7 show a spanwise view of this process. It should be noted that, while the primary vortices are not straight, they are nonetheless pairing in an essentially uniform fashion along the length of the vortex structures.

Interesting effects are seen near the centers of the two primary vortices. The one on the right hand side of these figures is more curved in the early stages of the rollup. The streamwise component of the vorticity resulting from the curvature apparently enhances the entrainment of irrotational fluid into the center of the vortex. This does not happen in the straighter vortex on the left. When the vortices begin to pair, the fatter section of the right hand vortex is heavily

strained and is torn apart. This appears to be another mechanism for the creation of streamwise vorticity.

Case 7, which is identical to Case 6 except that the initial disturbance energy is two orders of magnitude larger, behaves in a qualitatively similar way to Case 6. Fig. 5.11.8 is quite similar to Fig. 5.11.4 and we see that increasing the amplitude has caused the development to take place faster but has not produced any important structural changes.

Case 8, which has an initial disturbance energy two orders of magnitude greater than Case 7, behaves in a more chaotic manner. Recall that in this case the vertical marker lines of Fig. 5.11.1 are not vortex lines. Fig. 5.11.9 shows that there is a tendency for the markers to agglomerate in this case but the pattern is different. The development is also more rapid.

Cases 5 and 10 have identical initial conditions; the only different is that Case 10 has no model. They develop in a very similar manner and only Case 10 will be presented here. These cases differ from Case 7 only in the set of random phases in the initial condition. At $T = 76$ (Fig. 5.11.10), it is immediately apparent that Case 10 does not roll up into a pair of well defined vortices. The vortices are inclined and branch in a complicated manner not seen in Case 6; local (rather than uniform) vortex pairing is taking place. The distinction between local and uniform pairing is probably the key to reconciling the Bradshaw and Browand-Roshko models of the development of the shear layer. In Chandrsuda et al's (1978) visualization, there is local (in Bradshaw's terminology, helical) pairing, while in Winant and Browand's (1974) visualization there is essentially uniform pairing along the entire span of the vortices. Uniform pairing may persist indefinitely, as Browand's experiments suggest, if three dimensional perturbations can be excluded in the early stages of development; the strong two dimensional vortices will not be modified greatly by weak three dimensional perturbations after rollup has been completed. On the other hand, if the near field has local or helical pairing, it will probably break down into the chaotic state normally associated with turbulence. The development of

Case 10 is shown in Fig. 5.11.10 through 5.11.15. The local or helical pairing is immediately apparent.

When filtering is eliminated, as in Case 9, the initial rollup is not very different (compare Figs. 5.11.10 and 5.11.6). However, the later development is much more irregular as can be seen by comparing Figs. 5.11.14 and 5.11.17 and Figs. 5.11.15 and 5.11.18. It is difficult to be certain of the reasons for this but it appears that the difference may be due to the fact that filtering tends to remove (or, at least, diffuse) kinks in the vortices. Since highly kinked vortices are very energetic, they are capable of producing the chaotic pattern seen in Figs. 5.11.17 and 5.11.18. Also recall that the numerical methods lose their accuracy after about $T = 140$ in this case.

In Case 11, the initial condition is richer in the large scales and leaner in the small scales, relative to the other cases. Nevertheless, the development of this flow is not greatly different from those presented above. At the relatively early time shown in Fig. 5.11.19 there are three vortices. The first two are close together at the upper left while the other two are close at the center right of the figure. It is not surprising that this arrangement leads to local pairing of the center vortex with the left one at the top and with the right one near the center. Fig. 5.11.20 clearly shows this to be the case; also note that the left vortex has developed a considerable amount of curvature at the time corresponding to this figure. To understand what happens next it is important to remember that the boundary conditions are periodic and the flow actually being computed can be constructed by repeating the figure to the left and right (and above and below) itself to form an infinite array. The center of the left vortex now begins to pair with the center of the right one. This causes the left vortex to become still more curved and the resulting streamwise vorticity pushes the part of the right vortex closest to it downward. This produces a downward kink in the right vortex and the marker points seem to be drawn together in the spanwise direction when viewed from above. The result is shown in Fig. 5.11.21. The spanwise view of this flow is shown in Figs. 5.11.22 and 5.11.23.

The figures and arguments presented in this section provide insight into the nature of the processes that occur in mixing layers. The initial layer always seems to rollup into a configuration in which the spanwise vorticity is more concentrated than it was initially. The precise structure of the rolled up layer seems to depend on the initial disturbance field in a way that would be hard to predict simply knowing the spectrum. It is possible to produce layers with straight two-dimensional vortices, ones with curved vortices, and ones with vortices arranged in a 'fishnet' pattern. The subsequent dynamics of the layer depends very much on the configuration produced by the initial rollup. Pairing seems to play an important role in the later development, but it may take the form of either simple uniform pairing of two vortices or local pairing in which different parts of the same vortex pair with parts of different neighboring vortices. Local pairing leads to much more three dimensionality than does simple uniform pairing, but it looks as if there will always be large regions of concentrated vorticity in the mixing layer and that these will grow by agglomeration as the layer develops.

Finally, we should note that all of these results are for the time-developing mixing layer. In the spatially-developing mixing layer studied in the laboratory there are important feedback effects. Pressure fluctuations created in the downstream part of the flow can influence the upstream development strongly. It is quite possible that this feedback can cause the layer to 'lock on' to a particular structure which is then maintained for a long time.

Chapter 6

CONCLUSIONS

This study of the mixing layer has focused on the physics of transition and early turbulence in a time-developing mixing layer. The effort was concentrated on the effect of initial disturbance field on the later character of the turbulence.

Concern about the possible influence of image flows (which are implied by the boundary conditions) on the computations led to the development of a new infinite domain orthogonal function expansion. Use of the discrete form of this new method in the computations eliminates the influence of image flows by keeping them an infinite distance from the flow of interest.

This new and very accurate numerical differencing and integrating scheme for infinite domains was presented. It is based on the use of Fourier expansions and takes advantage of the computational efficiency of the fast Fourier transform. The new method is applicable to more general boundary conditions than the standard Fourier method, due to the use of mapping functions. (The simplest boundary conditions to implement are periodicity, or zero, or zero-derivative conditions, or combinations thereof.) However, the allowed mapping functions are restricted for reasons of efficiency and accuracy. For more detail, see Chapter 3.

Two particular mapping schemes, both for doubly infinite domains, were implemented. One was chosen to handle jet-type flows, while the other was designed for the mixing layer. Both schemes were applied to linear test equations having known analytical solutions. The new scheme was shown to have errors as much as six orders of magnitude smaller than common finite-difference schemes for equal numbers of mesh points.

Using the new infinite-domain scheme, a 3-D, time-dependent, large-eddy simulation study of transition and early turbulence in a time-developing mixing layer was undertaken. The primary focus of this study concerned the effect of the initial disturbance field on turbulence development. Effects due to filtering and modeling were also examined.

To sort out the effects of the initial disturbance field, the same laminar, mean-velocity profile was used as the initial mean field in all cases. To this mean velocity field, an initial divergence-free disturbance field was added. We used nine cases involving seven different initial disturbance fields. These seven cases allowed us to examine the influence of the disturbance amplitude, spectrum shape, and random phase sets on the resulting early turbulence.

The computations provided the mean velocity profile, the momentum thickness, the turbulent kinetic energy, the Reynolds stress tensor, the Reynolds stress anisotropy tensor, and particle tracking pictures. Examination of these results provided new understanding of the mixing layer. Key results of this work are summarized below:

- Self-similarity in the mean velocity profile develops very quickly; the self-similar profile is independent of initial conditions.
- The momentum-thickness growth rate is strongly influenced by the initial disturbance-spectrum shape.
- Interesting oscillatory behavior occurs in the width of the kinetic energy profile for the small-amplitude initial disturbances. This oscillatory behavior is not present if the initial disturbance is large.
- The anisotropy tensor is a very sensitive measure of self-similarity. Even changing the random phase distribution in the initial disturbance field produces enormous differences in the evolution of the anisotropy tensor.

Probably the most significant aspect of the study was revealed in the particle-track pictures. Large coherent structures readily appeared (some similar to those of Winant and Browand (1974) and others like Chandrsuda et al. (1978)). More important, the mechanism for producing the secondary vortices was identified. These vortices develop as a result of spanwise variations in the strength or position of the primary vortex structures, which give rise to spanwise variations in the straining field stagnation line. This causes the formation of pairs of counter-rotating secondary vortices aligned with the straining field.

The statistical and structural characteristics of the mixing layer are very sensitive to the phases of the initial disturbance. This may explain the differences that have been observed among different experimental setups, each of which produces a given type of large eddy structure. Thus, large eddy variation may be small in a given experiment, but significant variations may occur from experiment to experiment.

Two cases were run to examine the effects of filtering and subgrid turbulence modeling. We found that filtering delays the onset of nonlinear effects and gives us less than the total picture. However, it considerably extends the length of time over which the computation is meaningful. The subgrid-scale model was shown to have very little influence on the calculation of the early stages of transition.

Appendix A

FINITE DIFFERENCE METHODS

For non-uniformly spaced data, we may define

$$\Delta_j = x_{j+1} - x_j$$

and use the three-point finite-difference approximation

$$\left. \frac{\delta u}{\delta x} \right|_{x_j} = au_{j-1} + bu_j + cu_{j+1} \quad (\text{A.1})$$

where

$$a = -\frac{1}{\Delta_{j-1}^2/\Delta_j + \Delta_{j-1}}; \quad c = \frac{1}{\Delta_j + \Delta_j^2/\Delta_{j-1}}; \quad b = -a - c$$

From a Taylor series, expansion (A.1) can be shown to be second-order accurate in Δ_j . On the other hand, the two-point formula

$$\left. \frac{\delta u}{\delta x} \right|_{x_j} = au_{j-1} + bu_{j+1} \quad (\text{A.2})$$

with

$$a = -b = -\frac{1}{x_{j+1} - x_{j-1}}$$

is first-order accurate and becomes second-order accurate as $\Delta_{j-1} \rightarrow \Delta_j$. For the second derivative, the approximation:

$$\left. \frac{\delta^2 u}{\delta x^2} \right|_{x_j} = au_{j-1} + bu_j + cu_{j+1} \quad (\text{A.3})$$

with

$$a = 2/[\Delta_{j-1}(\Delta_j + \Delta_{j-1})]$$

$$b = -2/\Delta_j\Delta_{j-1}$$

$$c = 2/\Delta_j(\Delta_j + \Delta_{j-1})$$

is first-order accurate and becomes second-order accurate as $\Delta_{j-1} \rightarrow \Delta_j$.

Appendix B

TIME-INTEGRATION SCHEMES

Given $dy/dt = f(y,t)$, the second-order Adams-Bashforth scheme is

$$y^{n+1} = y^n + \Delta t(1.5f^n - 0.5f^{n+1}) \quad (\text{B.1})$$

The fourth-order Runge-Kutta scheme is

$$\begin{aligned} y^{n+1} = y^n + \Delta t & \left[\frac{1}{6} f(y^n, t^n) + \frac{1}{3} f(y^{*n+1/2}, t^{n+1/2}) \right. \\ & \left. + \frac{1}{3} f(y^{**n+1/2}, t^{n+1/2}) + \frac{1}{6} f(y^{*n+1}, t^{n+1/2}) \right] \end{aligned} \quad (\text{B.2})$$

where

$$\begin{aligned} y^{*n+1/2} &= y^n + \frac{\Delta t}{2} f(y^n, t^n) \\ y^{**n+1/2} &= y^n + \frac{\Delta t}{2} f(y^{*n+1/2}, t^{n+1/2}) \\ y^{*n+1} &= y^n + \Delta t f(y^{**n+1/2}, t^{n+1/2}) \\ t^{n+1/2} &= t^n + \Delta t/2 \end{aligned}$$

The second-order Runge-Kutta method is

$$\begin{aligned} y^{n+1} &= y^n + \Delta t f(y^{*n+1/2}, t^{n+1/2}) \\ y^{*n+1/2} &= y^n + (\Delta t/2) f(y^n, t^n) \end{aligned} \quad (\text{B.3})$$

Appendix C
SUBGRID MODELING

C.1 A New Model

Recall from Section 2.5 that subgrid scale field is the difference between the velocity u_i and filtered velocity, denoted \bar{u}_i . While we refer to u_i' as "subgrid scale," it in fact has some components in the resolved domain. A new modeling concept involves exploiting this fact. We use the following decompositions:

$$u_i = \bar{u}_i + u_i' \quad (C.1.1)$$

$$u_i' = u_i'' + u_i'''$$

where

$$\hat{u}_i'(k) = \begin{cases} \hat{u}_i''(k) & ; \quad k \leq k_c \\ \hat{u}_i'''(k) & ; \quad k > k_c \end{cases}$$

k_c is the highest computed wavenumber. Therefore

$$u_i''(k) = \frac{(1 - \hat{G}(k))}{\hat{G}(k)} \hat{u}_i(k)$$

We propose that

$$\tau_{ij} = C_1 T_{ij} + C_2 m_{ij} \quad (C.1.2)$$

where

$$T_{ij} = \overline{\bar{u}_i u_j''} + \overline{u_i'' \bar{u}_j} + \overline{u_i'' u_j''} \quad (C.1.3)$$

and

$$m_{ij} = \frac{T_{\ell\ell}}{\bar{S}} \bar{S}_{ij} \quad (C.1.4)$$

$$\bar{s}_{ij} = \frac{1}{2} \left[(\bar{u}_i - \langle \bar{u}_i \rangle),_j + (u_j - \langle u_j \rangle),_i \right]$$

$$\bar{s} = (\bar{s}_{ij} \bar{s}_{ij})^{1/2}$$

Using the high wavenumber spectrum of Comte-Bellot and Corrsin (1971)

$$D(k) = \alpha \epsilon^{2/3} k^{-5/3} \exp \left[-\frac{3}{2} \alpha (k\eta)^{4/3} \right] \quad (C.1.5)$$

We evaluate this expression for the highest computed wavenumber k_c using the experimental value, $\alpha = 1.5$, to get

$$E(k) = \beta k^{-5/3} \exp \left[-\frac{3}{2} \alpha (k\eta)^{4/3} \right]$$

$$\beta = \frac{(k_c)^{5/3} E(k_c)}{\exp \left[-\frac{3}{2} \alpha (k_c \eta)^{4/3} \right]}$$

where the Kolmogorov microscale $\eta = (\nu/q^3)^{1/4}$. This gives C_1 as

$$C_1 = \frac{\int_{k_c}^{1/\eta} E(k) dk}{\langle T_{ii} \rangle} \quad (C.1.6)$$

since $m_{ii} = 0$. To evaluate C_2 , we use Lumley's expression for the energy transfer spectrum:

$$T(k) \approx \frac{0.5\pi}{\alpha^{3/2}} k^{5/2} E(0.4k) E^{1/2}(k) \quad (C.1.7)$$

and therefore

$$C_2 = \frac{T(k_c) - \langle u_i T_{ij,j} \rangle}{\langle u_i m_{ij,j} \rangle}$$

This model is for homogeneous flow and therefore was not used in the present work. With more development, it may be used in flows with homogeneity in two directions. Jorge Bardina is testing models using similar ideas and is getting very promising results.

Appendix D

IMAGE FLOWS

In solving problems in fluid mechanics, boundary conditions are often applied at finite boundaries. If this is done for a flow which actually extends to infinity, the boundary conditions imply artificial image flows. If one is not careful, the image flows may render the results meaningless. The new Fourier method described earlier puts the image flows infinitely far away, thus eliminating this difficulty.

Suppose we want to compute the flow due to two vortices of the same sign. If we were to use discrete cosine and sine expansions on a finite uniform grid, we would be applying a no-stress boundary condition at some finite distance from the vortices. This implies an infinite array of pairs of vortices with alternating signs of vorticity. In order to assess whether the image flows (a finite distance away) affect the computed solution, we performed the following numerical experiment. First we placed two pairs of vortices of opposite sign a distance $d/2$ above and below the x axis, as shown in Fig. D.1. The vortices had elliptical Gaussian distributions of vorticity and a separation of distance c . The upper vortices will rotate about one another in a clockwise manner, while the lower pair will rotate counterclockwise. If the pairs are far enough apart not to affect each other, we should be able to shift the location of the lower pair by a distance $c/2$ in the x direction and get identical results. In performing this calculation, we used the mapping given by Eq. (3.3.5). We used the standard Fourier method for differentiating in the x direction and the second-order Adams-Bashforth scheme for the time advance. We used 16 grid points in the x direction and 128 in the z direction. The vortex pairs were centered at grid points 59 and 71 in z , and grid points 5 and 11 in x . The coefficient of the mapping function a was $a = 192/\pi$ (this gives $\Delta z = 1.5$ near the origin); the x coordinates were $x_j = 2(j-1)$; the dimensionless time step was selected so that $(u_{\max}/\Delta x + w_{\max}/\Delta z_{\min}) \Delta t = .3$. We did this calculation by solving the vorticity equation:

$$\frac{\partial}{\partial t} \omega + \frac{\partial}{\partial x} u\omega + \frac{\partial}{\partial z} w\omega = \nu \nabla^2 \omega \quad (\text{D.1})$$

and the vector potential given by

$$\nabla^2 \psi = -\omega \quad (\text{D.2})$$

to get

$$u = -\frac{\partial}{\partial z} \psi ; \quad w = \frac{\partial}{\partial x} \psi \quad (\text{D.3})$$

We computed until the dimensionless time $T = u_{\max} t / c = 1.0$, at which point we compared the "turbulent" kinetic energy in the full domain of the computation (with turbulence defined as the local deviation from an average in the x direction). For the case shown in Fig. D.1, the turbulent kinetic energy was the same at $T = 1$ and $T = 0$. However, when the lower pair of vortices was shifted by $c/2$, the kinetic energy at $T = 1$ was double the energy at $T = 0$.

We thus conclude that a computation in a domain of height 1.5 times the spacing between a pair of vortices would suffer tremendously from the influence of image flows. We also did the same calculation with $d/c = 4$ and found no significant image flow influence.

References

- Ashurst, W. T. (1979), "Numerical Simulation of Turbulent Mixing Layers via Vortex Dynamics," in Turbulent Shear Flows, I (F. Durst et al., eds.), Springer-Verlag, Berlin, 402-413.
- Bardina, J. Ferziger, J. H., and W. C. Reynolds (1980), "Improved Subgrid Scale Models for Large Eddy Simulation," AIAA paper 80-1537
- Betchov, R., and W. O. Criminale (1967), Stability of Parallel Flows, Academic Press, New York.
- Birch, S. (1980), "Data Evaluation Summary-Planar Mixing Layer," AFOSR-HTTM-Stanford Conference on Complex Turbulent Flows.
- Bradshaw, P. (1966), "The Effect of Initial Conditions on the Development of a Free Shear Layer," J. Fluid Mech., 26, Part 2, 225-236.
- Browand, F. K., and T. R. Troutt (1980), "A Note on Spanwise Structure in the Two-Dimensional Mixing Layer," J. Fluid Mech., 97, Part 4, 771-781.
- Brown, G. L., and A. Roshko (1974), "On Density Effects and Large Structure in Turbulent Mixing Layers," J. Fluid Mech., 64, Part 4, 775-816.
- Champagne, F. H., Y. H. Pao, and I. J. Wignanski (1976), "On the Two-Dimensional Mixing Region," J. Fluid Mech., 74, 209.
- Chandrsuda, C., R. D. Mehta, A. D. Weir, and P. Bradshaw (1978), "Effect of Free-Stream Turbulence on Large Structure in Turbulent Mixing Layers," J. Fluid Mech., 85, Pt. 4, 693-704.
- Clark, R. A., J. H. Ferziger, and W. C. Reynolds (1979), "Evaluation of Subgrid-Scale Turbulence Models Using a Fully Simulated Turbulent Flow," J. Fluid Mech., 91, 1.
- Comte-Bellot, G., and S. Corrsin (1971), "Simple Eulerian Line Correlation of Full- and Narrow-Band Velocity Signals in Grid-Generated 'Isotropic' Turbulence," J. Fluid Mech., 48, 273.
- Cooley, J. W., and J. W. Tukey (1965), "An Algorithm for the Machine Calculation of Complex Fourier Series," Math. Comput., 19, 90, 297-301.
- Corcos, G. (1981), Mech. Engrg. Dept., Univ. of California, Berkeley (private communication).
- Couët, B., and A. Leonard (1980), "Mixing Layer Simulation by an Improved Three-Dimensional Vortex-in-Cell Algorithm," Seventh International Conf. on Numerical Methods in Fluid Mechanics, Stanford Univ. and NASA-Ames Research Center.

Feiereisen, W. J., W. C. Reynolds, and J. H. Ferziger (1981), "Numerical Simulation of a Compressible, Homogeneous, Turbulent Shear Flow," Rept. No. TF-13, Mech. Engrg. Dept., Stanford Univ.

Kim, J. (1981), Mech. Engrg. Dept., Stanford Univ. (private communication).

Kline, S. J., and P. W. Runstadler (1959), "Some Preliminary Results of Visual Studies of the Wall Layers of the Turbulent Boundary Layer," ASME Paper No. 58-A-64, J. Appl. Mech.

Konrad, J. H. (1976), "An Experimental Investigation of Mixing in Two-Dimensional Shear Flows with Applications to Diffusion-Limited Chemical Reactions," Project SQUID. Tech. Rept. CIT-8-PU.

Kwak, D., W. C. Reynolds, and J. H. Ferziger (1975), "Three-Dimensional Time-Dependent Computation of Turbulent Flows," Rept. No. TF-5, MEch. Engrg. Dept., Stanford Univ.

Leonard, A (1974), "On the Energy Cascade in Large-Eddy Simulations of Turbulent Fluid Flows," Adv. in Geophysics, 18A, 237.

Leonard, A. (1980), "Vortex Methods for Flow Simulation," J. of Comp. Physics, 37, No. 3, 289-335, Oct.

Liepmann, H. W. (1979), "The Rise and Fall of Ideas in Turbulence," Am. Scientist, 67, 221-228 (1979).

Mansour, N. N., P. Moin, W. C. Reynolds, and J. H. Ferziger (1977), "Improved Methods for Large Eddy Simulation of Turbulence," Proc. Symp. on Turbulent Shear Flows, Penn. State Univ.

Mansour, N. N., J. H. Ferziger, and W. C. Reynolds (1978), "Large Eddy Simulation of a Turbulent Mixing Layer," Rept. TF-11, Dept. of Mech. Engrg., Stanford Univ.

Metcalf, R. W., and J. J. Riley (1980), "Direct Numerical Simulation of Turbulent Shear Flows," Seventh International Conf. on Numerical Methods in Fluid Dynamics, Springer-Verlag.

Michalke, A. (1965), "On Spatially Growing Disturbances in an Inviscid Shear Layer," J. Fluid Mech., 22, 371.

Miksad, R. W. (1972), "Experiments on the Nonlinear Stages of Free Shear Layer Transition," J. Fluid Mech., 56, Pt. 4, 695-719.

Miksad, R. W. (1973), "Experiments on Nonlinear Interactions in the Transition of a Free Shear Layer," J. Fluid Mech., 59, Pt. 1, 1-21.

Moin, P., W. C. Reynolds, and J. H. Ferziger (1978), "Large Eddy Simulation of Incompressible Turbulent Channel Flow," Rept. TF-12, Mech. Engrg. Dept., Stanford Univ.

- Moin, P., and J. Kim (1981), "Numerical Investigation of Turbulent Channel Flow," NASA TM-81309. Submitted for publication in J. Fluid Mech.
- Patel, R. P. (1973), "An Experimental Study of a Plane Mixing Layer," AIAA, 11, No. 1, 67-71.
- Orszag, S. A., and G. S. Patterson (1972), "Numerical Simulation of Three-Dimensional Homogeneous Isotropic Turbulence," Phys. Rev. Lett., 28, Pt. 2, 76.
- Phillips, O. M. (1954), "The Irrotational Motion Outside a Free Turbulent Boundary," Camb. Philos. Soc., 51, I, 220-229.
- Reynolds, W. C. (1976), "Computation of Turbulent Flows," Ann. Rev. Fluid Mech., 8, 183-208.
- Rogallo, R. S. (1981), "Numerical Experiments in Homogeneous Turbulence," Proc. AFOSR-HTTM-Stanford Conf. on Computation of Complex Turbulent Flows, Stanford Univ.
- Roshko, A. (1976), "Structure of Turbulent Shear Flows: A New Look," AIAA J., 14, 1349-1357.
- Roshko, A. (1980), "The Plane Mixing Layer Flow Visualization Results and Three-Dimensional Effects," Presented at an International Conf. on the Role of Coherent Structures in Modeling Turbulence and Mixing, Madrid, Spain.
- Shirani, E., J. H. Ferziger, and W. C. Reynolds (1981), "Mixing of a Passive Scalar in Isotropic and Sheared Homogeneous Turbulence," Rept. TF-15, Mech. Engrg. Dept., Stanford Univ.
- Smagorinsky, J. (1963), "General Circulation Experiments with the Primitive Equations," Mon. Weather Rev., 91, 99.
- Spencer, B. W., and B. G. Jones (1971), "Statistical Investigation of Pressure and Velocity Fields in the Turbulent Two-Stream Mixing Layer," AIAA Paper No. 71-613.
- Winant, C. D., and F. K. Browand (1974), "Vortex Pairing: The Mechanism of Turbulent Mixing-Layer Growth at Moderate Reynolds Number," J. Fluid Mech., 63, Pt. 2, 237-255.
- Wynanski, I., and H. E. Fiedler (1970), "The Two-Dimensional Mixing Region," J. Fluid Mech., 41, Pt. 2, 327-361.
- Wynograd, S. (1976), "On Computing the Discrete Fourier Transform," IBM Research Rept. RC-6291 (Proc. Nat. Acad. Sci., April 1976)

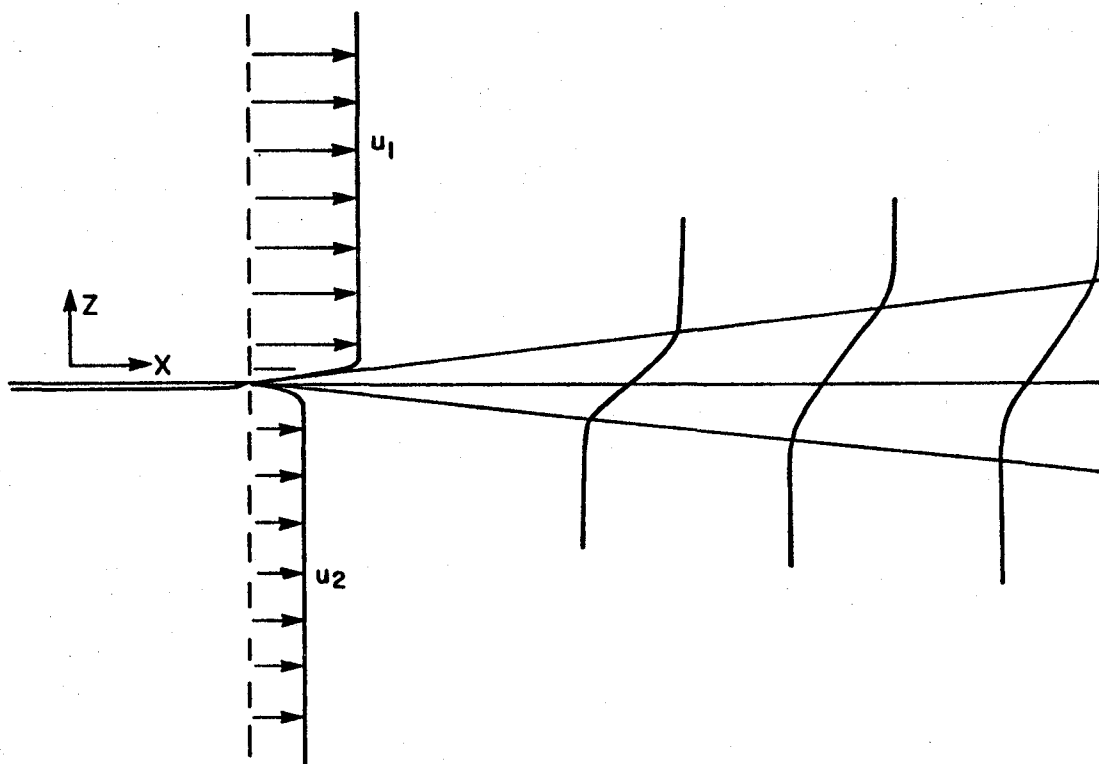


Fig. 1.3.1 The spatially developing mixing layer as created in the laboratory.

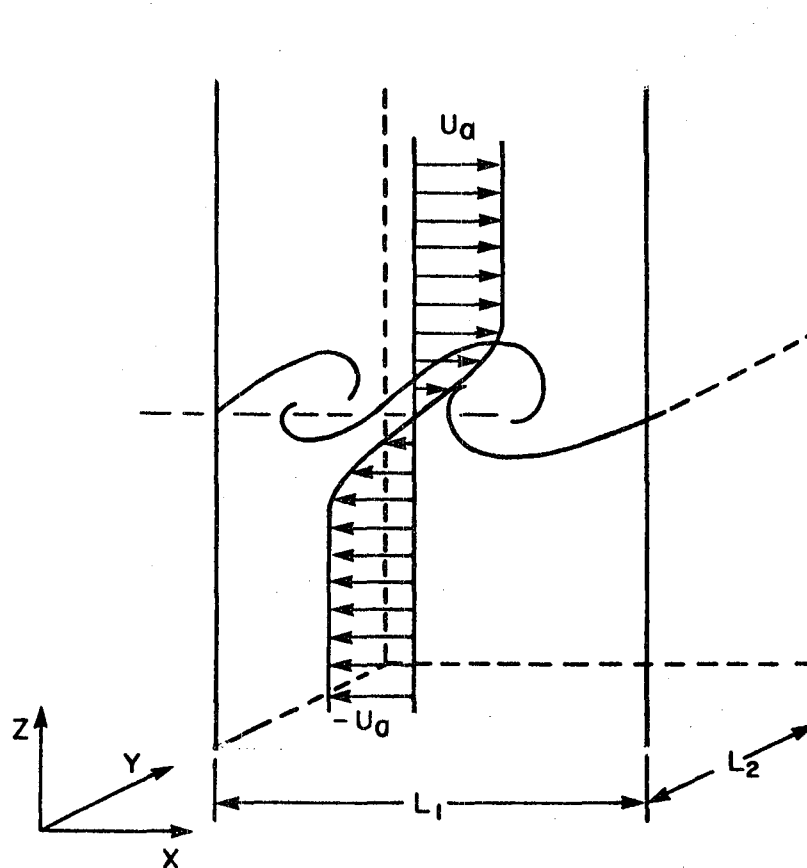


Fig. 1.3.2 The time-developing mixing layer studied in the present work.

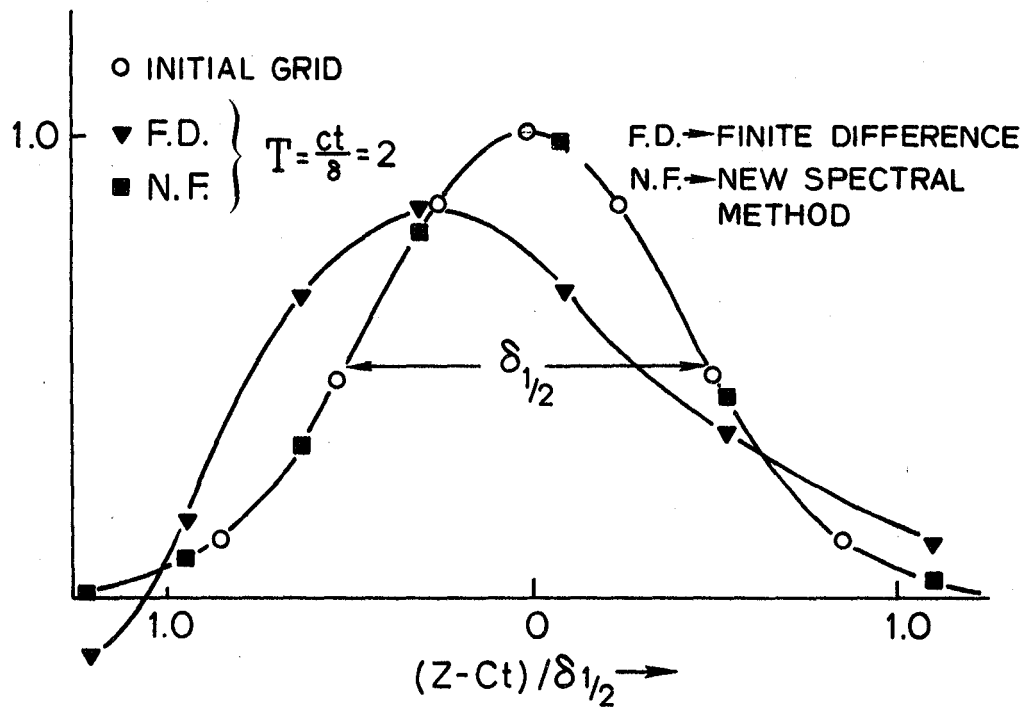


Fig. 4.1.1 Comparison of finite difference, new Fourier, and analytical solutions to the first-order convection equation.

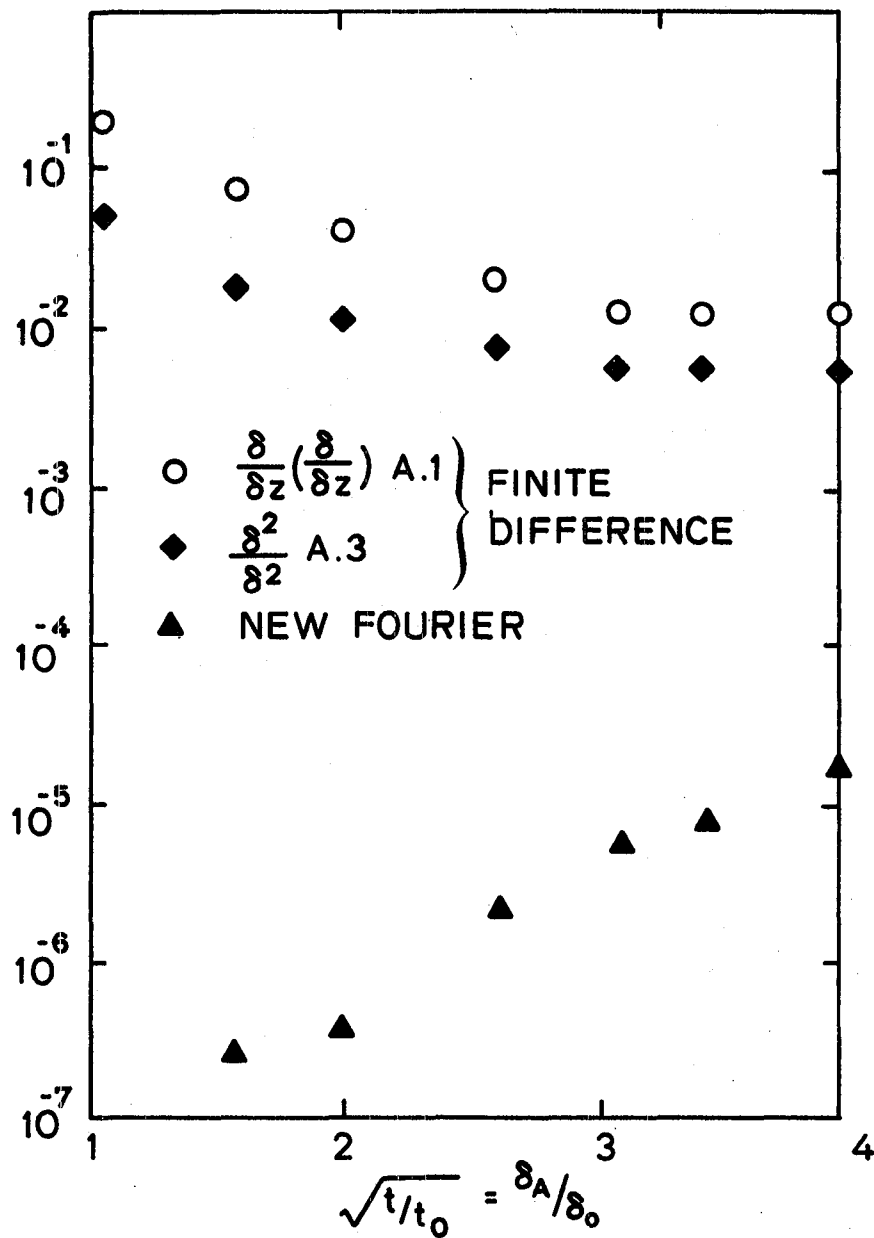


Fig. 4.2.1 Comparison of the maximum dimensionless errors of finite-difference and new Fourier solutions to the heat or diffusion equation.

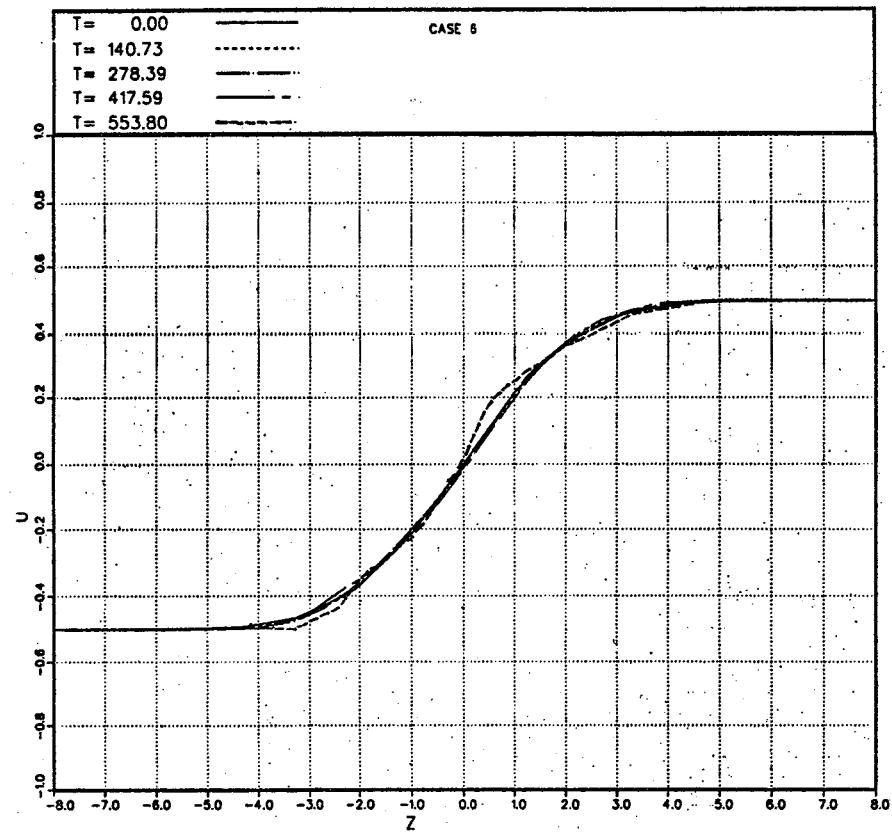


Fig. 5.3.1. Mean velocity profile at various times for Case 6.

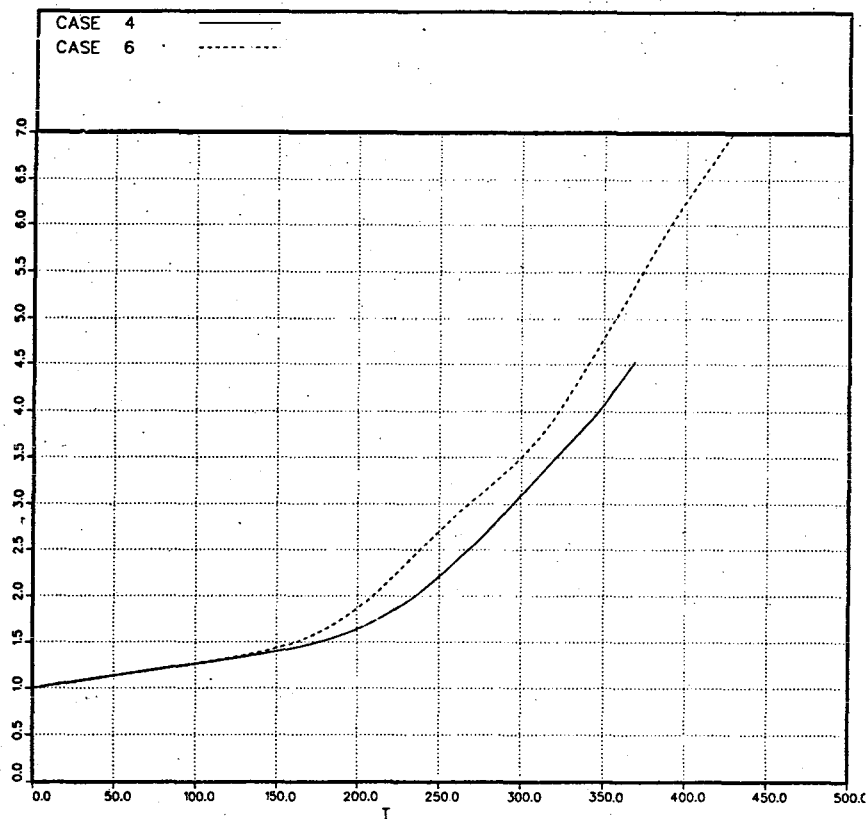


Fig. 5.4.1. Normalized momentum thickness vs. dimensionless time for low-amplitude Cases 4 and 6.

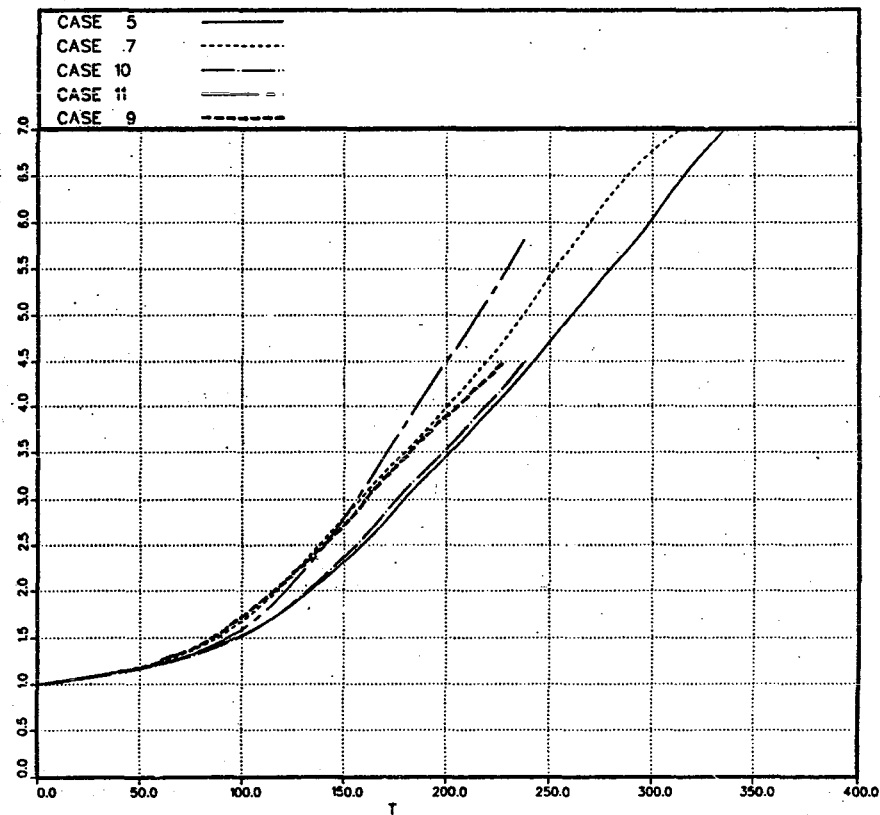


Fig. 5.4.2. Normalized momentum thickness vs. dimensionless time for medium-amplitude Cases 5, 7, 10, 11, and 9.

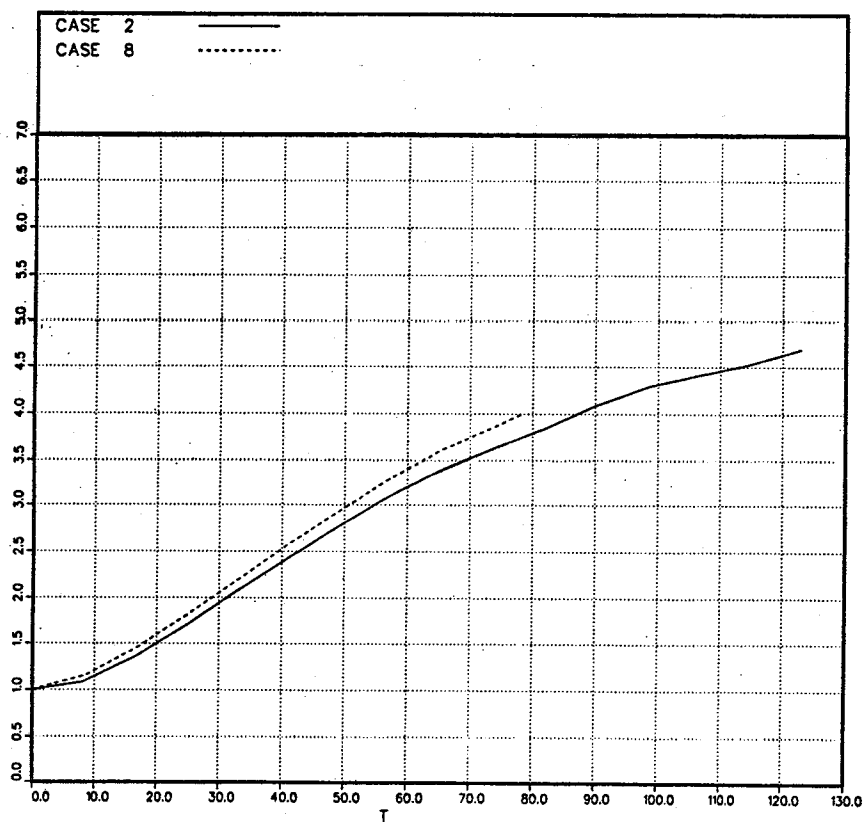


Fig. 5.4.3. Normalized momentum thickness vs. dimensionless time for high-amplitude Cases 2 and 8.

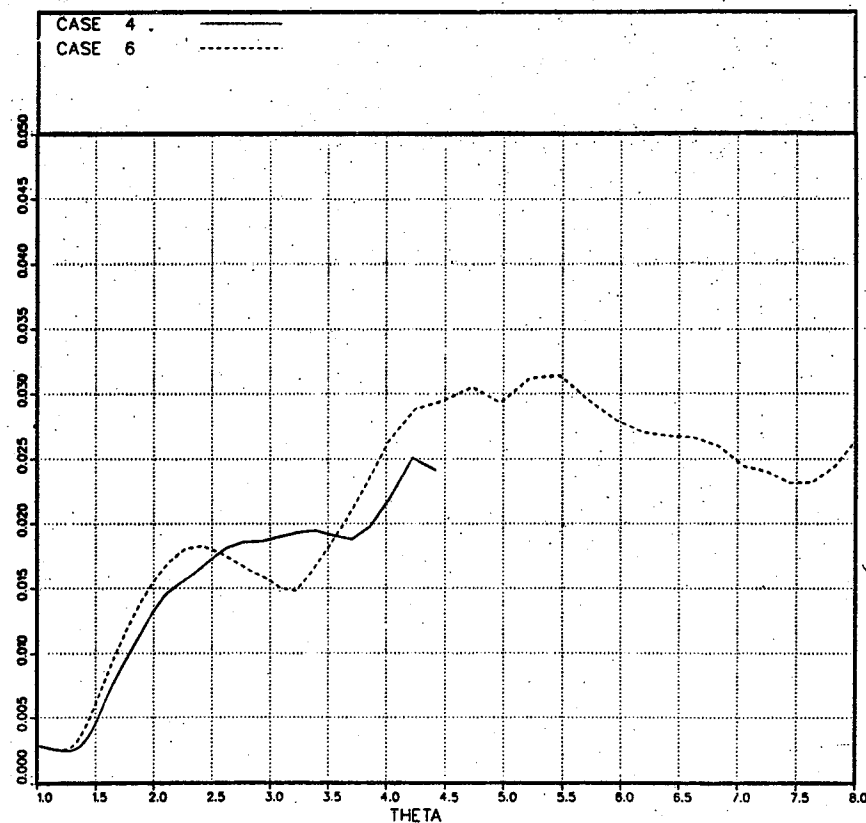


Fig. 5.4.4. Dimensionless momentum thickness growth rate vs. normalized momentum thickness for low-amplitude Cases 4 and 6.

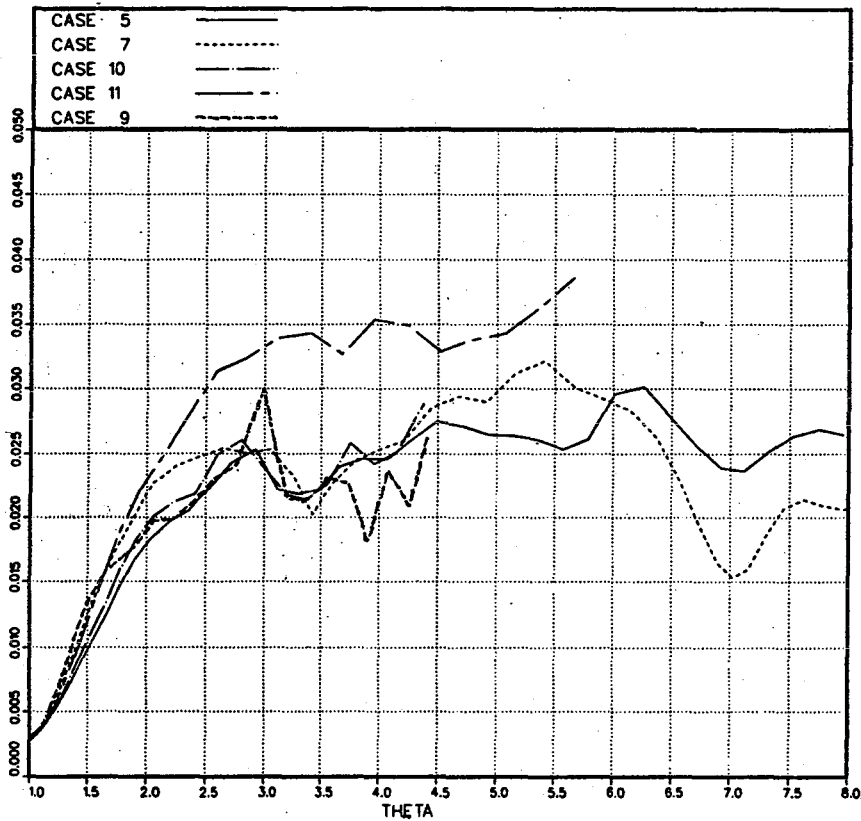


Fig. 5.4.5. Dimensionless momentum thickness growth rate vs. normalized momentum thickness for medium-amplitude Cases 5, 7, 10, 11, and 9.

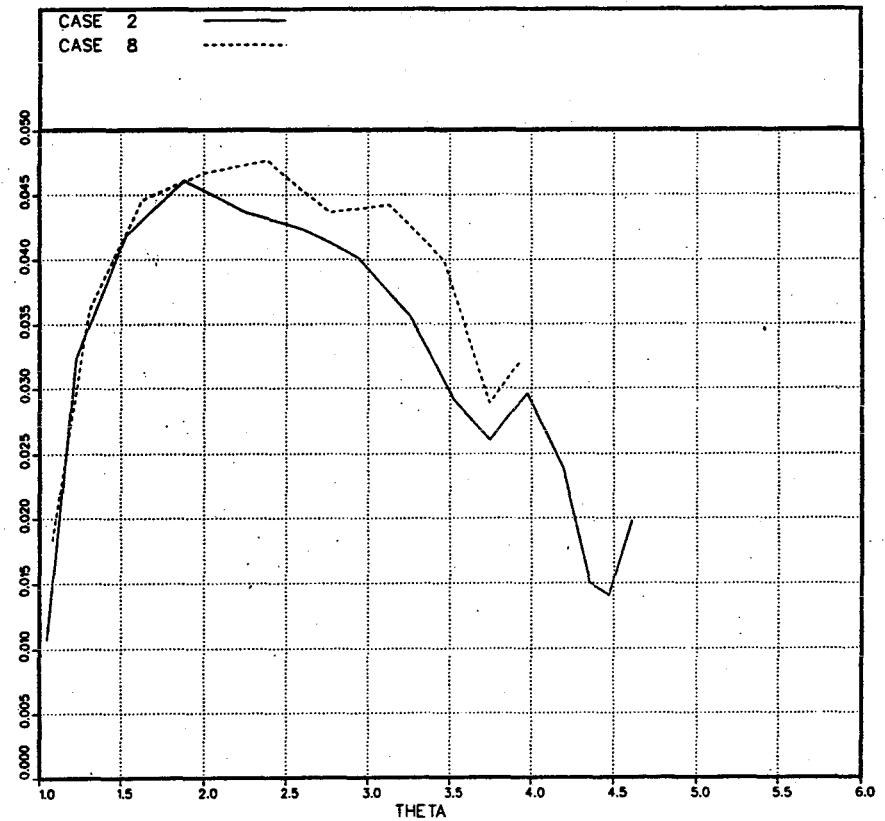


Fig. 5.4.6 Dimensionless momentum thickness growth rate vs. normalized momentum thickness for high-amplitude Cases 1 and 8.

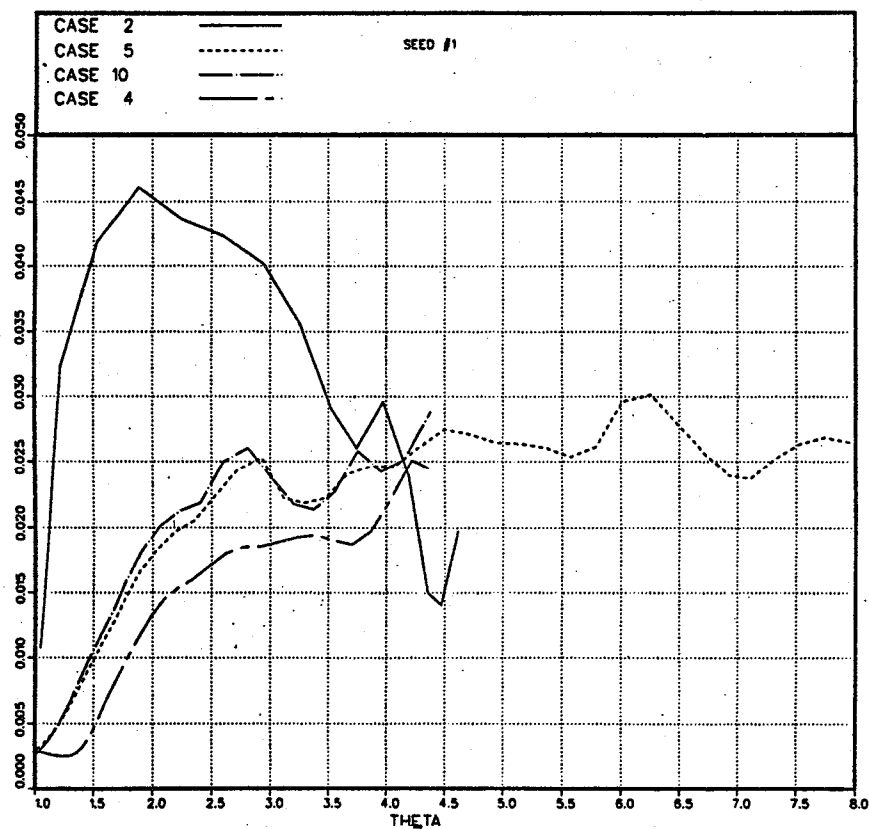


Fig. 5.4.7. Dimensionless momentum thickness growth rate vs. normalized momentum thickness for cases with seed #1.

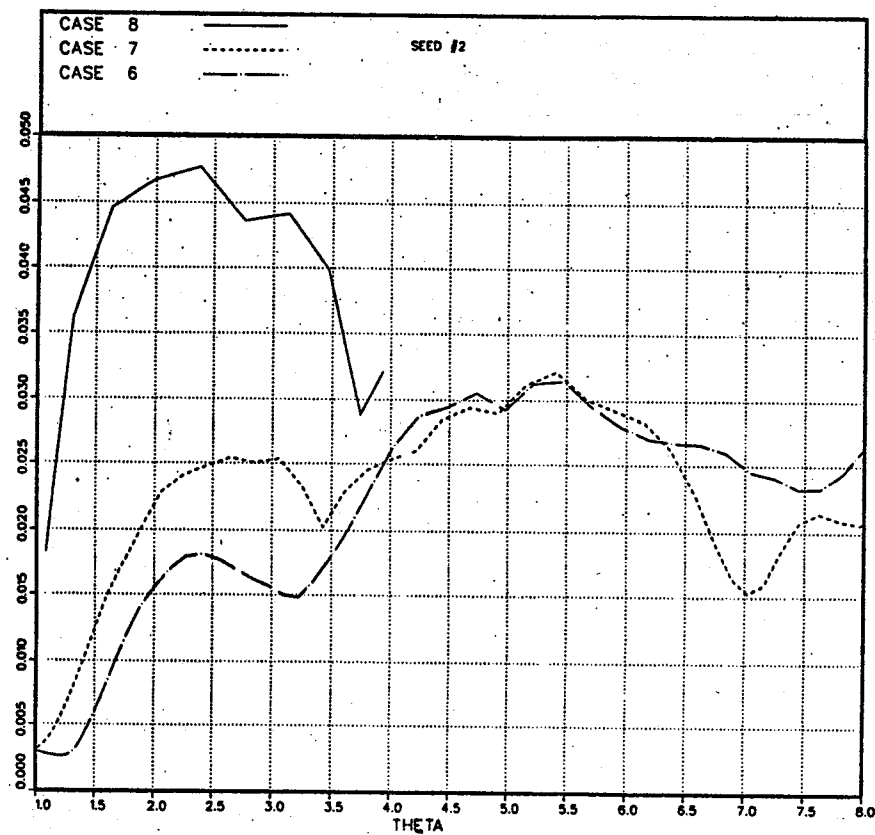


Fig. 5.4.8. Dimensionless momentum thickness growth rate vs. normalized momentum thickness for cases with seed #2.

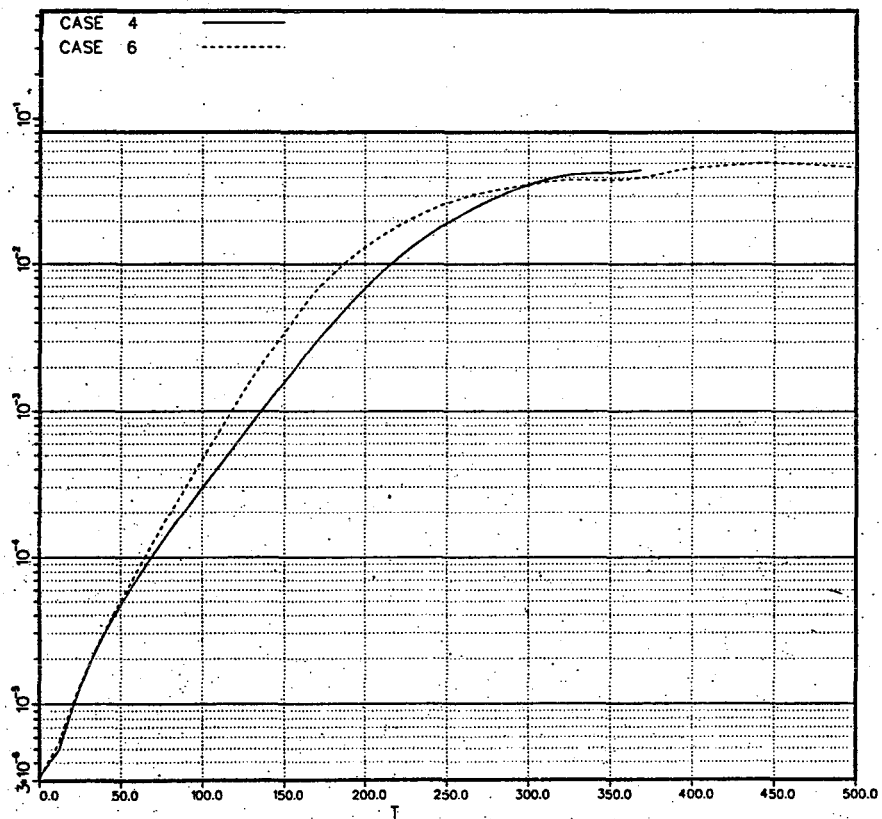


Fig. 5.5.1. Dimensionless turbulent kinetic energy at the center of the layer vs. dimensionless time for low-amplitude Cases 4 and 6.

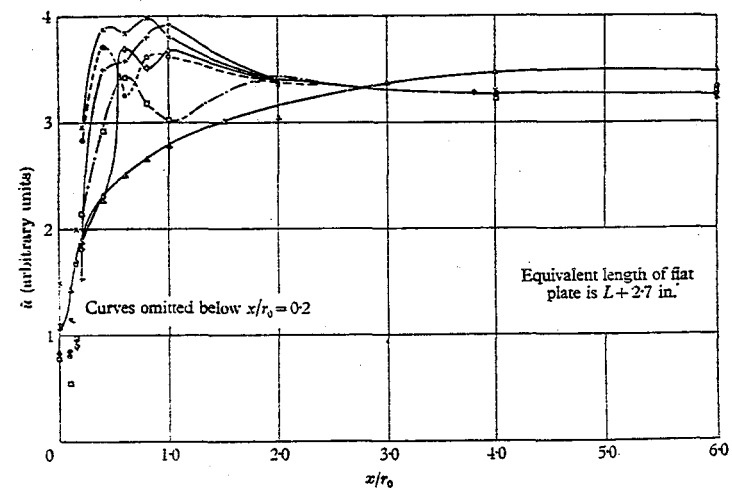


Fig. 5.5.2 R.M.S. values of the streamwise velocity fluctuation at the center of the mixing layer versus x/r_0 . An $x/r_0 = 6$ corresponds to T between 600 and 1200, depending on the initial boundary layer.

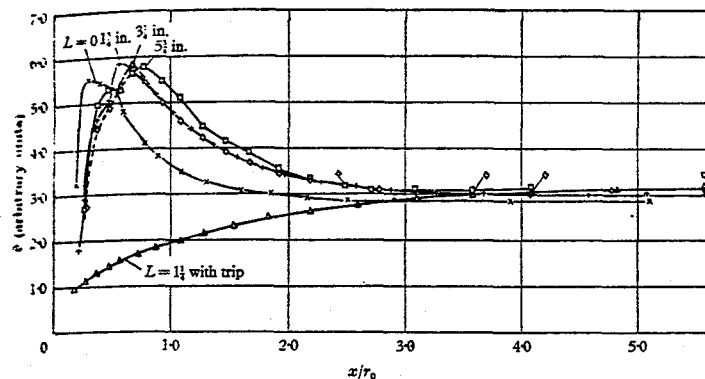


Fig. 5.5.3 R.M.S. values of the gradient velocity fluctuation at the center of the mixing layer versus x/r_0 . See caption of Fig. 5.2.2.

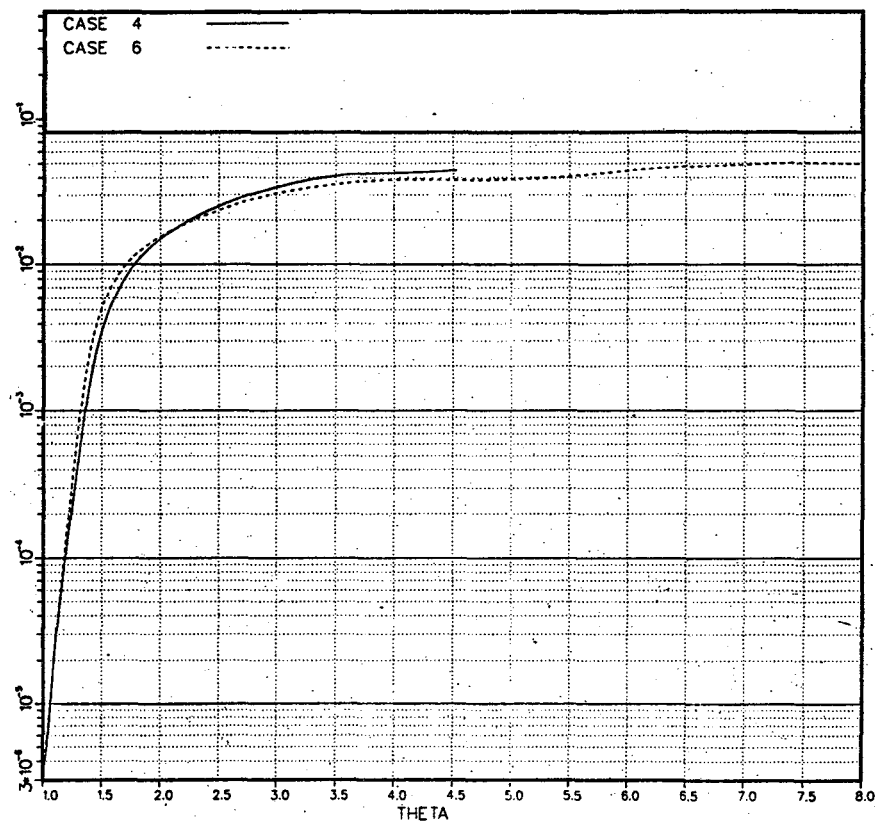


Fig. 5.5.4. Dimensionless turbulent kinetic energy at the center of the layer vs. normalized momentum thickness for low-amplitude Cases 4 and 6.

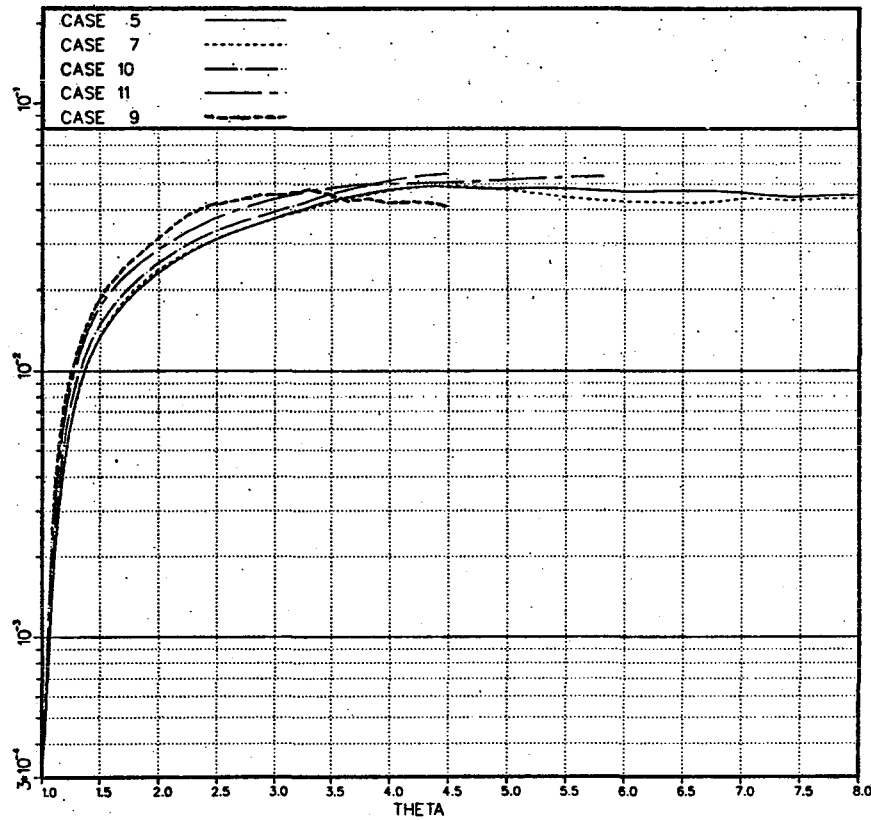


Fig. 5.5.5. Dimensionless turbulent kinetic energy at the center of the layer vs. normalized momentum thickness for medium-amplitude Cases 5, 7, 9, 10, and 11.

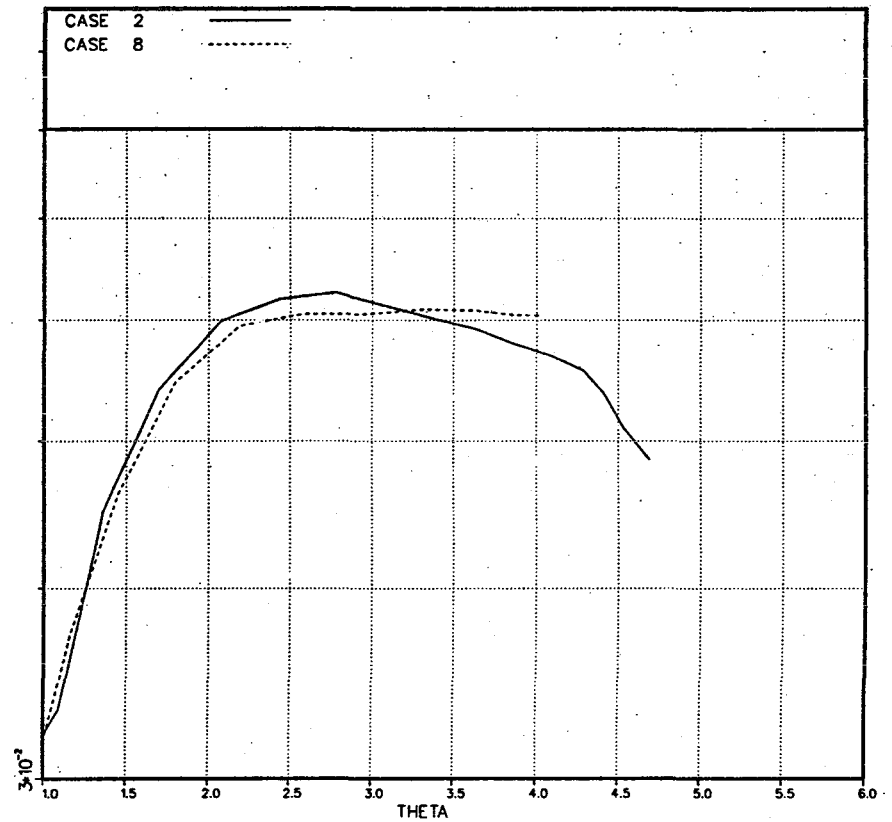


Fig. 5.5.6. Dimensionless turbulent kinetic energy at the center of the layer vs. normalized momentum thickness for high-amplitude Cases 2 and 8.

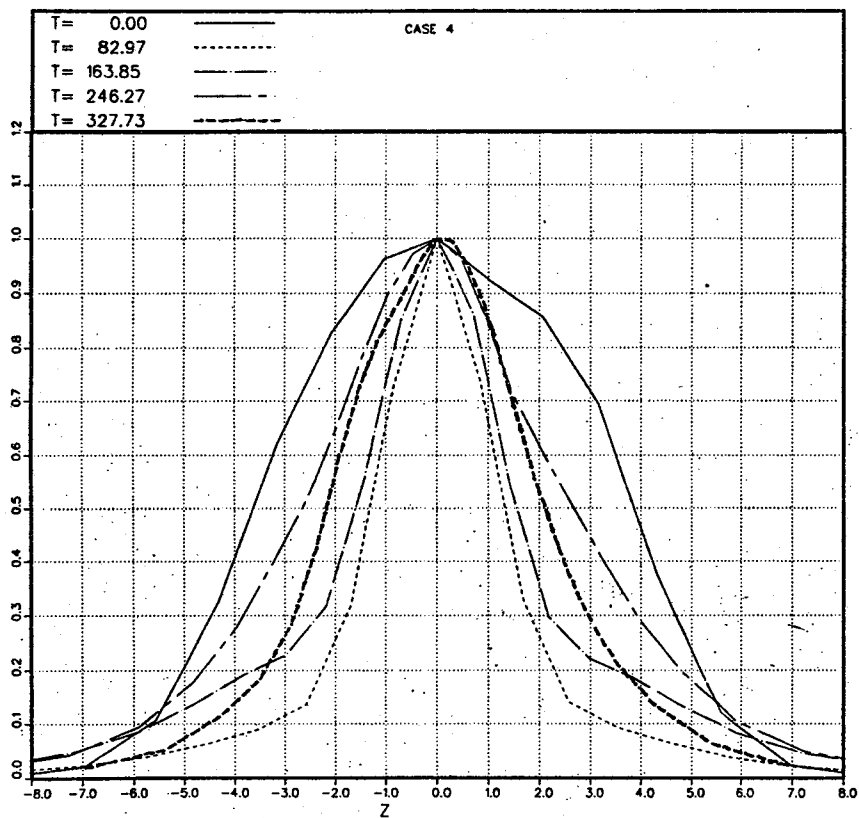


Fig. 5.6.1. Normalized turbulent kinetic energy profiles for Case 4.

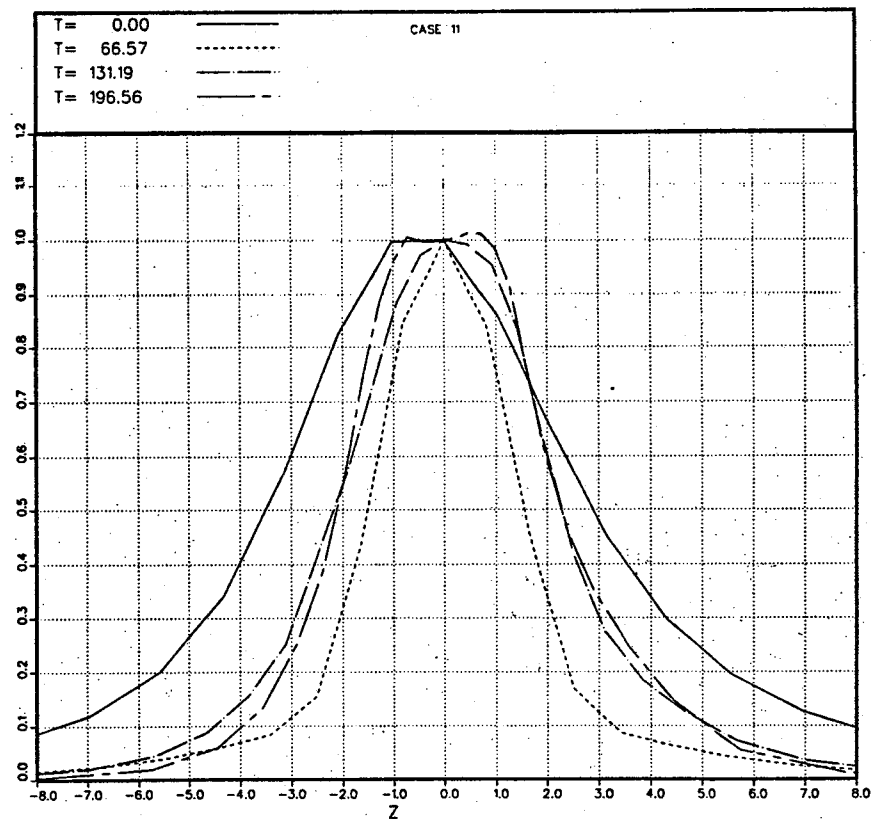


Fig. 5.6.2. Normalized turbulent kinetic energy profiles for Case 11.

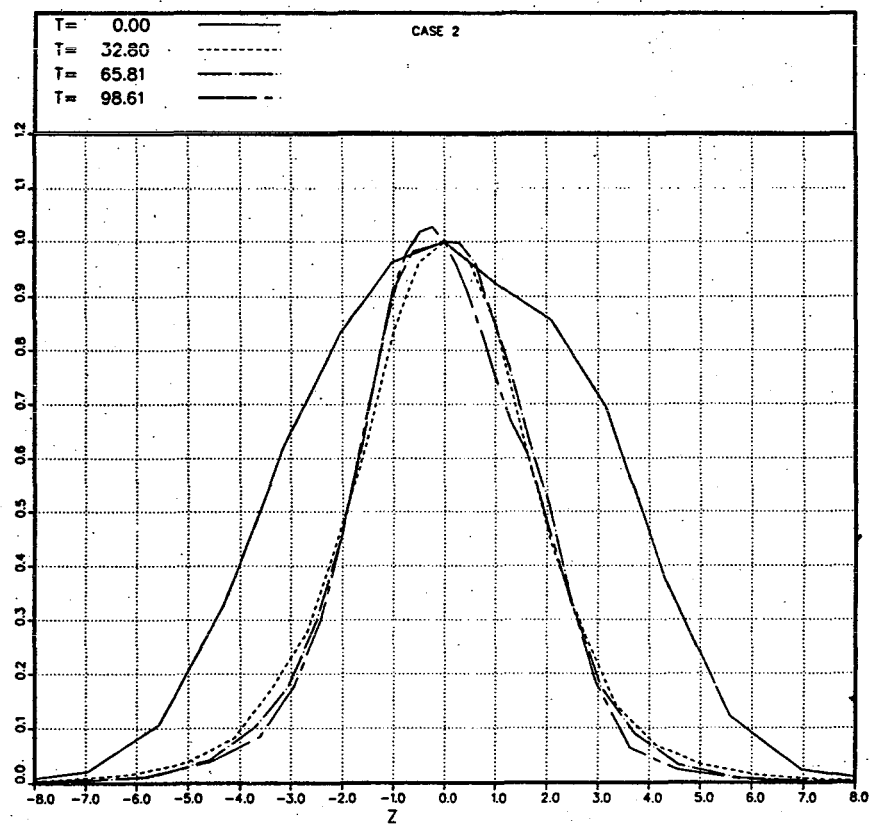


Fig. 5.6.3. Normalized turbulent kinetic energy profiles for Case 2.

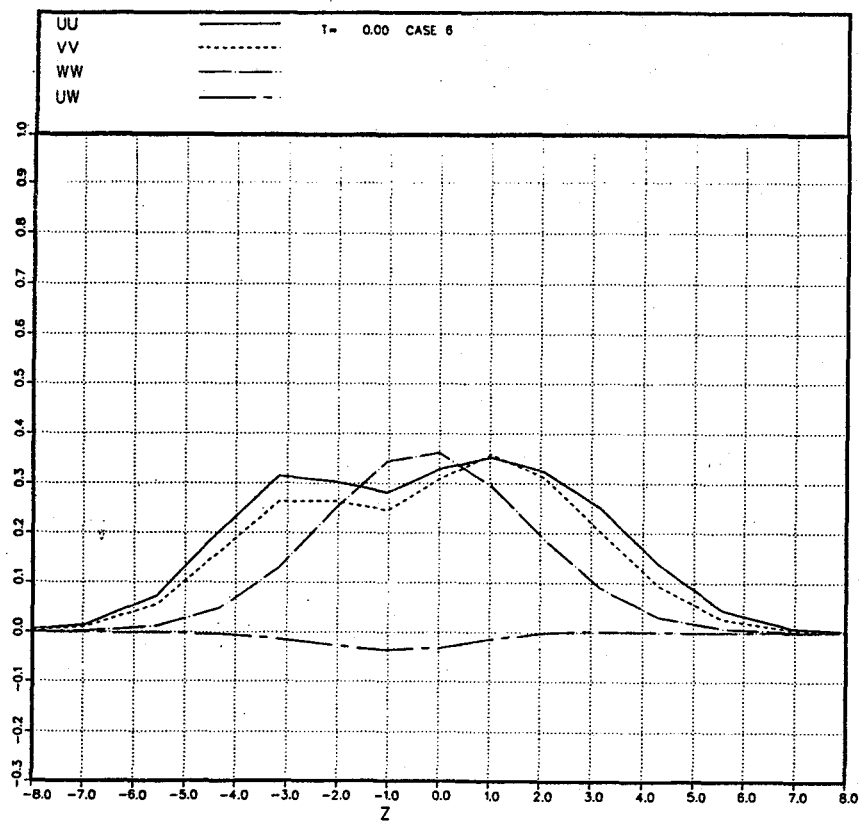


Fig. 5.7.1. Normalized Reynolds stress tensor profiles for Case 6 at $T = 0$.

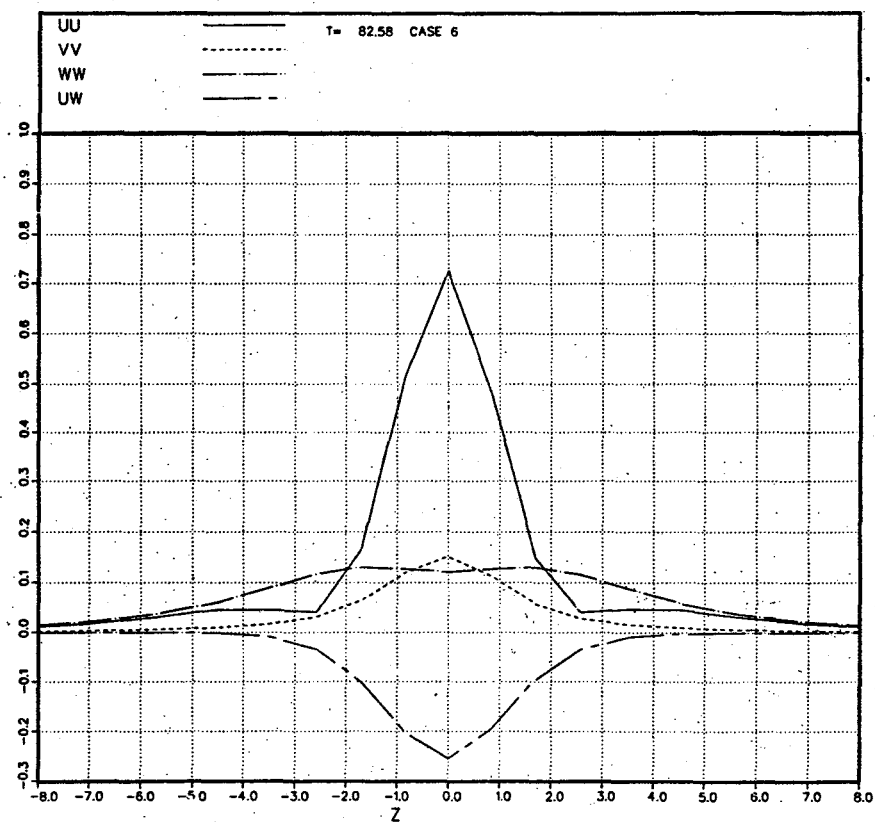


Fig. 5.7.2. Normalized Reynolds stress tensor profiles for Case 6 at $T = 83$.

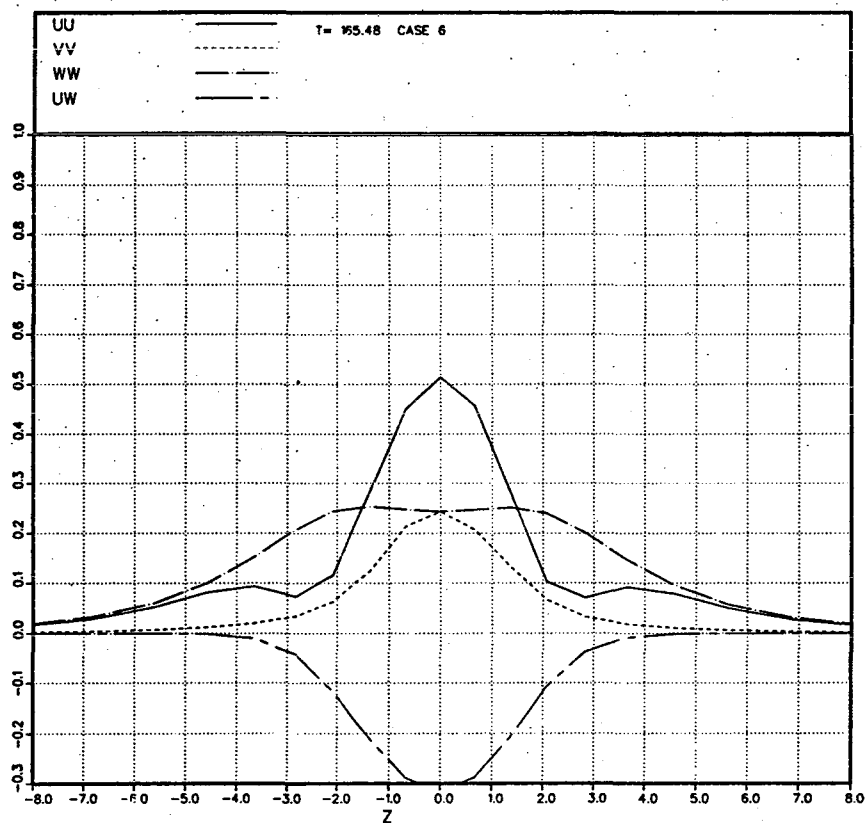


Fig. 5.7.3. Normalized Reynolds stress tensor profiles for Case 6 at $T = 165$.

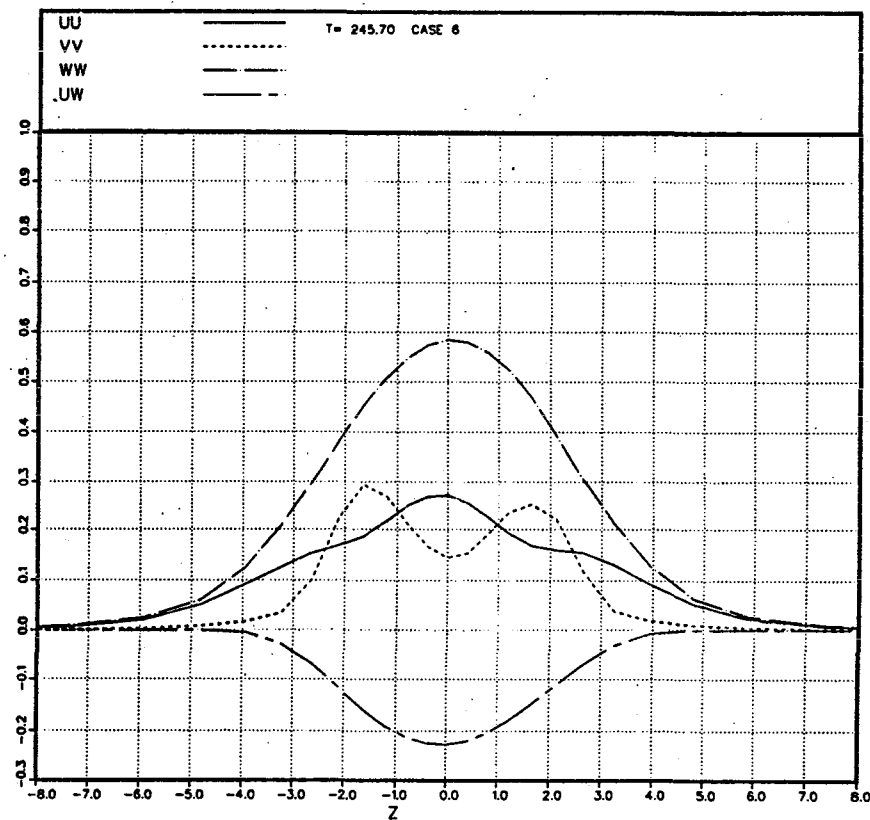


Fig. 5.7.4. Normalized Reynolds stress tensor profiles for Case 6 at $T = 246$.

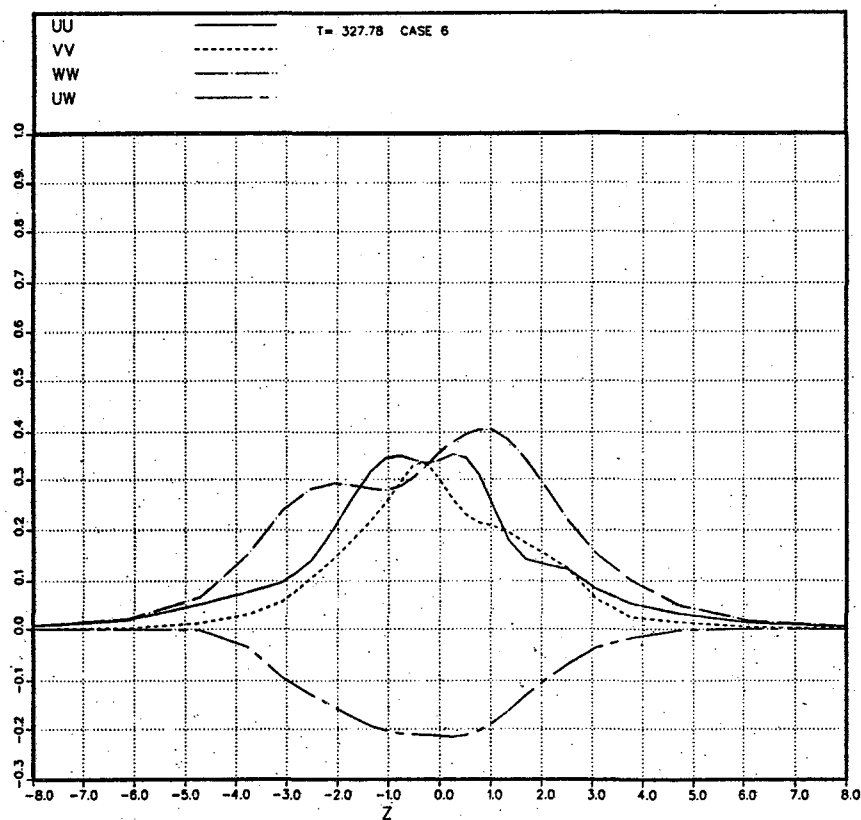


Fig. 5.7.5. Normalized Reynolds stress tensor profiles for Case 6 at $T = 328$.

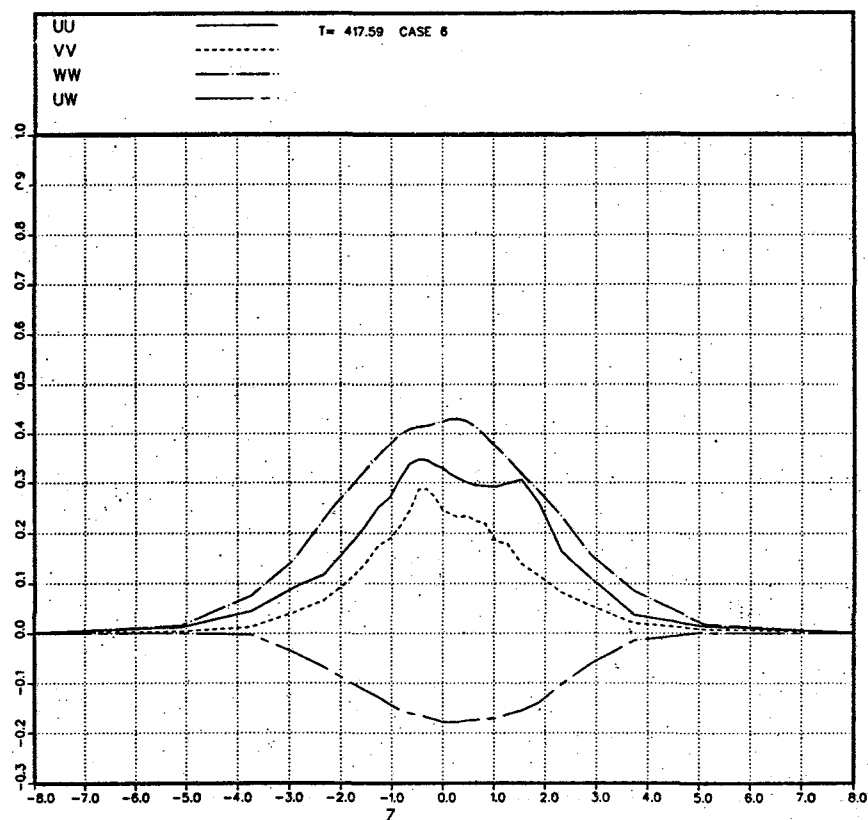


Fig. 5.7.6. Normalized Reynolds stress tensor profiles for Case 6 at $T = 418$.

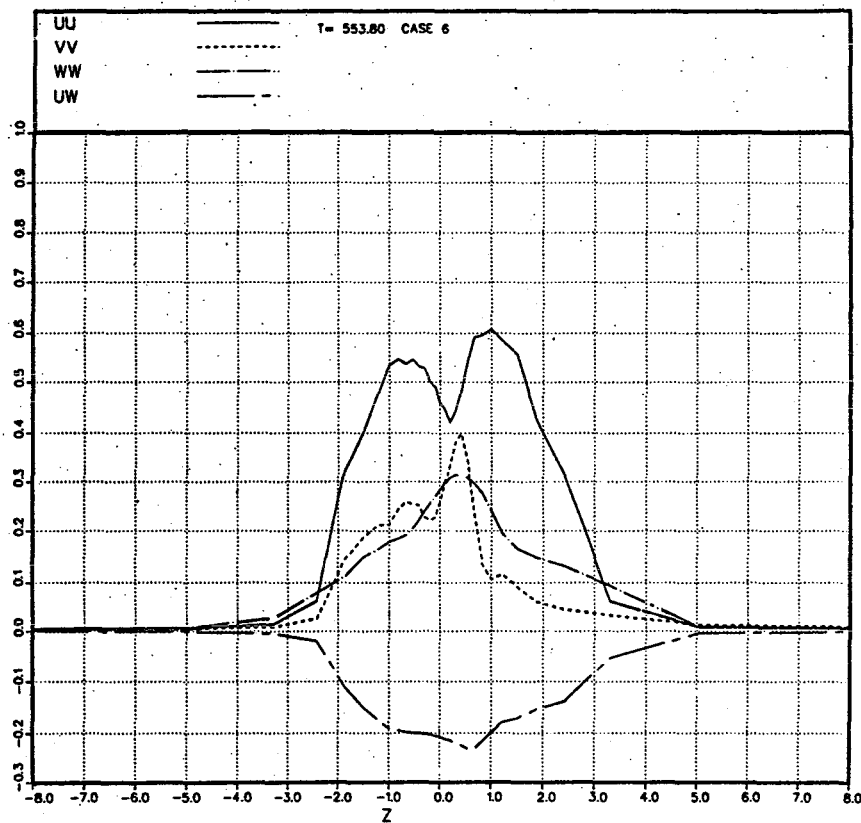


Fig. 5.7.7. Normalized Reynolds stress tensor profiles for Case 6 at $T = 554$.

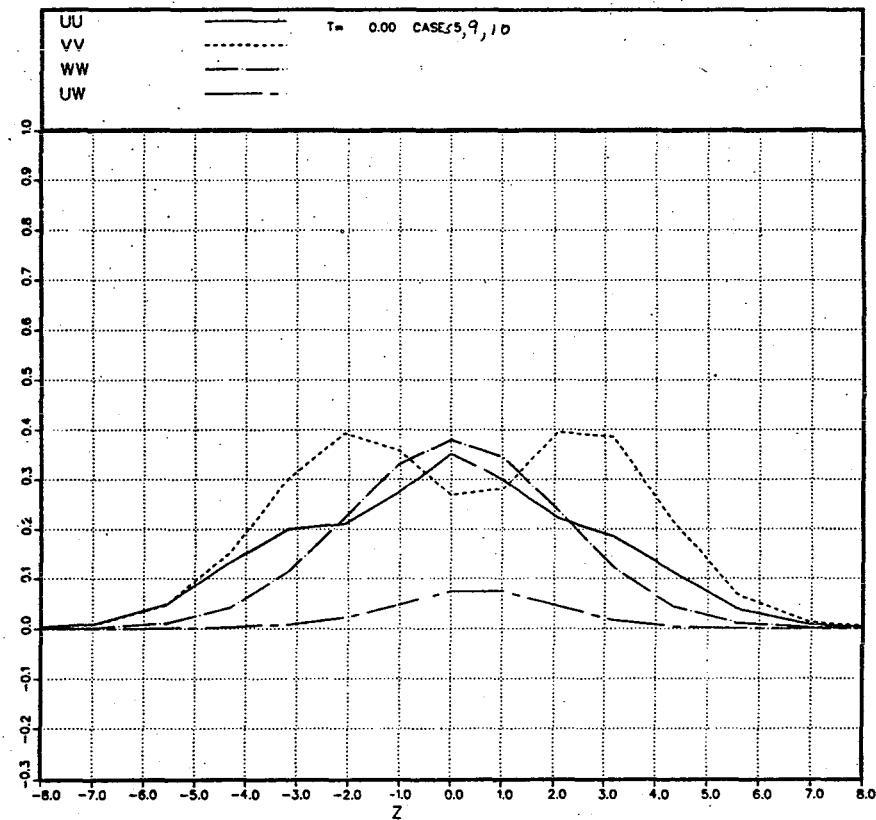


Fig. 5.7.8. Normalized Reynolds stress tensor profiles for Cases 5, 9, and 10 at $T = 0.0$.

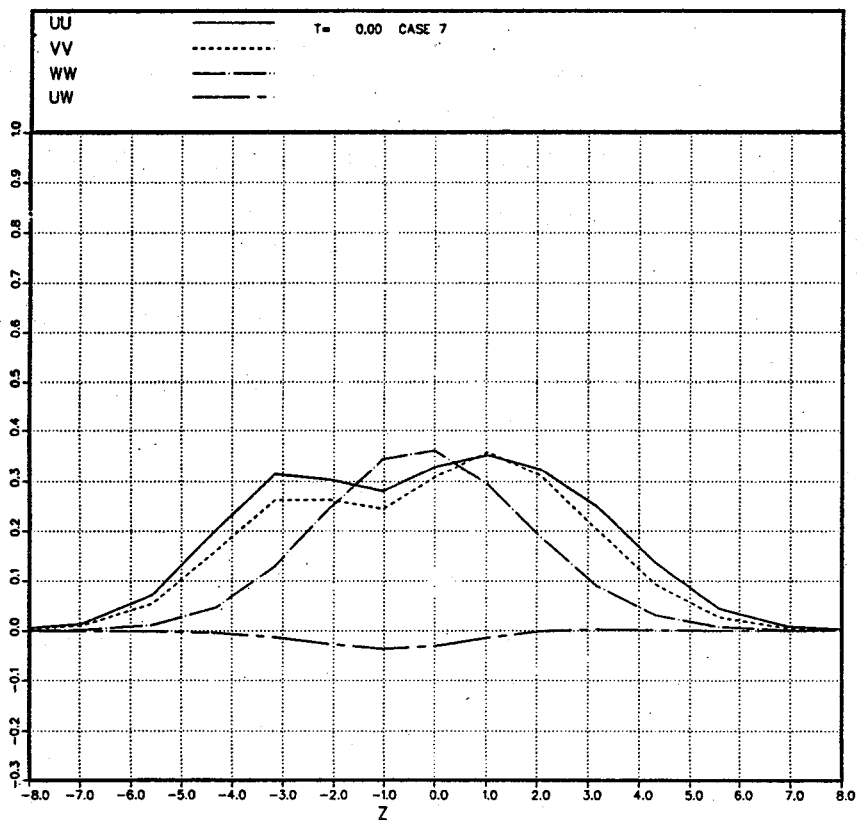


Fig. 5.7.9. Normalized Reynolds stress tensor profiles for Case 7 at $T = 0.0$.

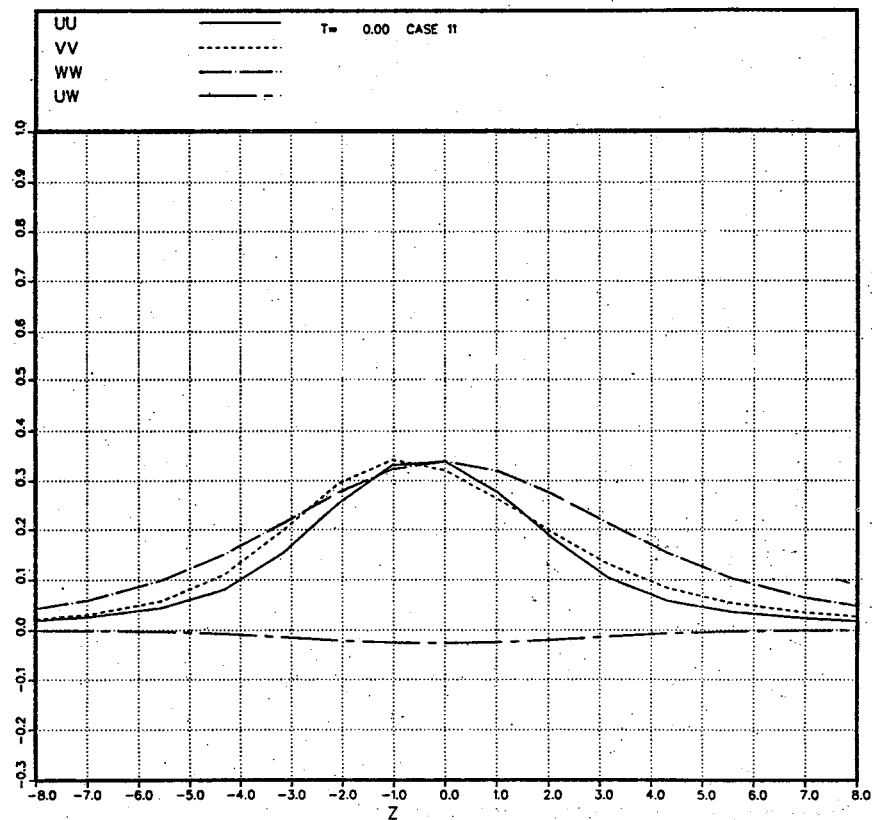


Fig. 5.7.10. Normalized Reynolds stress tensor profiles for Case 11 at $T = 0.0$.

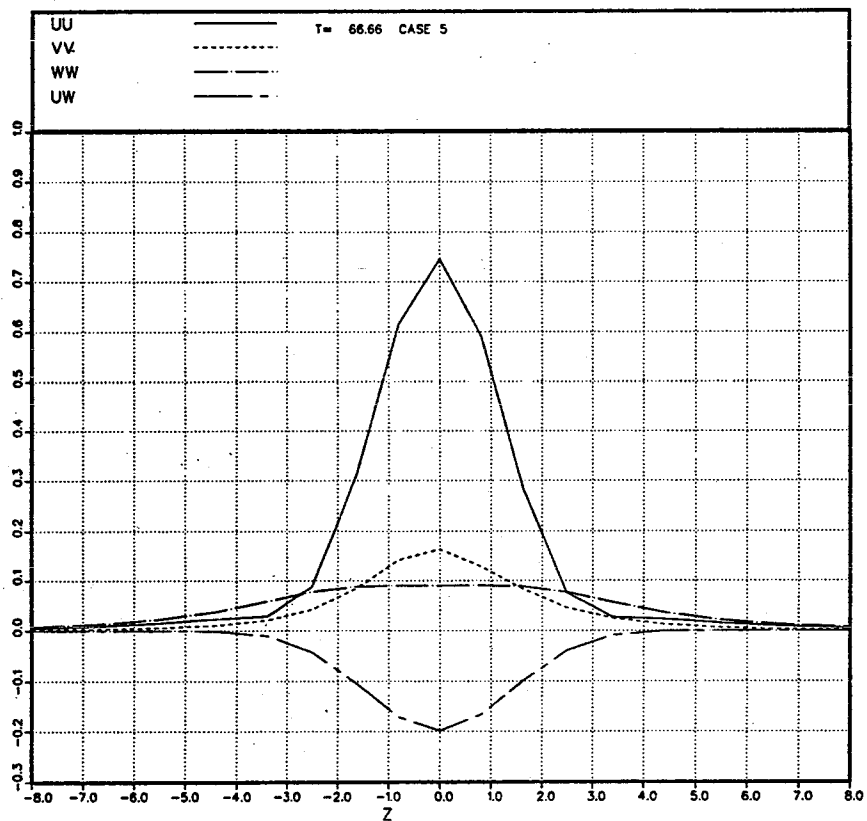


Fig. 5.7.11. Normalized Reynolds stress tensor profiles for Case 5 at $T = 67$.

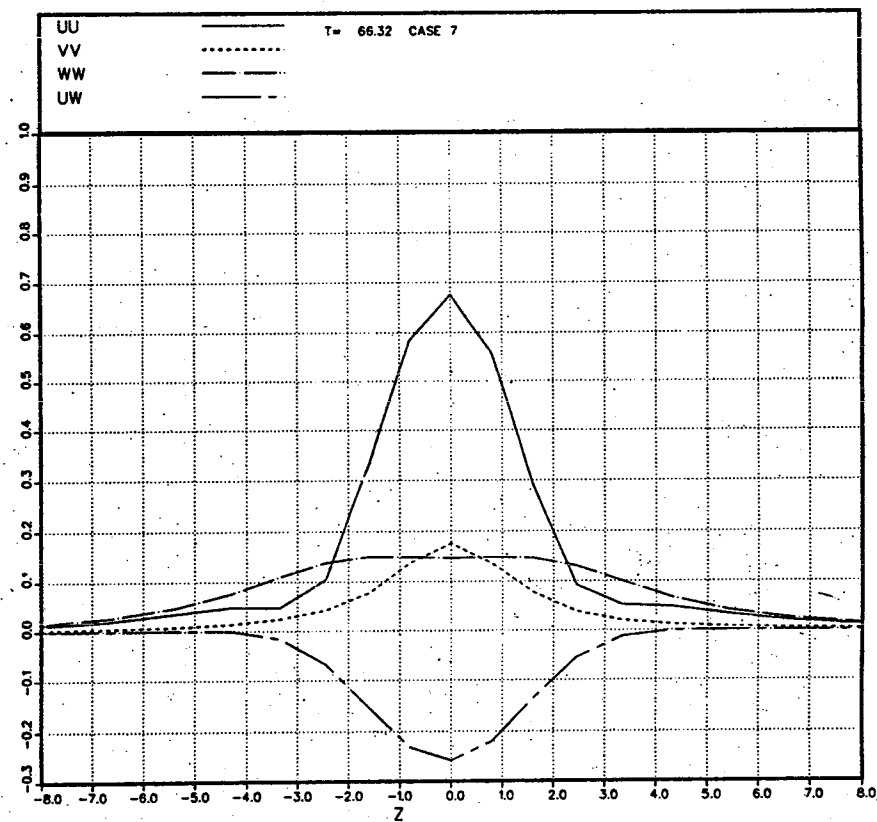


Fig. 5.7.12. Normalized Reynolds stress tensor profiles for Case 7 at $T = 66$.

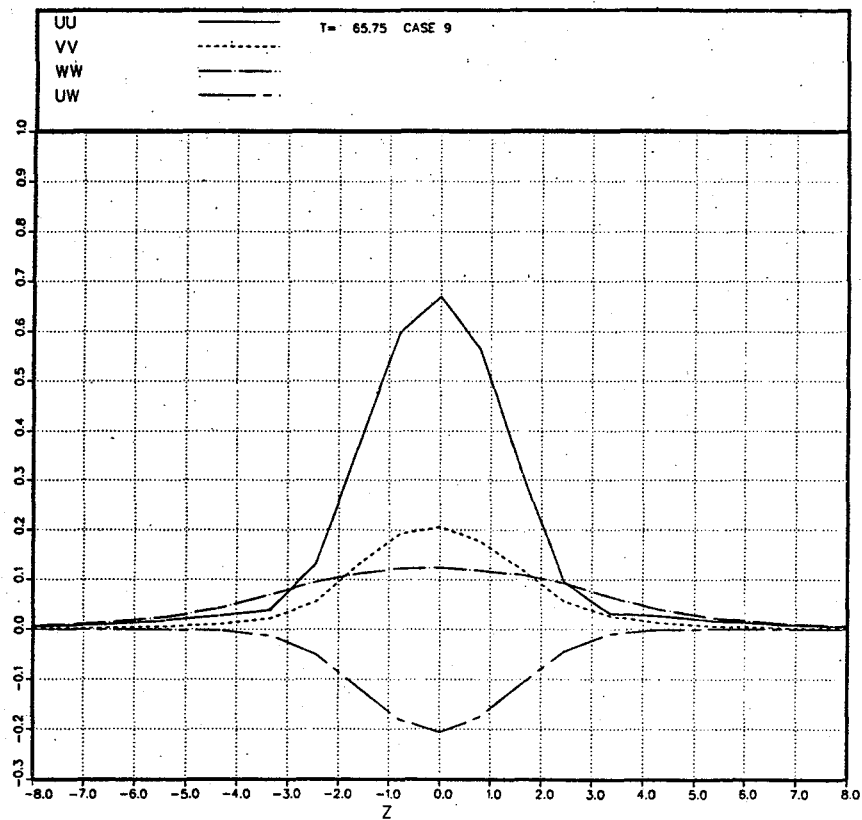


Fig. 5.7.13. Normalized Reynolds stress tensor profiles for Case 9 at $T = 66$.

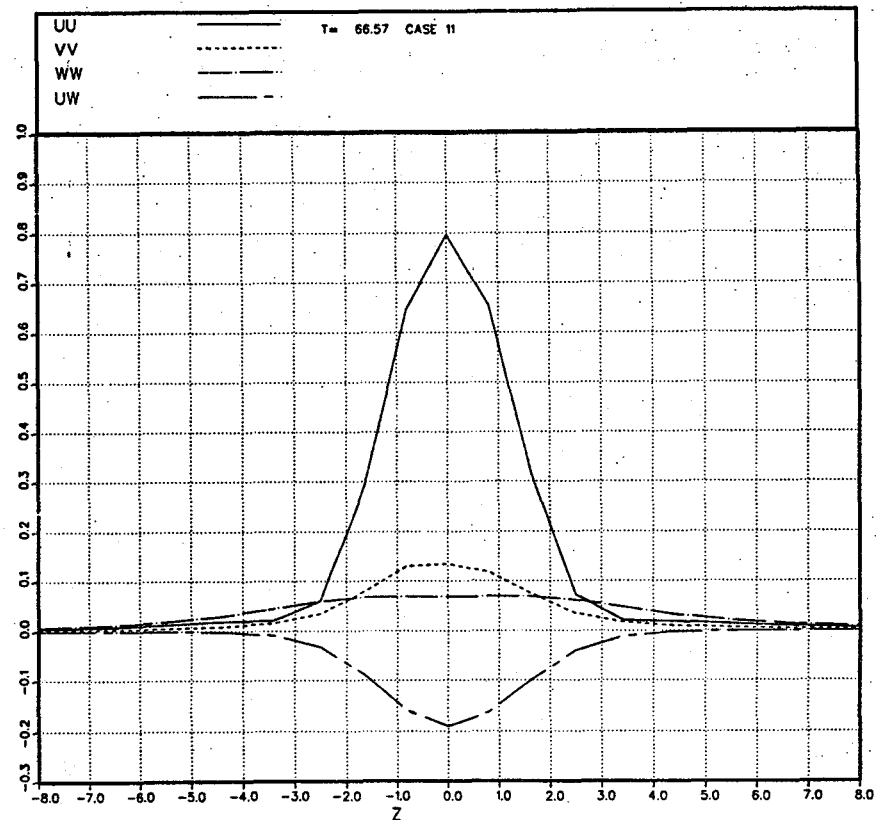


Fig. 5.7.14. Normalized Reynolds stress tensor profiles for Case 11 at $T = 67$.

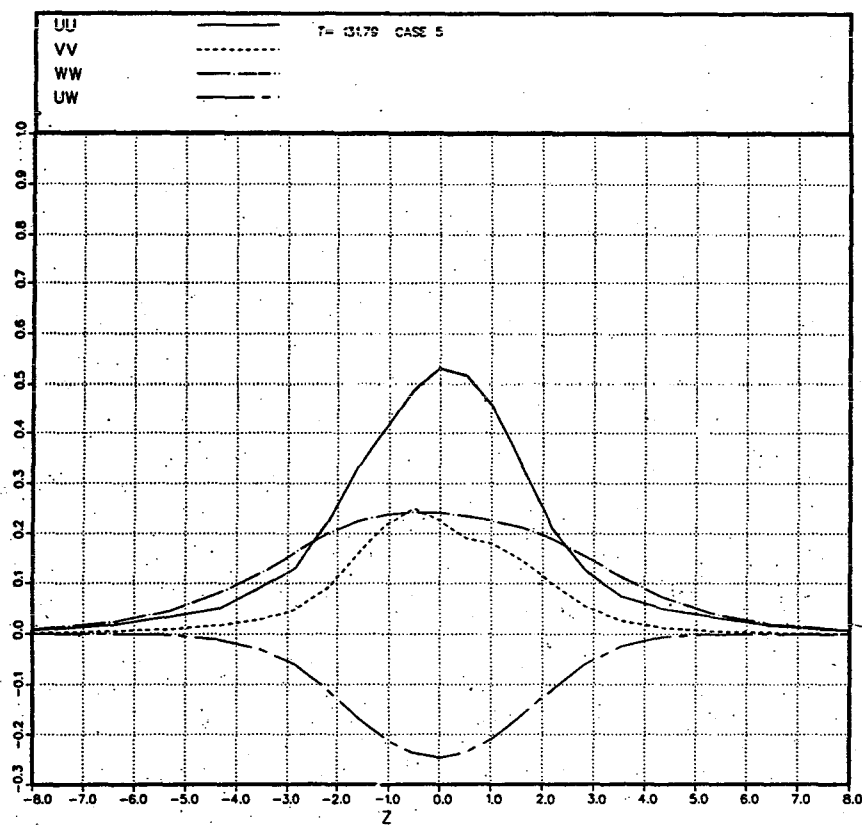


Fig. 5.7.15. Normalized Reynolds stress tensor profiles for Case 5 at $T = 132$.

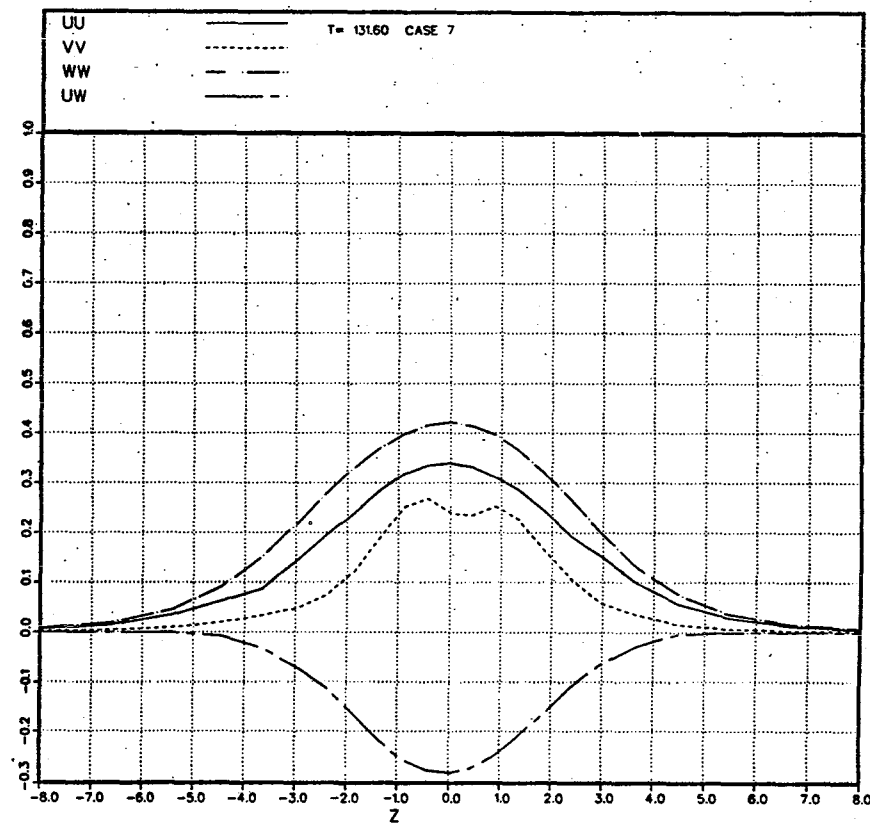


Fig. 5.7.16. Normalized Reynolds stress tensor profiles for Case 7 at $T = 132$.

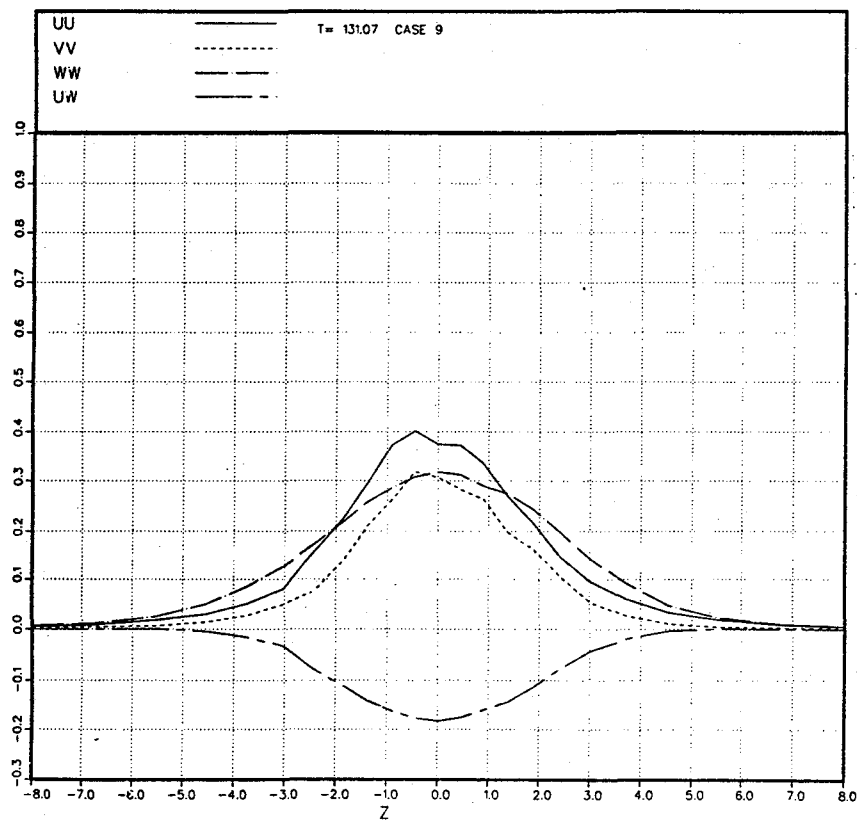


Fig. 5.7.17. Normalized Reynolds stress tensor profiles for Case 9 at $T = 131$.

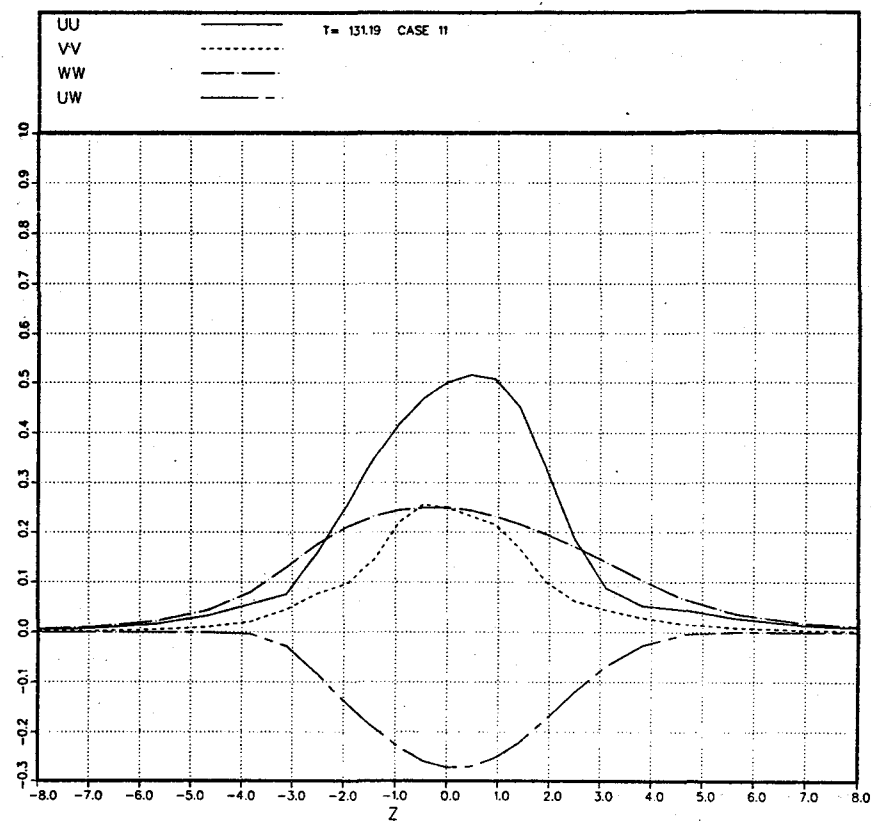


Fig. 5.7.18. Normalized Reynolds stress tensor profiles for Case 11 at $T = 131$.

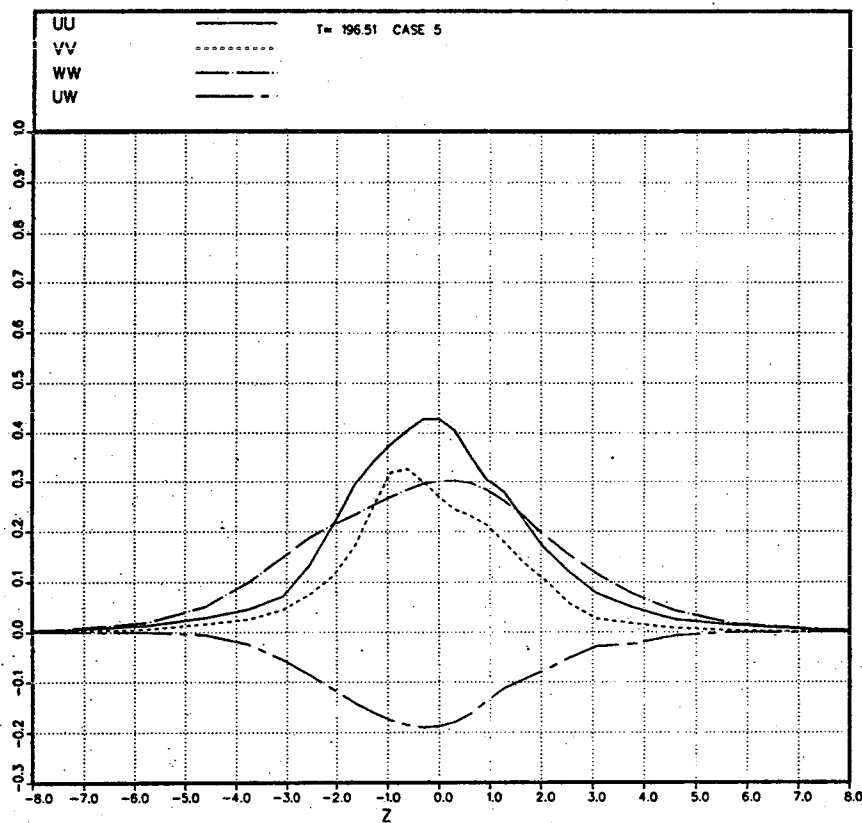


Fig. 5.7.19. Normalized Reynolds stress tensor profiles for Case 5 at $T = 197$.

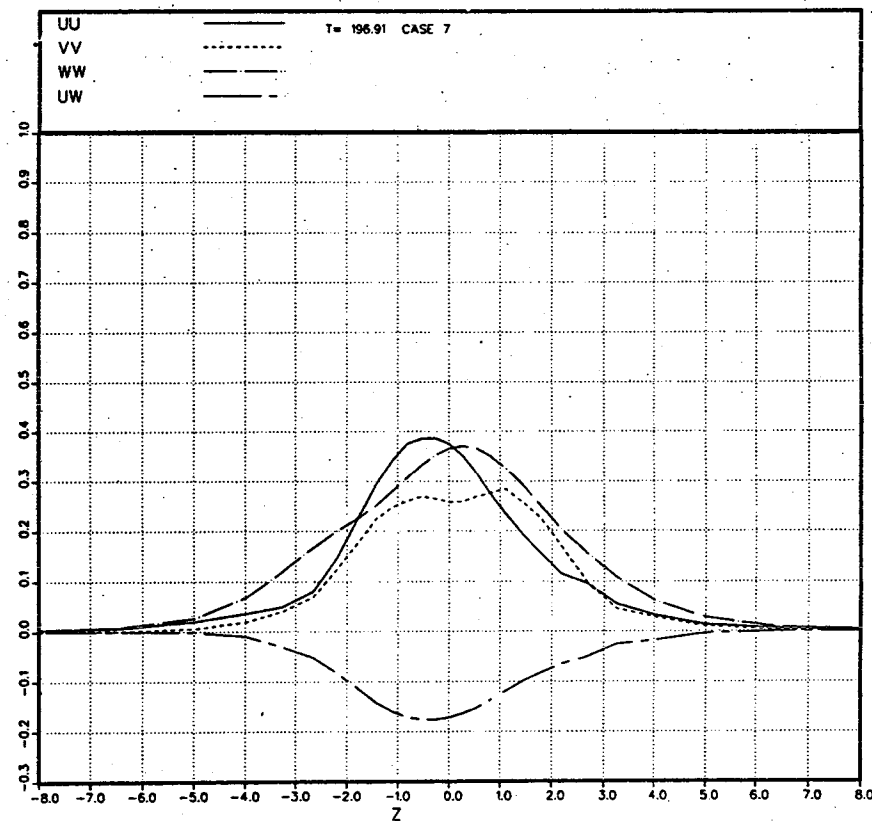


Fig. 5.7.20. Normalized Reynolds stress tensor profiles for Case 7 at $T = 197$.

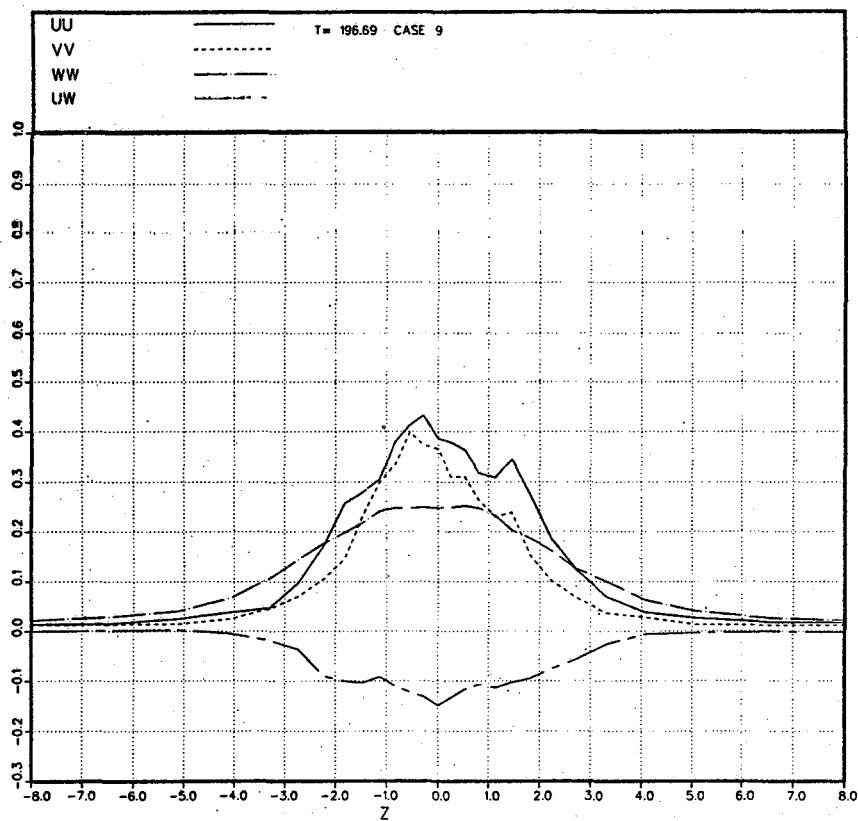


Fig. 5.7.21. Normalized Reynolds stress tensor profiles for Case 9 at $T = 197$.

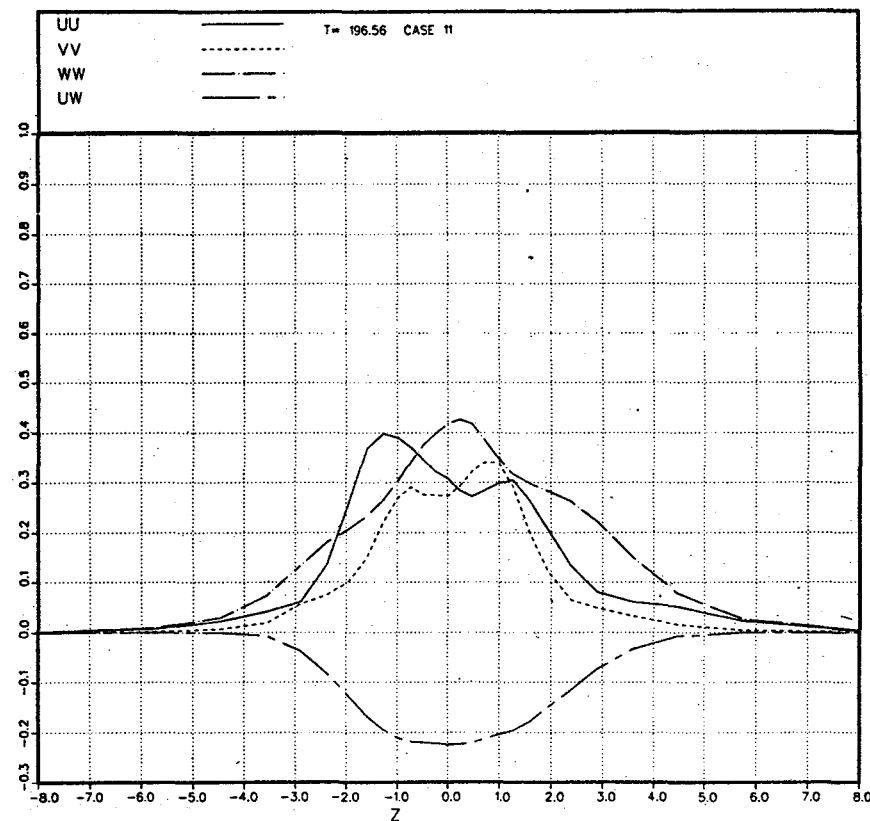


Fig. 5.7.22. Normalized Reynolds stress tensor profiles for Case 11 at $T = 197$.

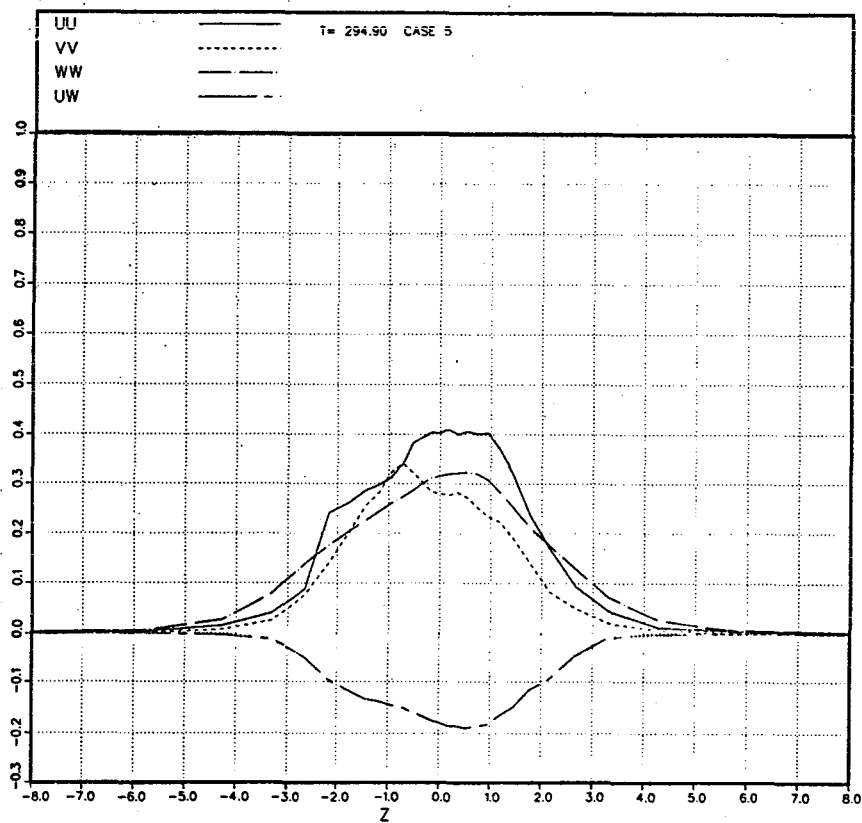


Fig. 5.7.23. Normalized Reynolds stress tensor profiles for Case 5 at $T = 295$.

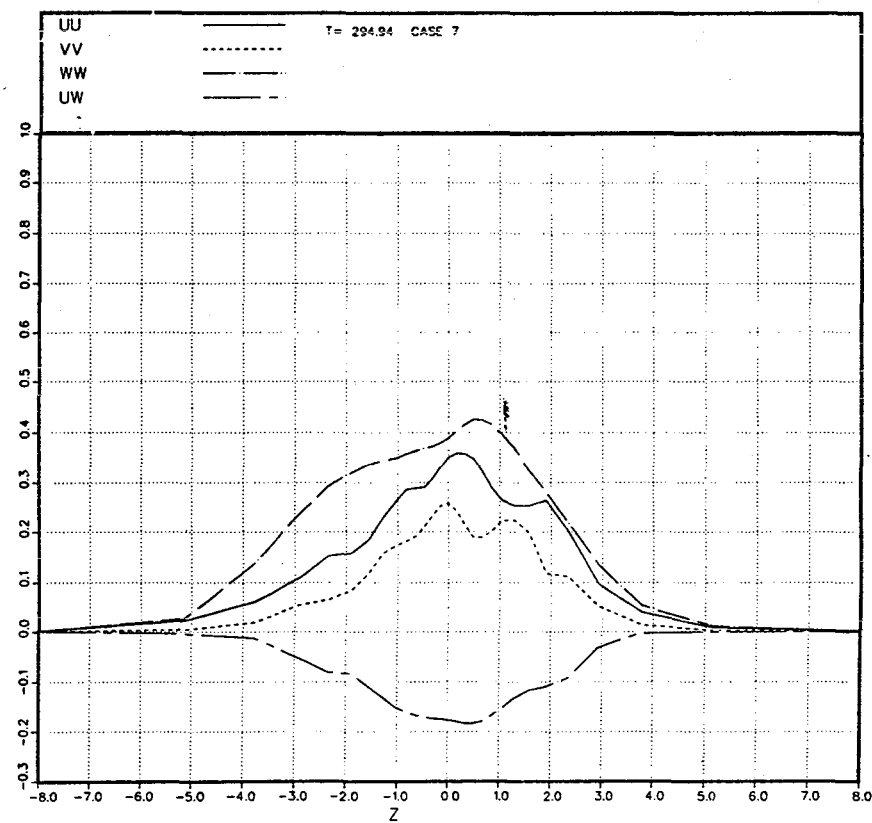


Fig. 5.7.24. Normalized Reynolds stress tensor profiles for Case 7 at $T = 295$.

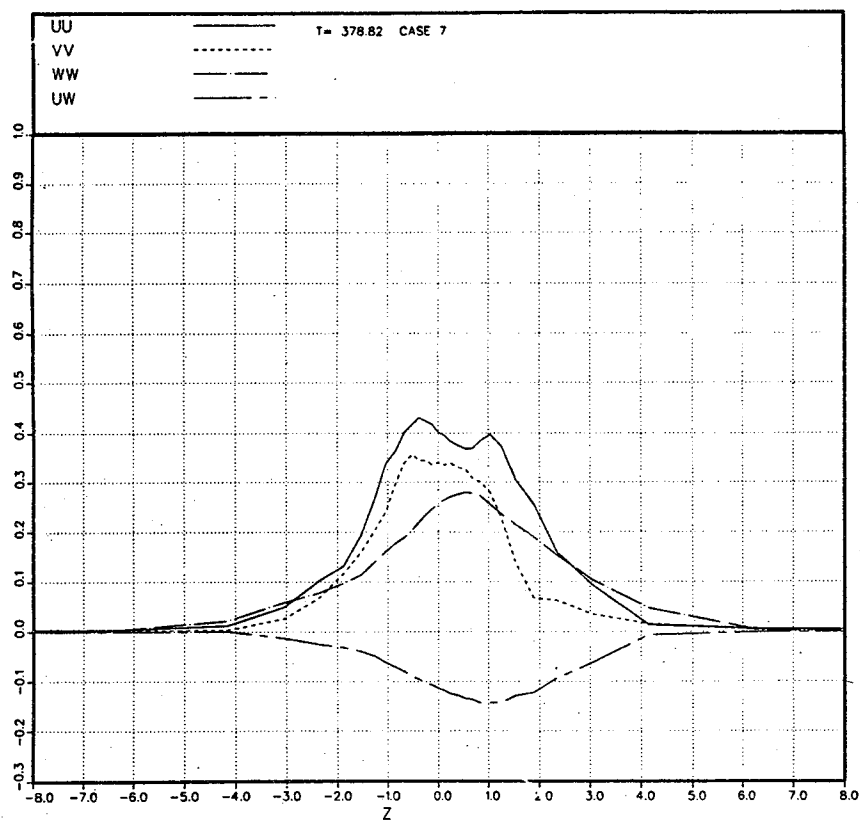


Fig. 5.7.25. Normalized Reynolds stress tensor profiles for Case 7 at $T = 379$.

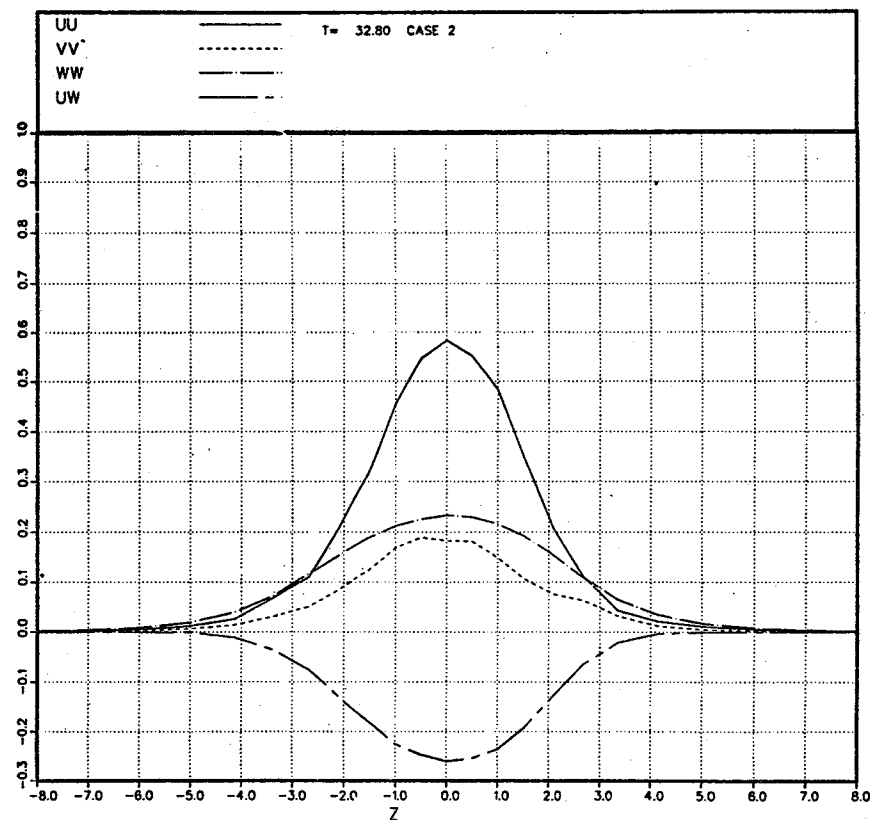


Fig. 5.7.26. Normalized Reynolds stress tensor profiles for Case 2 at $T = 33$.

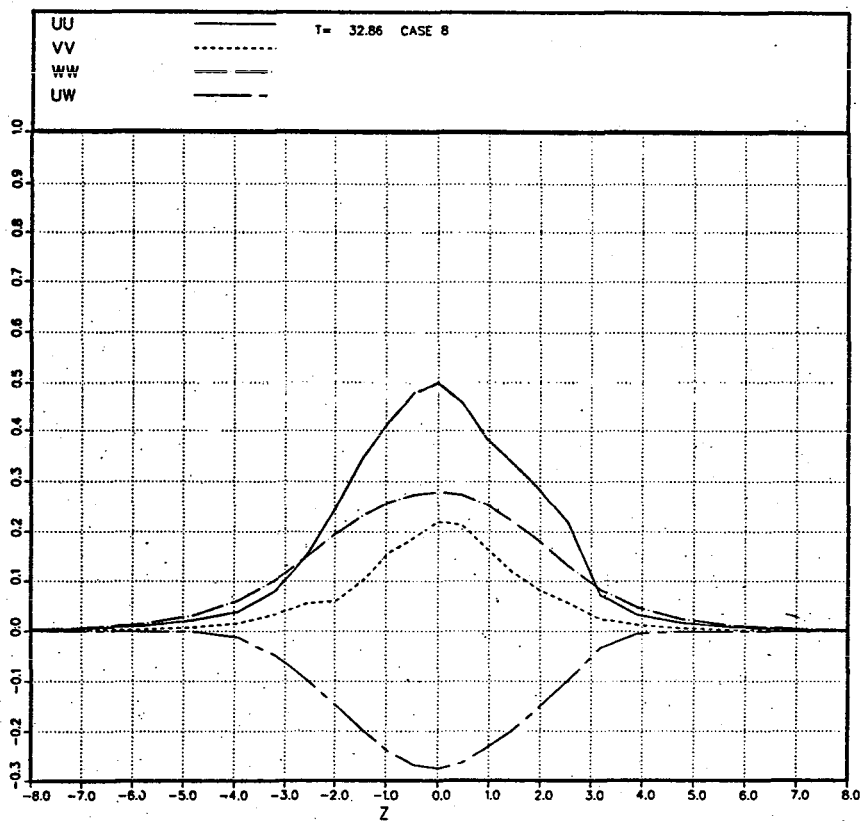


Fig. 5.7.27. Normalized Reynolds stress tensor profiles for Case 8 at $T = 33$.

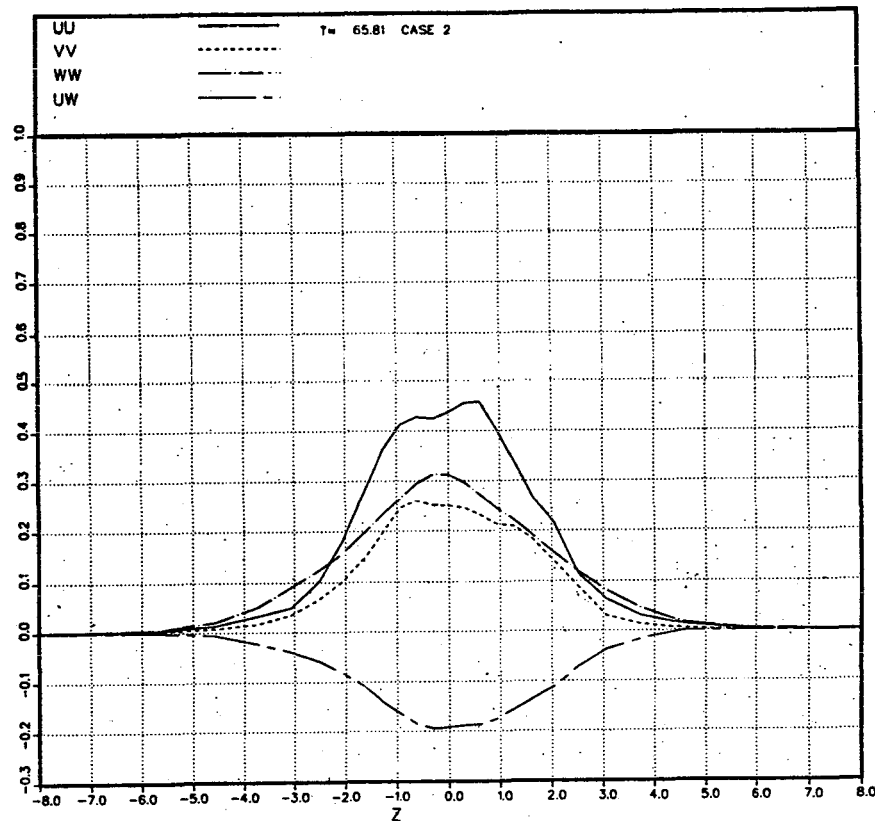


Fig. 5.7.28. Normalized Reynolds stress tensor profiles for Case 2 at $T = 66$.

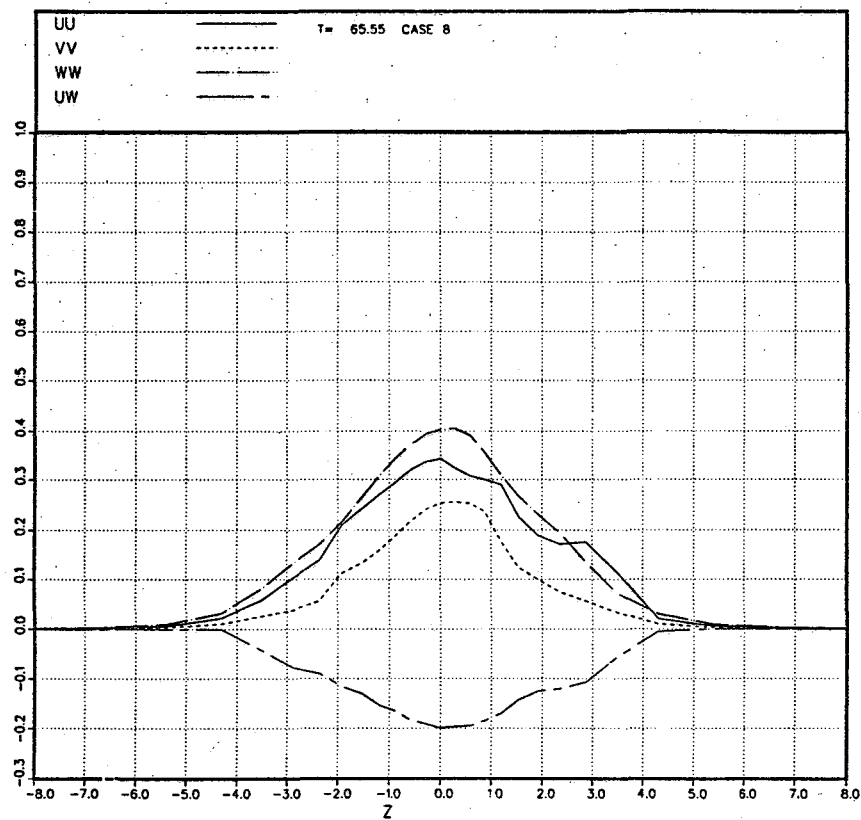


Fig. 5.7.29. Normalized Reynolds stress tensor profiles for Case 8 at $T = 66$.

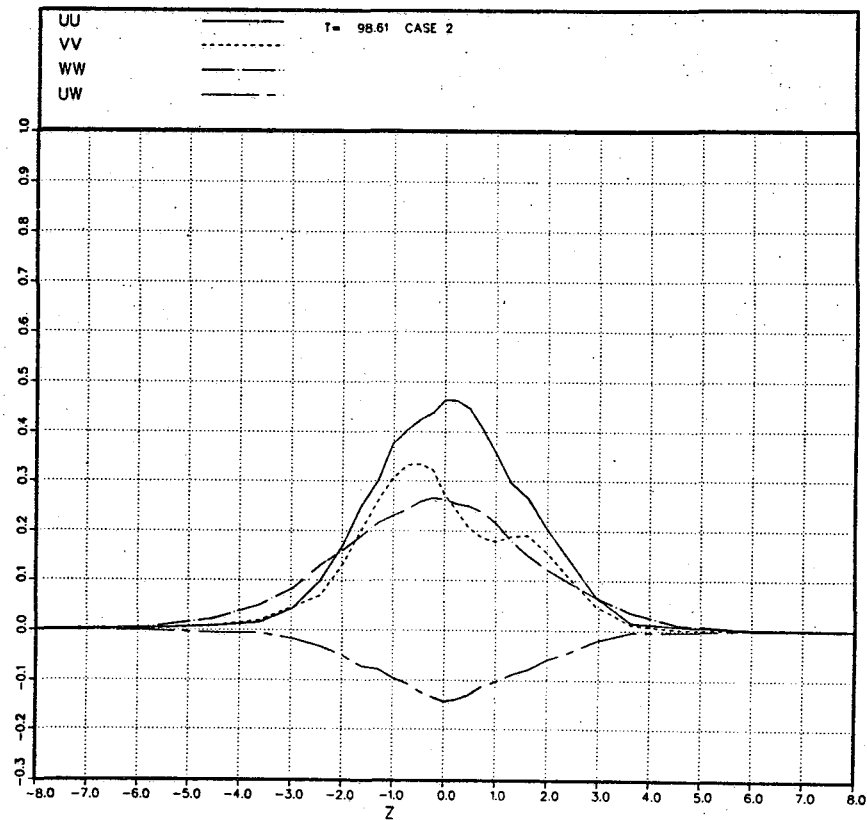


Fig. 5.7.30. Normalized Reynolds stress tensor profiles for Case 2 at $T = 99$.

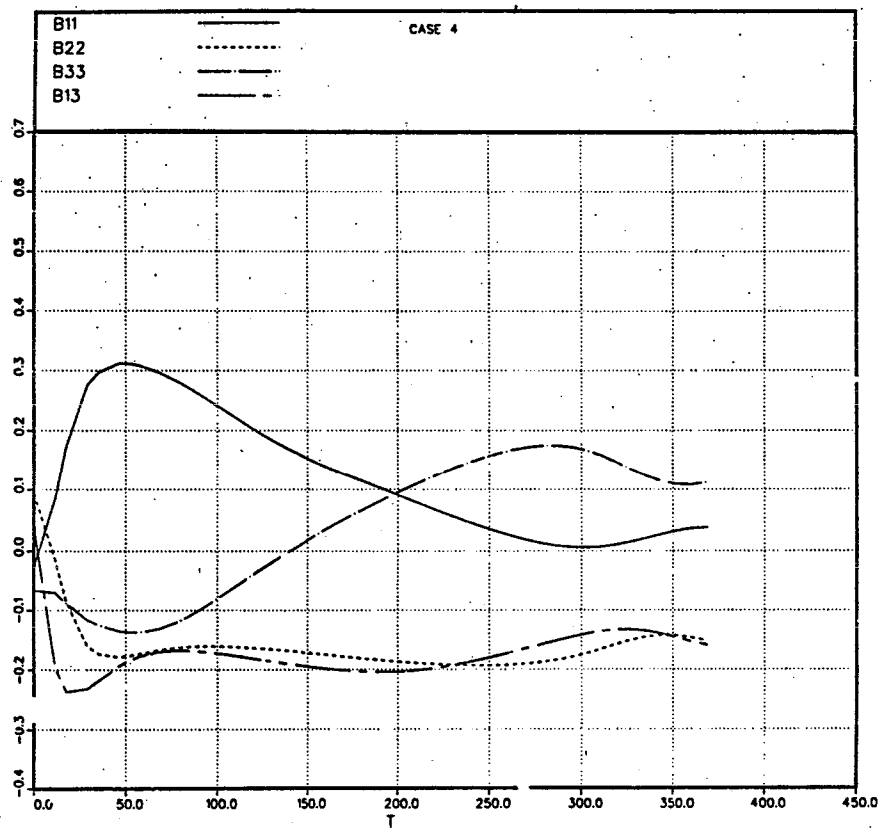


Fig. 5.8.1. Time history of the anisotropy tensor B_{ij} for Case 4.

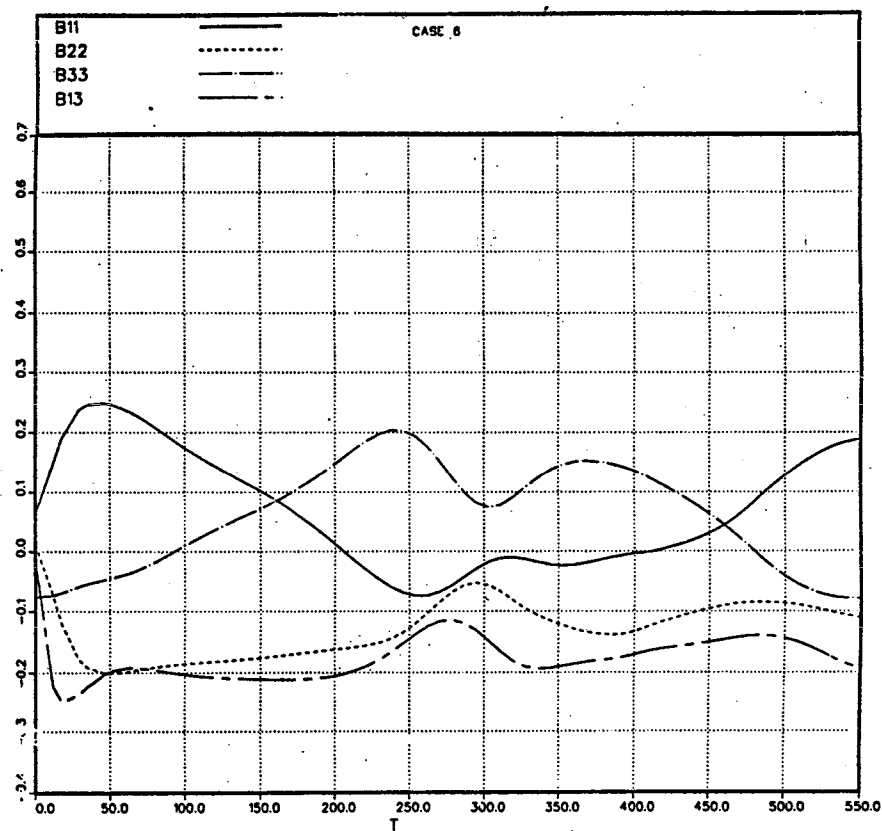


Fig. 5.8.2. Time history of the anisotropy tensor B_{ij} for Case 6.

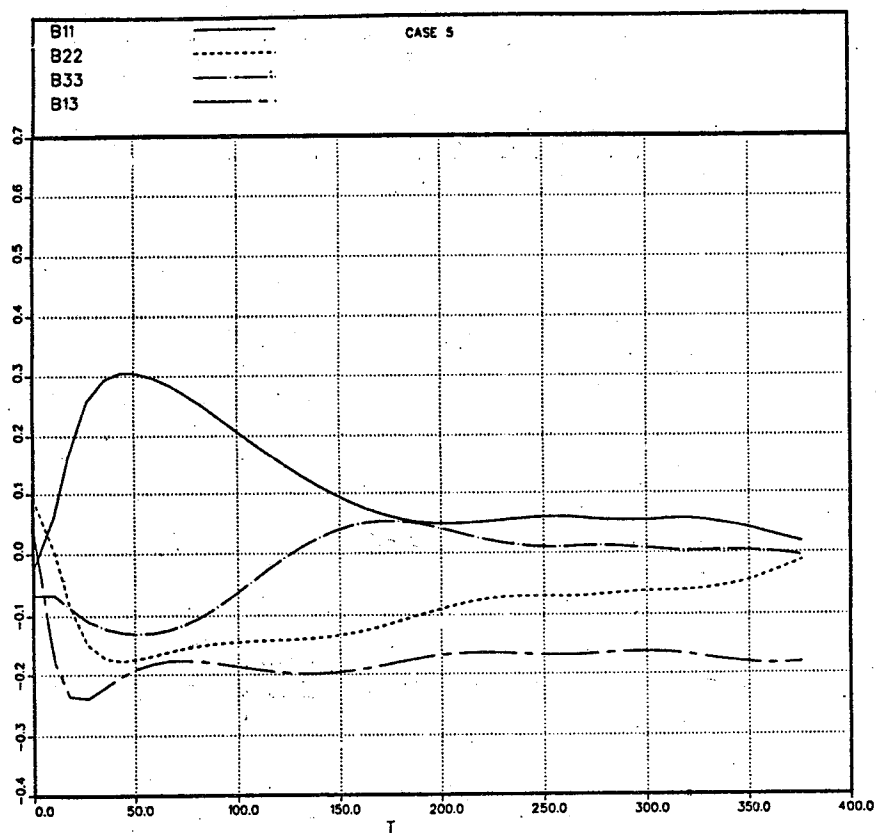


Fig. 5.8.3. Time history of the anisotropy tensor B_{ij} for Case 5.

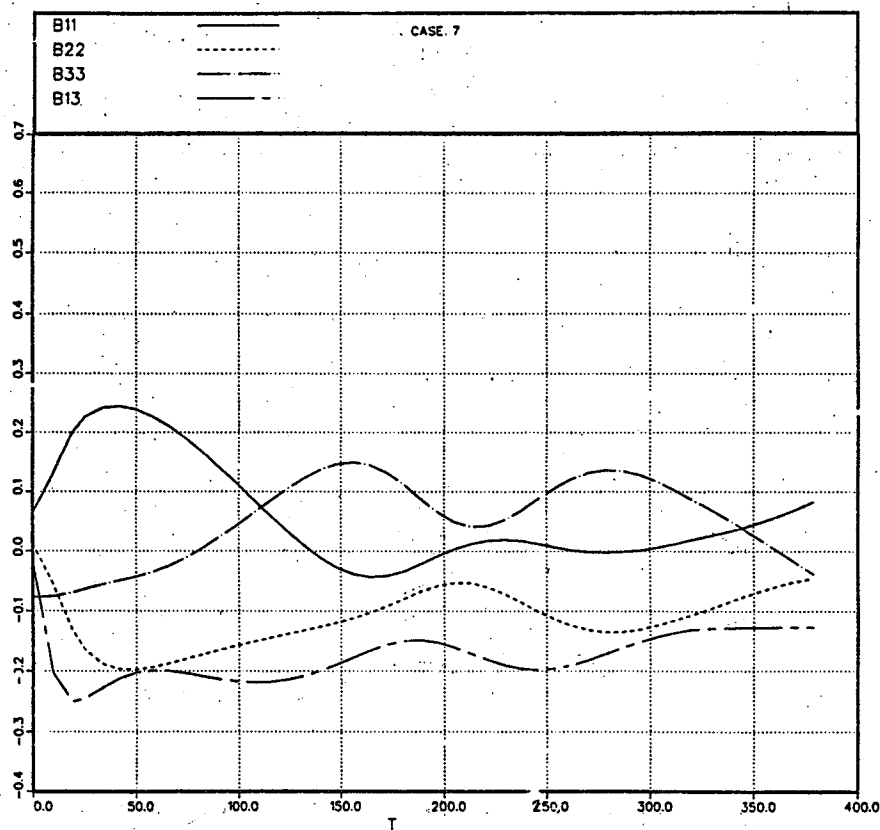


Fig. 5.8.4. Time history of the anisotropy tensor B_{ij} for Case 7.

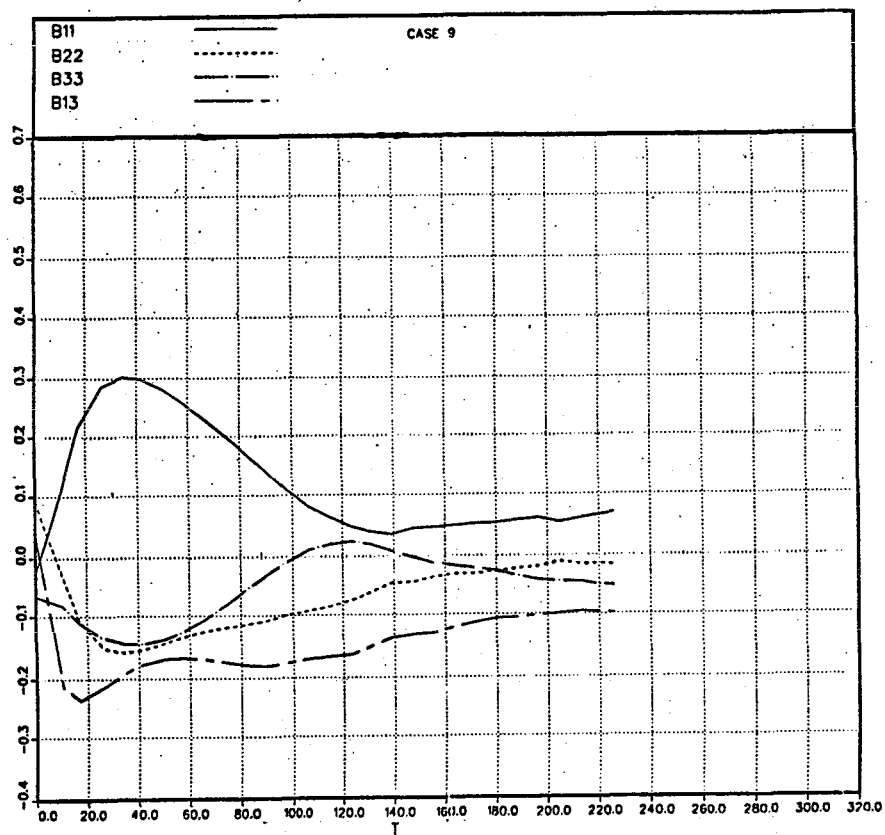


Fig. 5.8.5. Time history of the anisotropy tensor B_{ij} for Case 9.

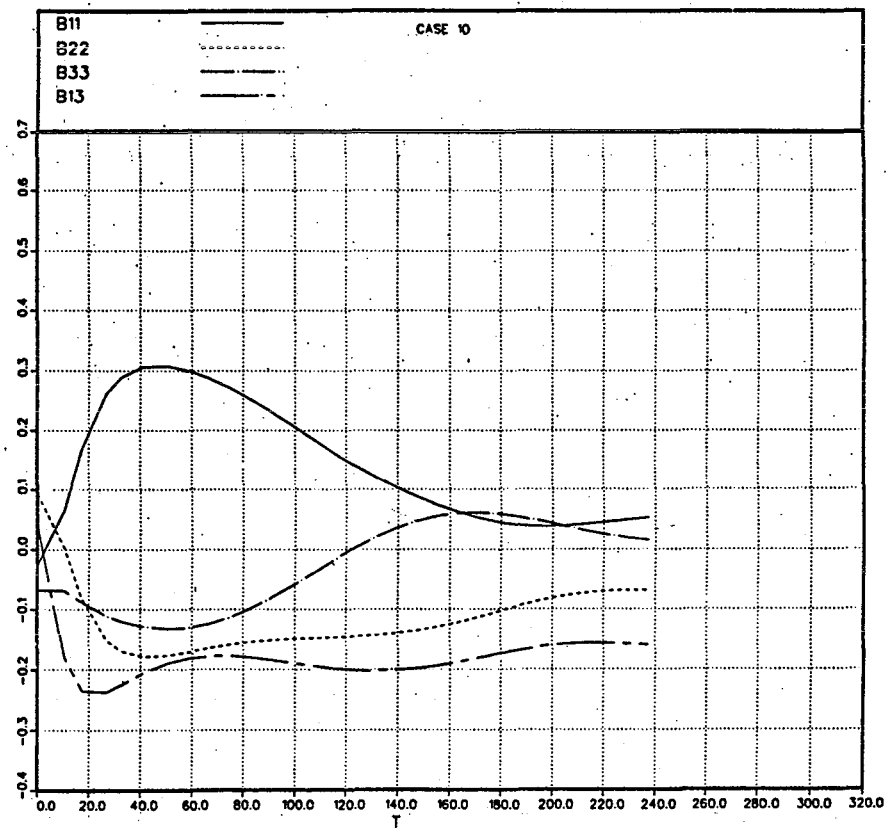


Fig. 5.8.6. Time history of the anisotropy tensor B_{ij} for Case 10.

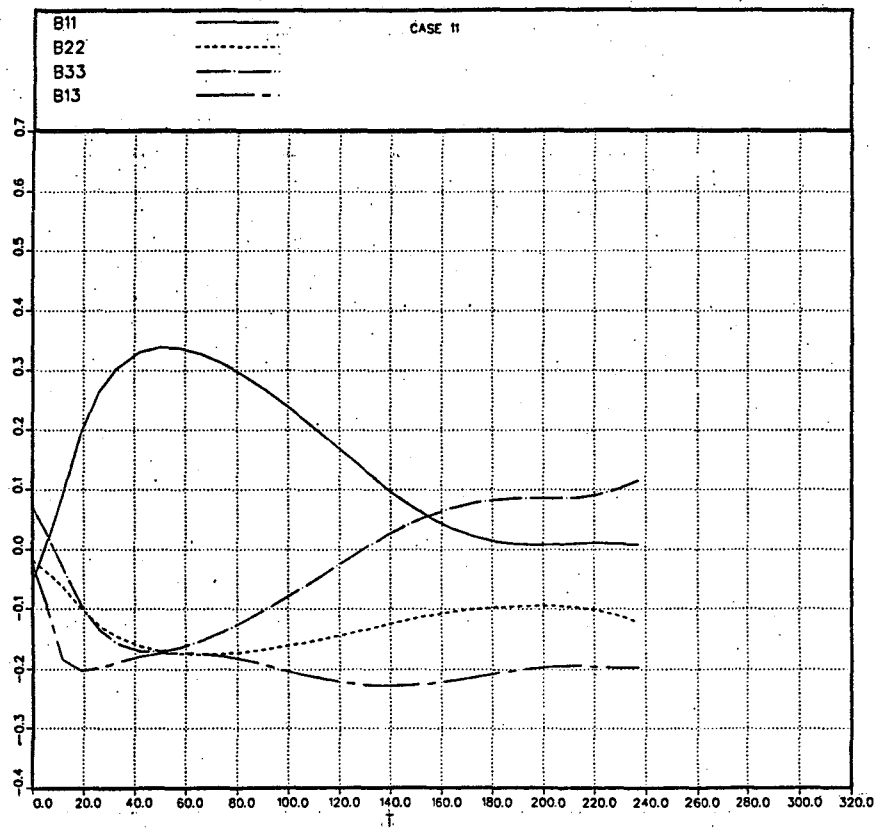


Fig. 5.8.7. Time history of the anisotropy tensor B_{ij} for Case 11.

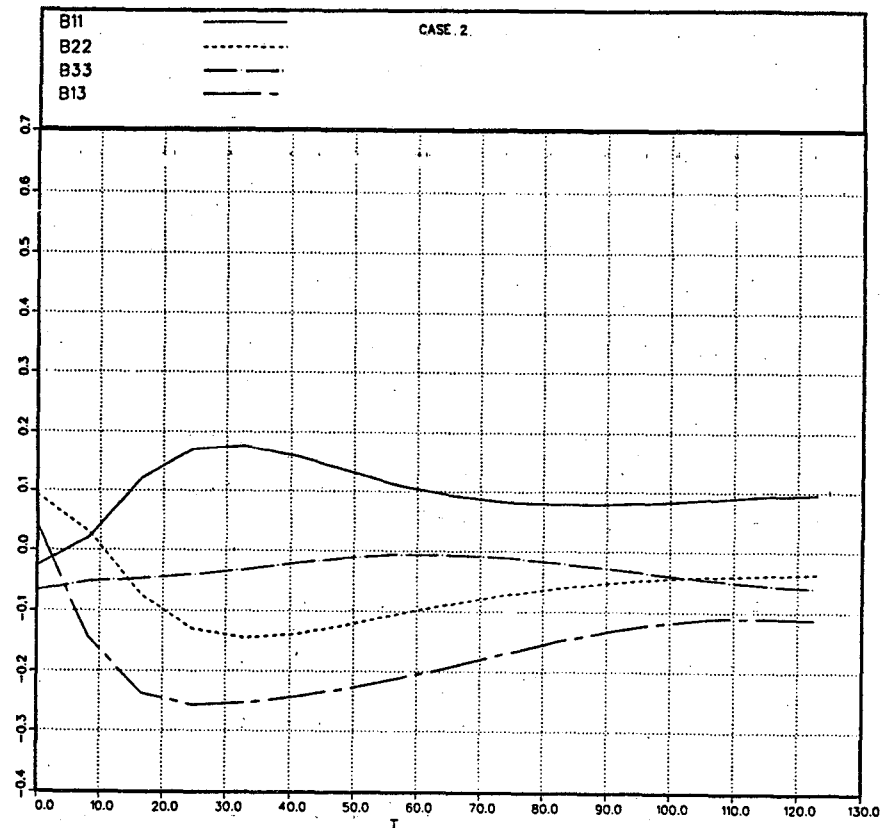


Fig. 5.8.8. Time history of the anisotropy tensor B_{ij} for Case 2.

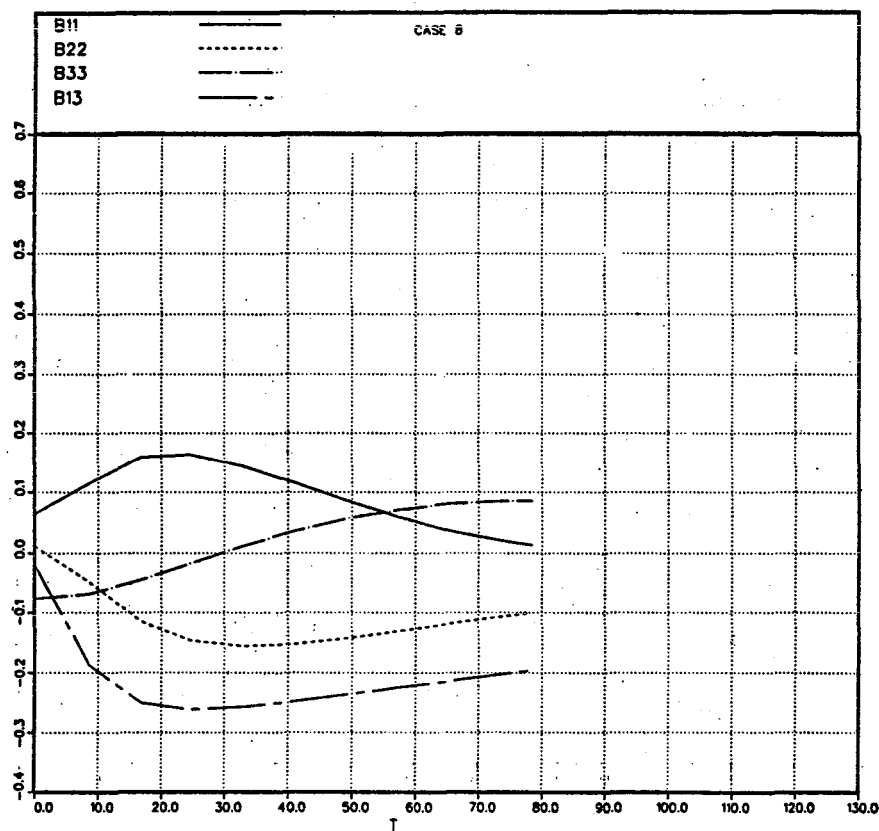


Fig. 5.8.9. Time history of the anisotropy tensor B_{ij} for Case 8.

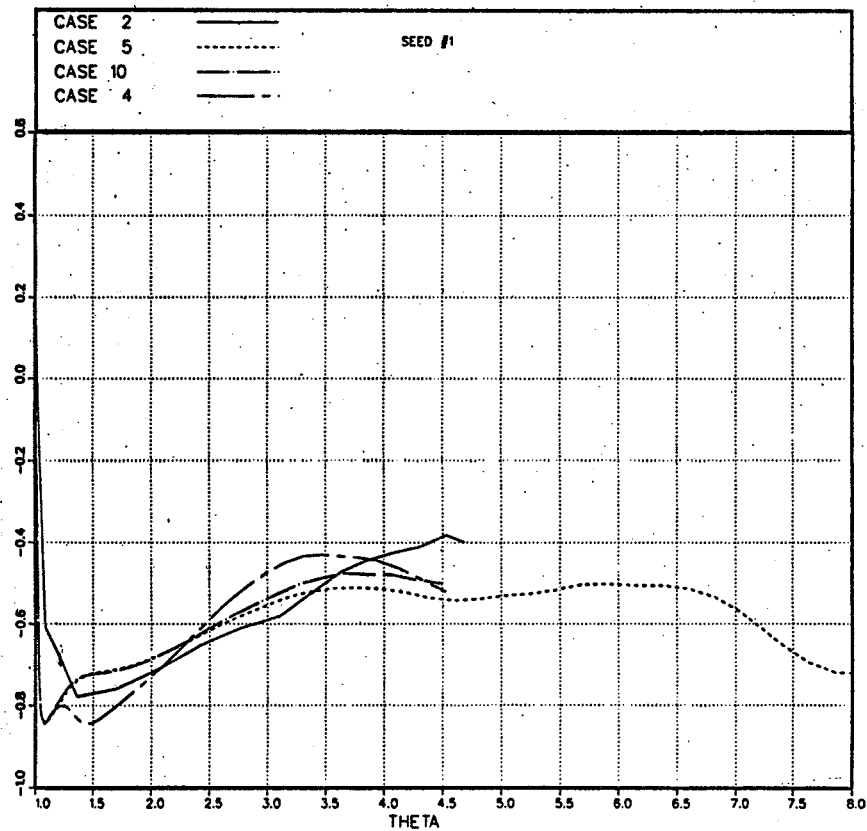


Fig. 5.9.1. Correlation coefficient at the center of the layer vs. normalized momentum thickness for cases with seed #1.

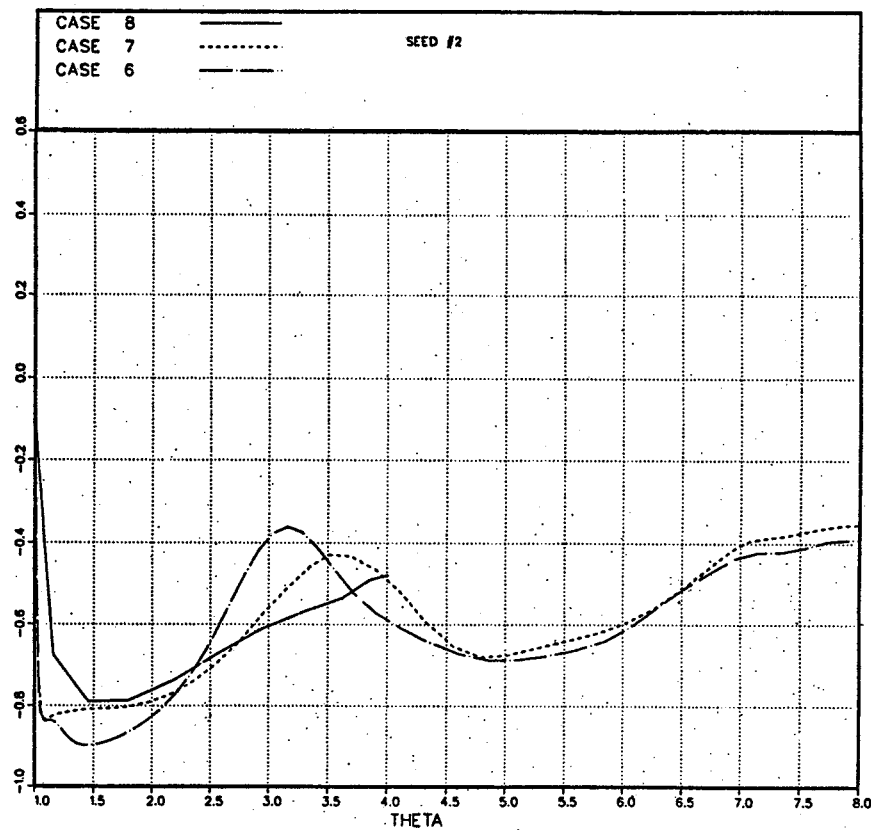


Fig. 5.9.2. Correlation coefficient at the center of the layer vs. normalized momentum thickness for seed #2.

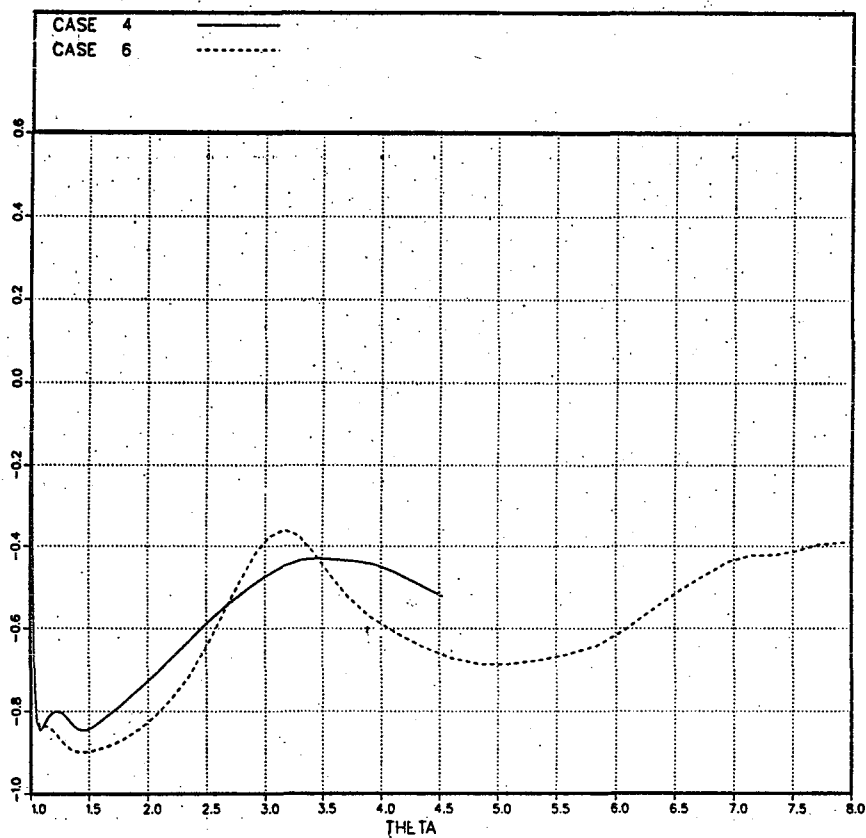


Fig. 5.9.3. Correlation coefficient at the center of the layer vs. normalized momentum thickness for low-amplitude Cases 4 and 6.

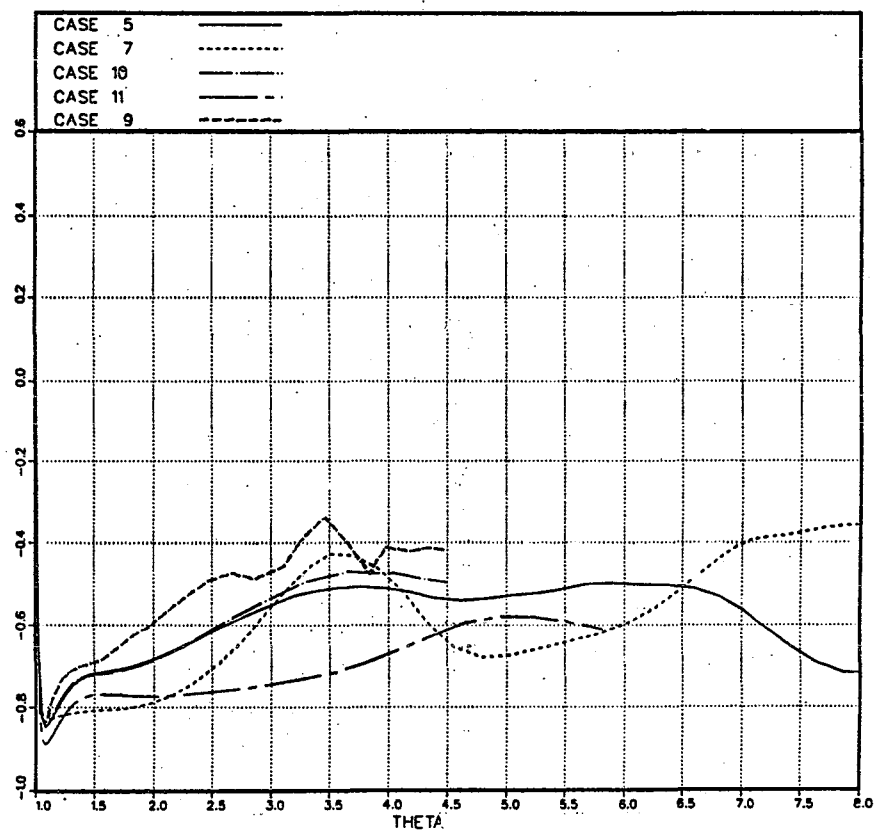


Fig. 5.9.4. Correlation coefficient at the center of the layer vs. normalized momentum thickness for medium-amplitude Cases 5, 7, 9, 10, and 11.

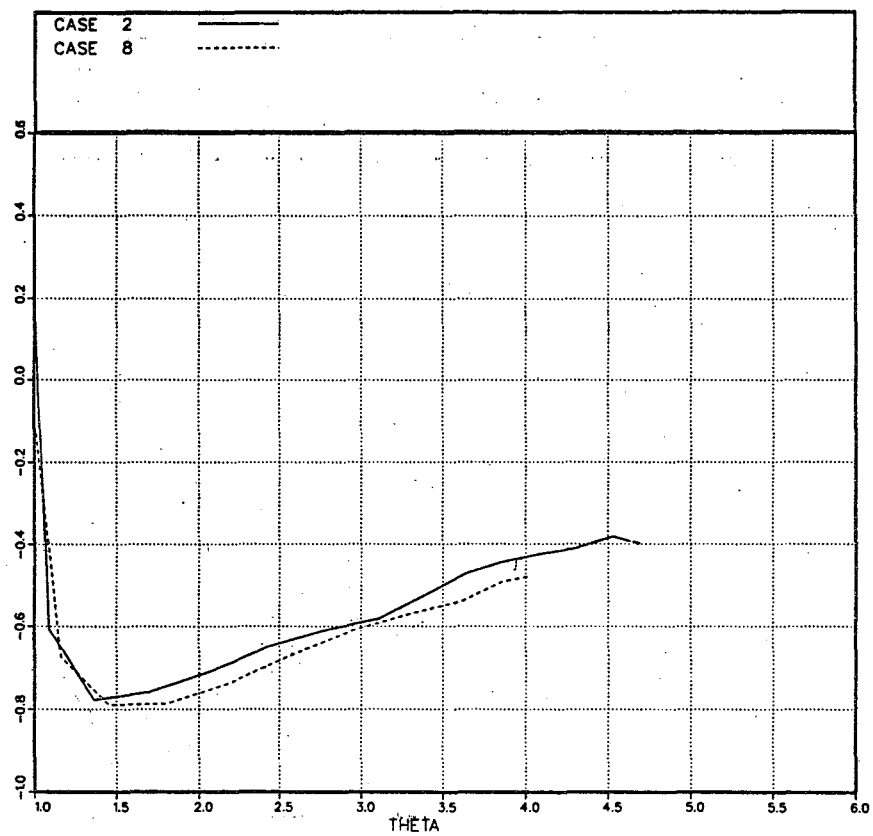


Fig. 5.9.5. Correlation coefficient at the center of the layer vs. normalized momentum thickness for high-amplitude Cases 2 and 8.

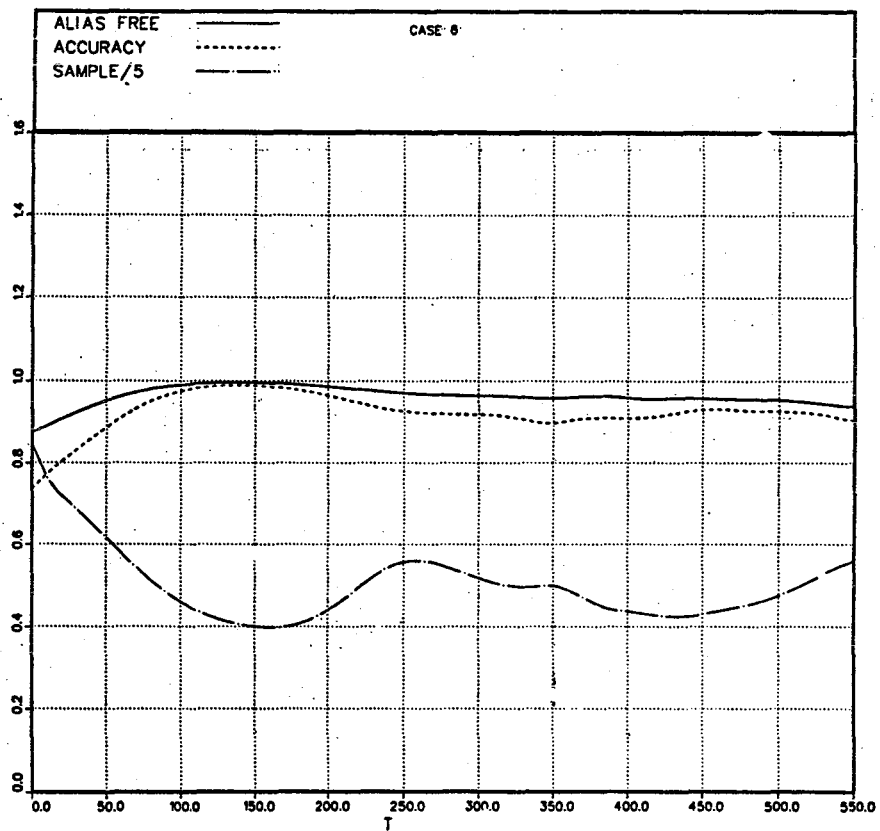


Fig. 5.10.1. Time history of alias-free accuracy and sample size parameters η_{AF} , η_A , and η_S .

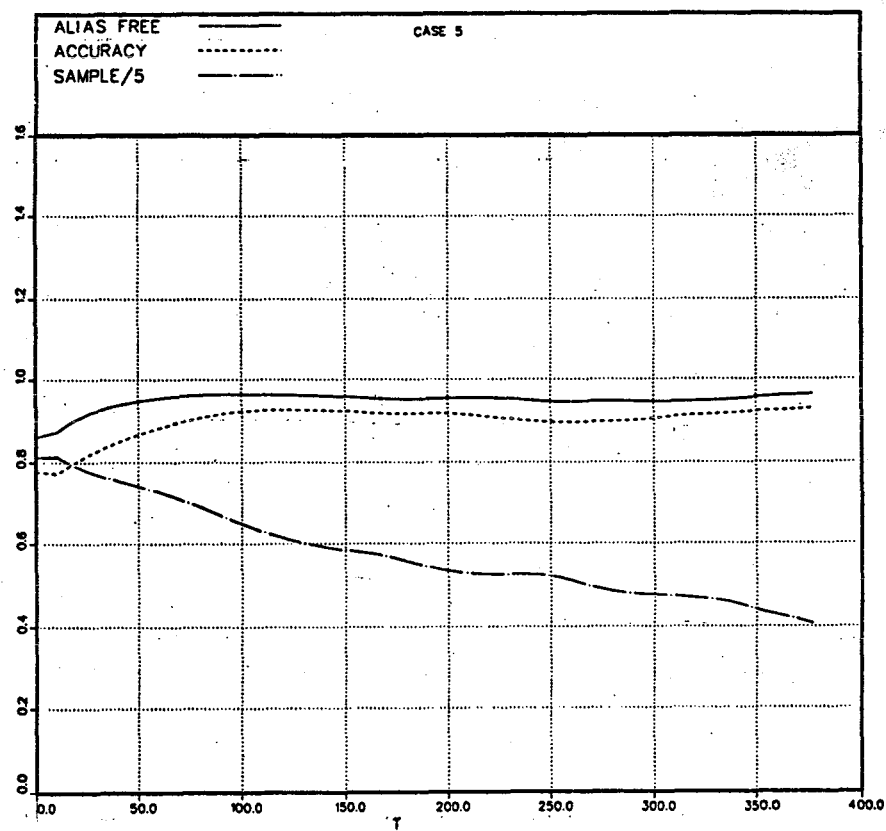


Fig. 5.10.2. Time history of alias-free accuracy and sample size parameters η_{AF} , η_A , and η_S .

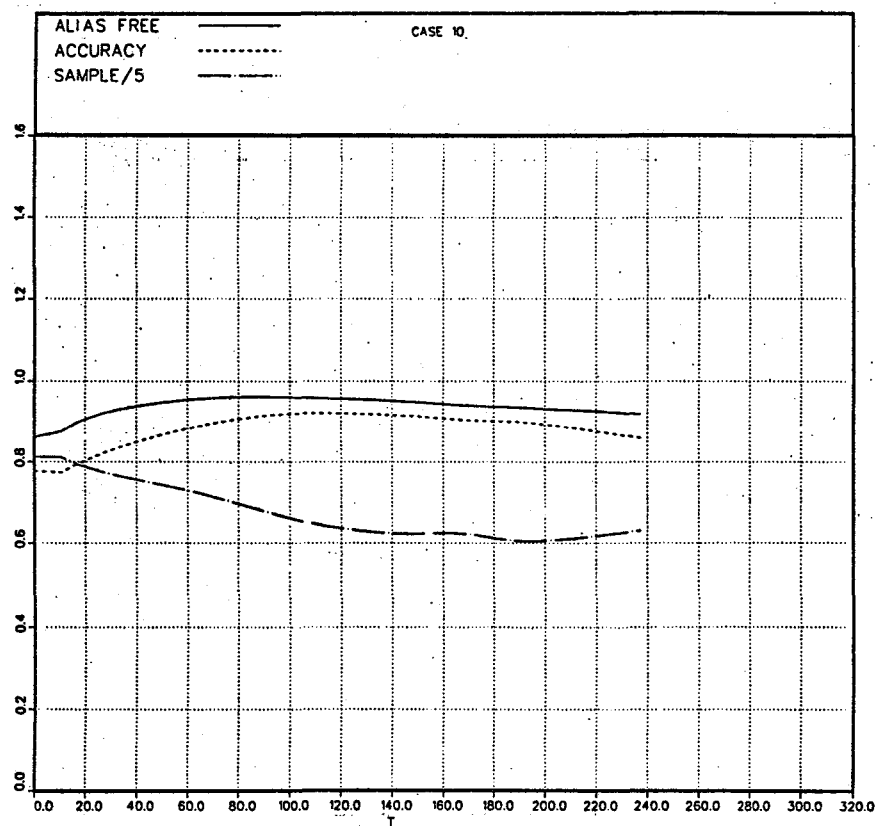


Fig. 5.10.3. Time history of alias-free accuracy and sample size parameters η_{AF} , η_A , and η_S .

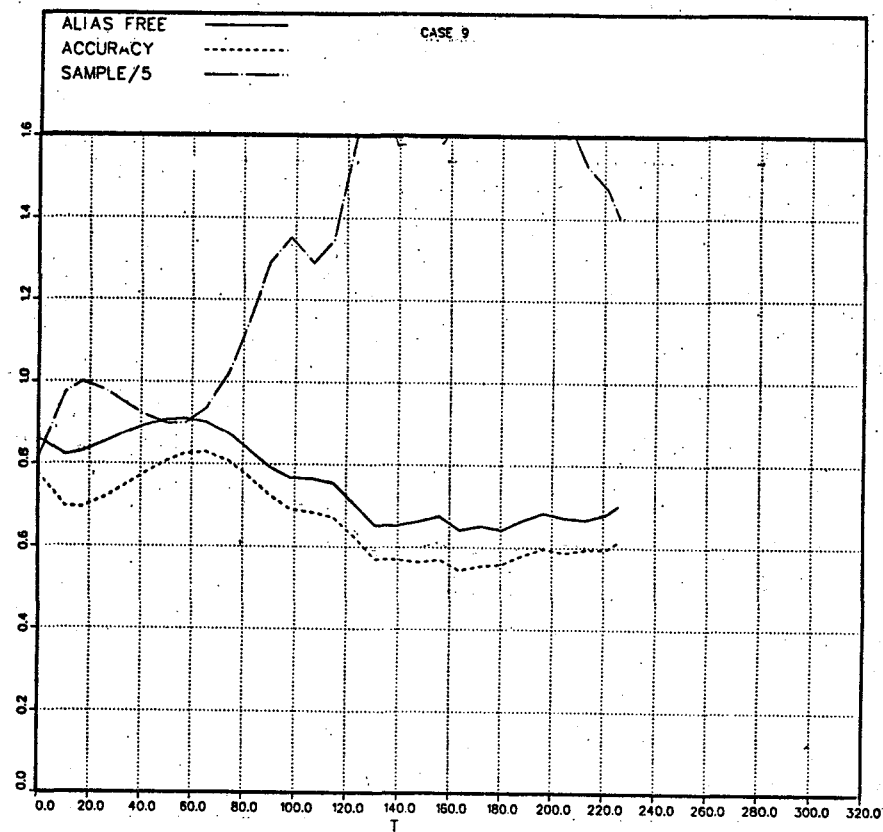


Fig. 5.10.4. Time history of alias-free accuracy and sample size parameters η_{AF} , η_A , and η_S .

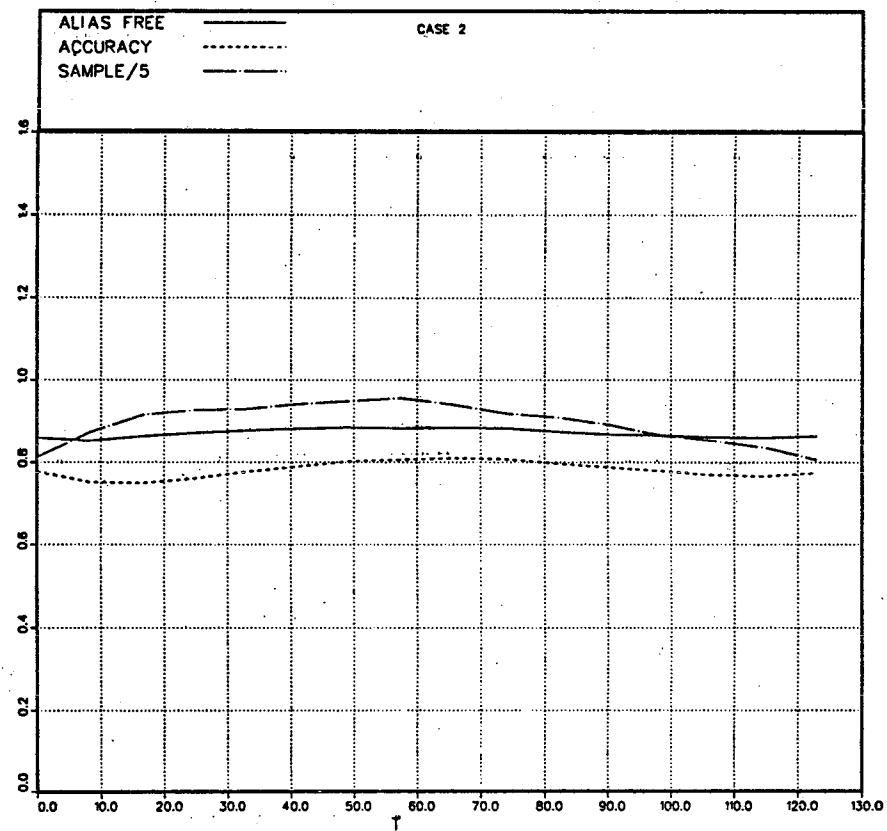


Fig. 5.10.5. Time history of alias-free accuracy and sample size parameters η_{AF} , η_A , and η_S .

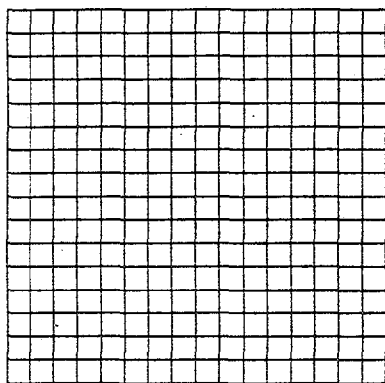


Fig. 5.11.1. Plan view of particle tracking grid for all cases at $T = 0$.

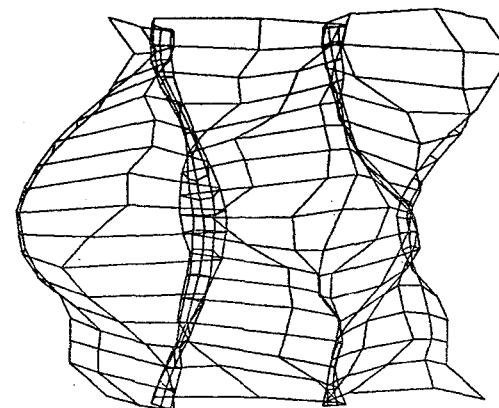


Fig. 5.11.2. Plan view of particle tracking grid for Case 6 at $T = 161$.

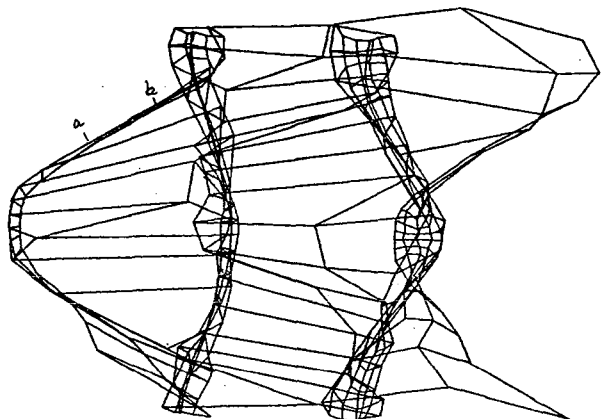


Fig. 5.11.3. Plan view of particle tracking grid for Case 6 at $T = 200$.

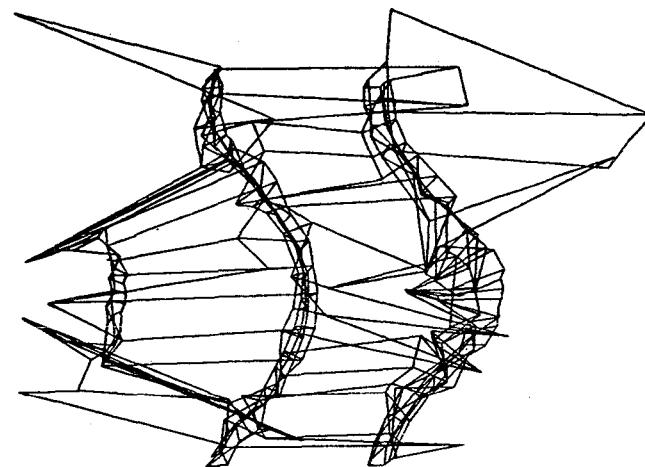


Fig. 5.11.4. Plan view of particle tracking grid for Case 6 at $T = 280$.

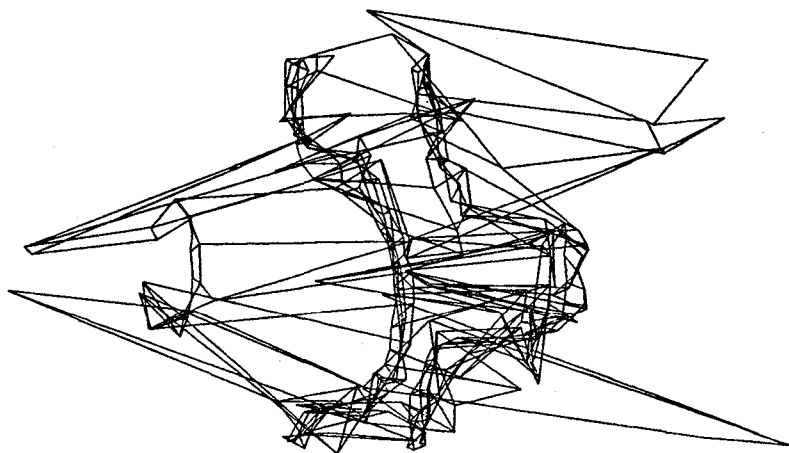
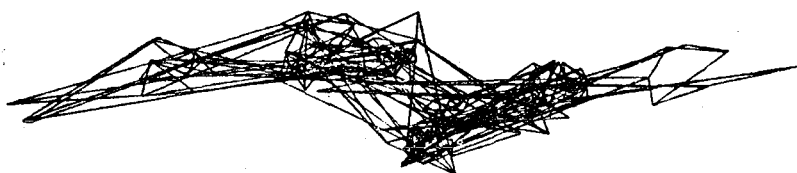


Fig. 5.11.5. Plan view of particle tracking grid for Case 6 at $T = 342$.



Fig. 5.11.6. Span view of particle tracking grid for Case 6 at $T = 200$.



116

Fig. 5.11.7. Span view of particle tracking grid for Case 6 at $T = 342$.

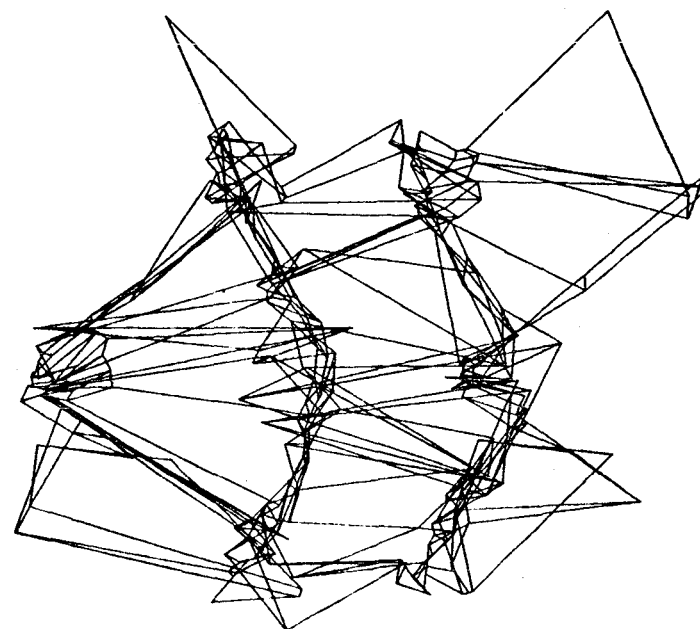


Fig. 5.11.8. Plan view of particle tracking grid for Case 7 at $T = 177$.

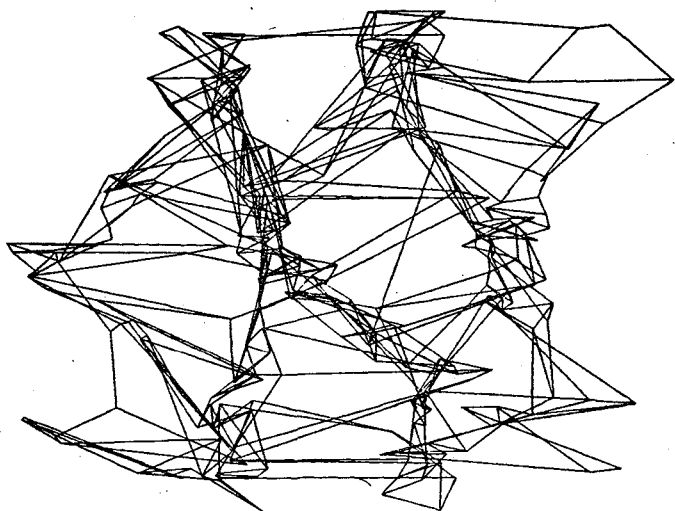


Fig. 5.11.9. Plan view of particle tracking grid for Case 8 at $T = 76$.

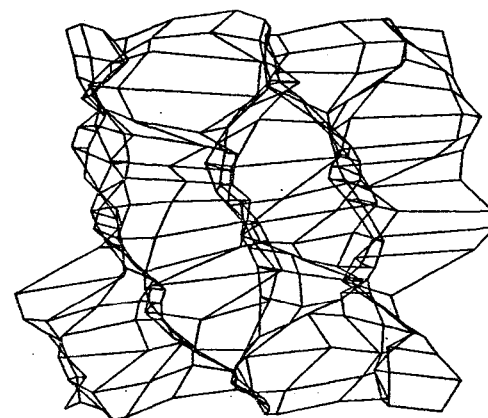


Fig. 5.11.10. Plan view of particle tracking grid for Case 10 at $T = 76$.

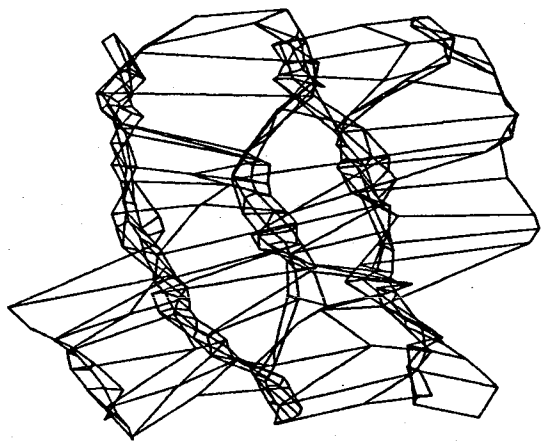


Fig. 5.11.11. Plan view of particle tracking grid for Case 10 at $T = 97$.

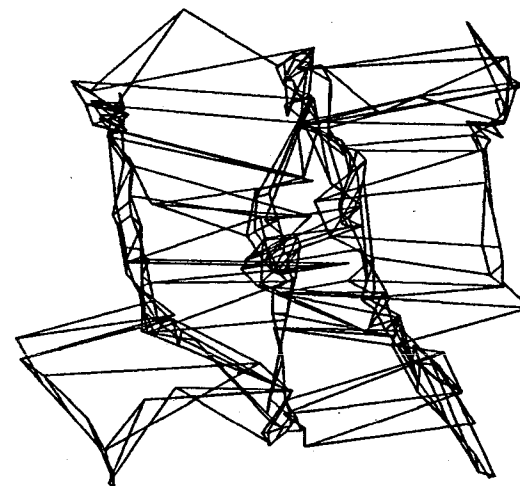


Fig. 5.11.12. Plan view of particle tracking grid for Case 10 at $T = 151$.

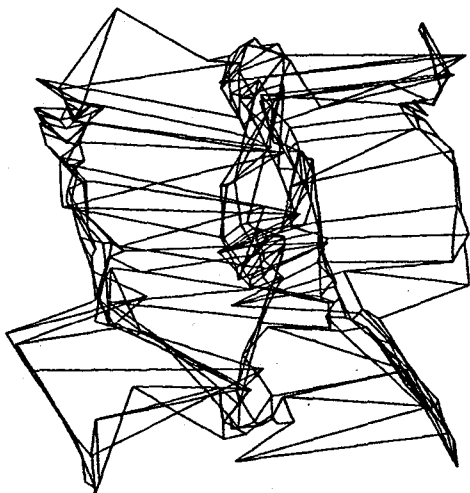


Fig. 5.11.13. Plan view of particle tracking grid for Case 10 at $T = 171$.

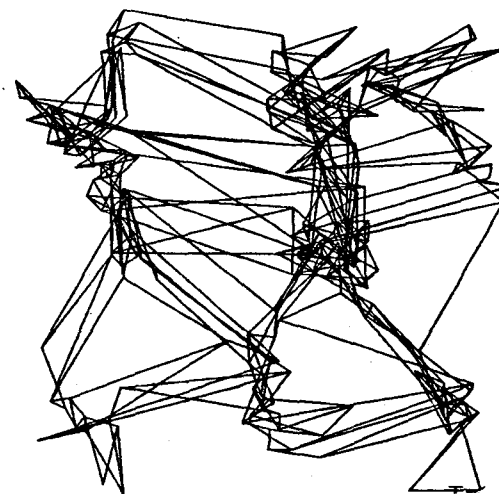


Fig. 5.11.14. Plan view of particle tracking grid for Case 10 at $T = 231$.

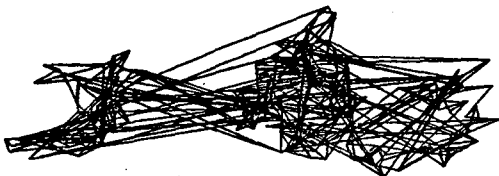


Fig. 5.11.15. Span view of particle tracking grid for Case 10 at $T = 231$.

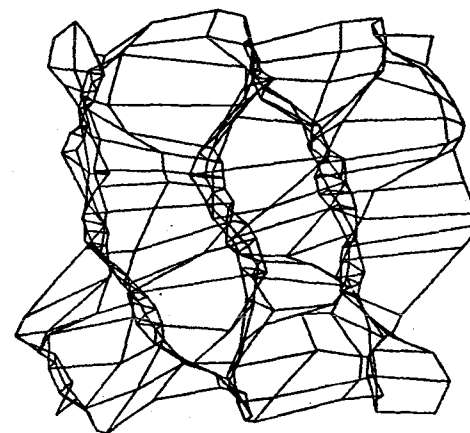


Fig. 5.11.16. Plan view of particle tracking grid for Case 9 at $T = 76$.

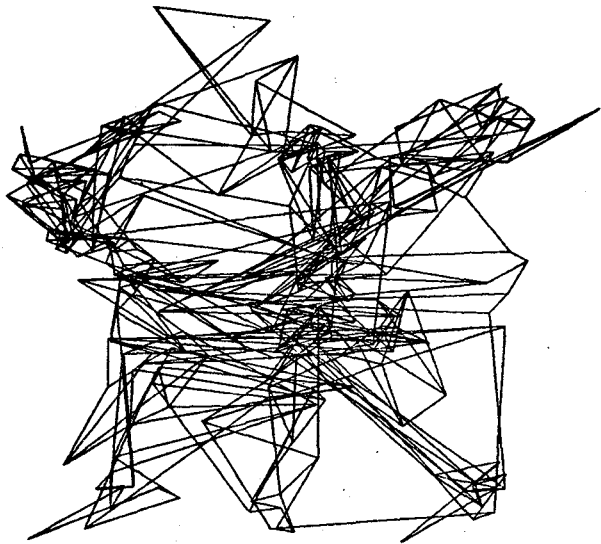


Fig. 5.11.17. Plan view of particle tracking grid for Case 9 at $T = 220$.

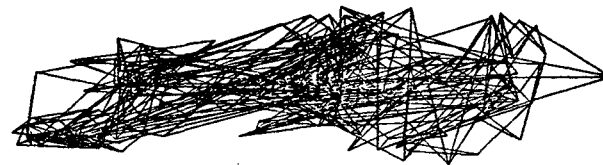


Fig. 5.11.18. Span view of particle tracking grid for Case 9 at $T = 220$.

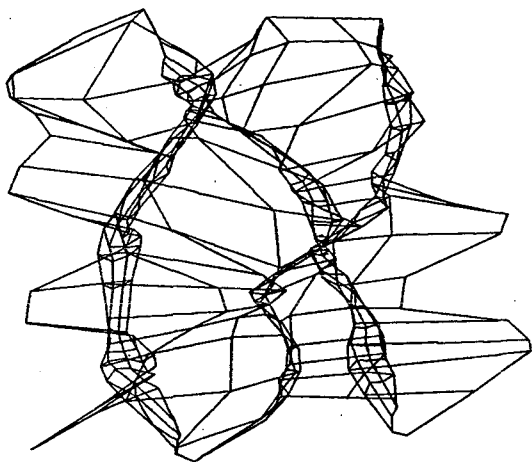


Fig. 5.11.19. Plan view of particle tracking grid for Case 11 at $T = 97$.

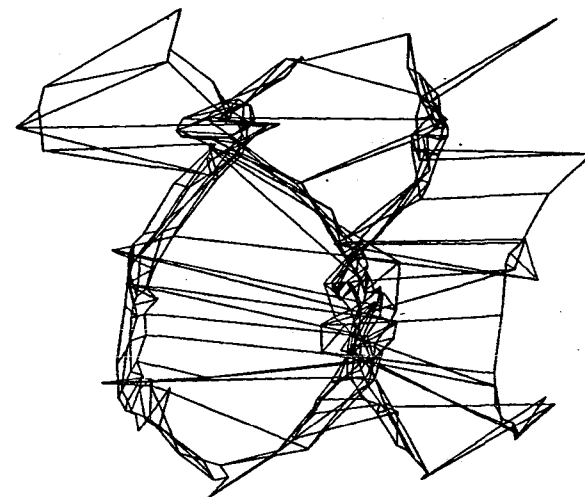


Fig. 5.11.20. Plan view of particle tracking grid for Case 11 at $T = 151$.

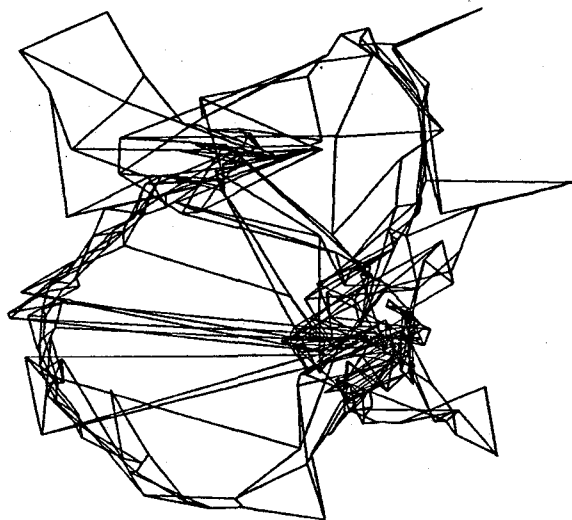


Fig. 5.11.21. Plan view of particle tracking grid for Case 11 at $T = 231$.



Fig. 5.11.22 Span view of particle tracking grid for Case 11 at $T = 171$.

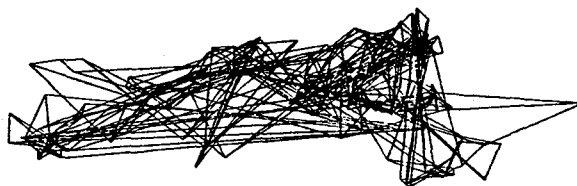
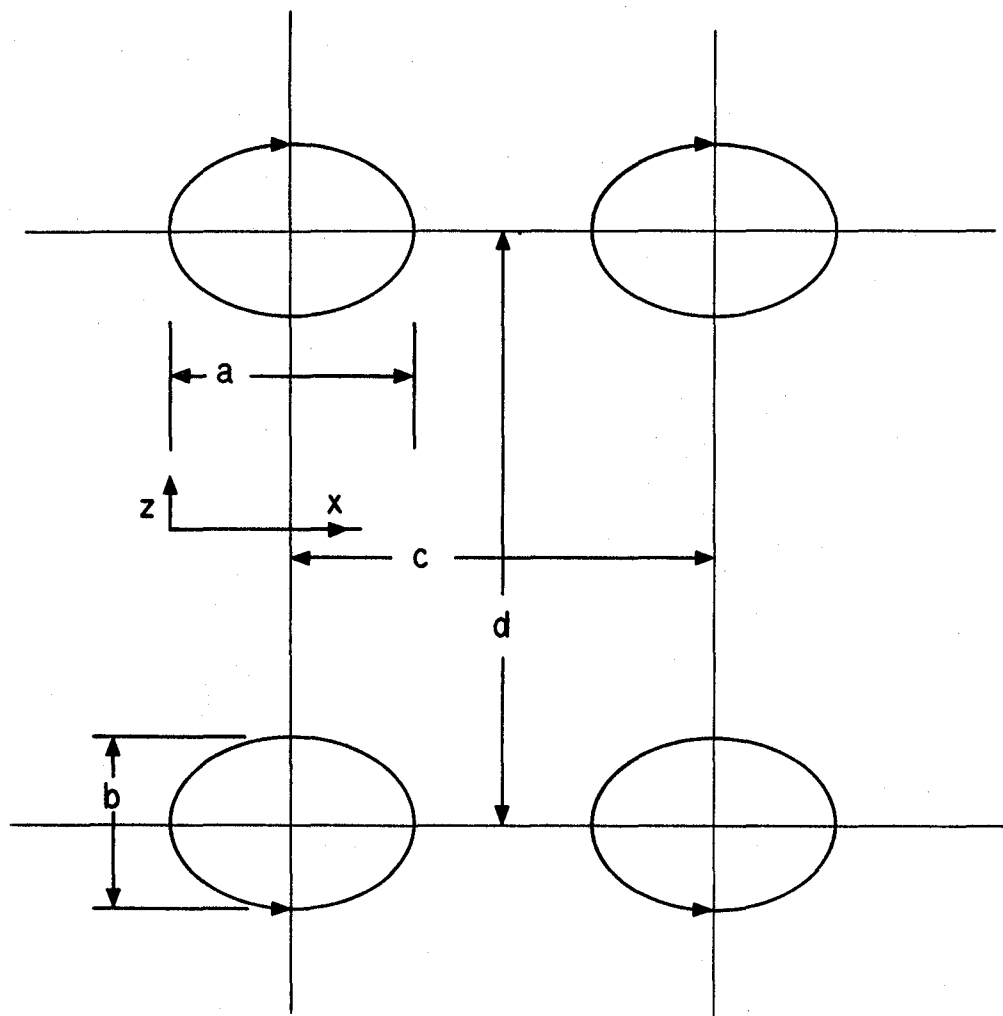


Fig. 5.11.23. Span view of particle tracking grid for
Case 11 at $T = 231$.



$$\frac{b}{a} = 3/4 ; \frac{d}{c} = 3/2$$

Fig. D.1 Schematic view of vortex pairing, image flow study.

End of Document